The Dissertation Committee for Sigfried William Haering
certifies that this is the approved version of the following dissertation:

Anisotropic hybrid turbulence modeling with specific application to the simulation of pulse-actuated dynamic stall control

Committee:

Robert D. Moser, Supervisor

Jayathi Murthy

David G. Bogard

Ofodike A. Ezekoye

Todd Oliver

Anisotropic hybrid turbulence modeling with specific application to the simulation of pulse-actuated dynamic stall control

by

Sigfried William Haering, B.S.M.E, M.S.E.

DISSERTATION

Presented to the Faculty of the Graduate School of

The University of Texas at Austin

in Partial Fulfillment

of the Requirements

for the Degree of

DOCTOR OF PHILOSOPHY

THE UNIVERSITY OF TEXAS AT AUSTIN

December 2015

Anisotropic hybrid turbulence modeling with specific application to the simulation of pulse-actuated dynamic stall control

Publication No. ____________________

Sigfried William Haering, Ph.D.
The University of Texas at Austin, 2015

Supervisor: Robert D. Moser

Experimental studies have shown pulse actuated dynamic stall control may provide a simple means to significantly increase the performance of lifting surfaces and expand their flight envelope. However, precise information of the complex boundary layer reattachment mechanisms are inaccessible to experimental measurements. Therefore, simulations are necessary to fully understand, optimize, and apply this method. Due to the inherent shortcomings of RANS, computational expense of LES, and deficiencies in current hybrid modeling approaches, a new hybrid modeling framework has been developed. Based in using the two-point second-order structure function to drive a local equilibrium between resolved and modeled turbulence, the new approach addresses issues associated with inhomogeneous and anisotropic grids as well as the treatment of the RANS/LES interface in hybrid simulations. Numerical studies using hybrid RANS/LES modeling approaches of a stalled airfoil with spanwise-uniform actuation regions experiencing single pulse actuated flow reattachment have been performed. The mechanism responsible for reattachment has been identified as a repeating wall-vortex interaction process. The new hybrid framework and anisotropic SGS models developed here are anticipated to be of great benefit well beyond the focus of this work with application to many challenging flow situations of pressing engineering interest.

Table of Contents

List of Tables

List of Figures

Chapter 1

Introduction

We shall not cease from exploration
And the end of all our exploring
Will be to arrive where we started
And know the place for the first time.
-T.S. Eliot

The promise of simulation-based engineering design and scientific discovery is to provide unparalleled insight into physical phenomena thereby opening new frontiers in design while simultaneously drastically reducing the time and expense of implementing new technologies. These lofty expectations have always been hampered by limited computational resources. More recently however, progress in the simulations of fluid systems has been slowed by an over-reliance on and broad application of Reynolds-averaged Navier-Stokes (RANS) turbulence models which are widely recognized to be unable to provide predictive simulation capability for many flows of technological interest. The recognition of limitations in accuracy of turbulence models has spurred a shift toward partial direct simulation, *i.e.* large eddy simulation (LES). While in principal LES removes the burden of accurately modeling all of the effects of complex turbulent flows, they fail in removing the burden of computational cost associated with complex geometries like aircraft, spacecraft, and turbomachines due to resolution requirements in boundary layers. For the foreseeable future, predictive simulation of high Reynolds number flows of engineering interest requires a flexible balance between modeling all turbulence effects and simulating all turbulence, guided by realistic expectations of the capabilities and limitations of existing turbulence model.

The body of work presented here pursues the development and demonstration of a new and comprehensive hybrid modeling framework with impetus provided by the simulation of pulse-actuated dynamic stall control of airfoils. This particularly complicated flow scenario involves the interaction of coherent turbulent structures with attached boundary layers, recirculating separation regions, and detached shear layers resulting in dynamic smooth-wall separation and reattachment. This single problem incapsulates nearly all of the simulation challenges outlined in the NASA CFD Vision 2030 Study [12] as being the significant hurdles in advancing the state of simulation-based engineering in aerospace. The resulting hybrid RANS/LES modeling approach is anticipated to be robust and predictive with general applicability to flows of interest to the aeronautics community well beyond the specific case examined here.

1.1 The Simulation of Pulse-Actuated Stall Control

Experiments have demonstrated that the separated flow on a stalled airfoil is highly susceptible to actuation using a brief ($\mathcal{O}0.1t_{conv}$) impulse applied near the origin of the separation [3, 13]. A collapse of the recirculation region accompanied by a large transitory increase in lift and reduction of drag on a significantly longer time scale ($\mathcal{O}10t_{conv}$) follows application of these pulses [2, 10, 14]. Referred to as "pulse actuated dynamic stall control", this method may provide a simple means to significantly increase the performance of lifting surfaces and expand their flight envelope. However, detailed information of the complex boundary layer reattachment mechanisms remain inaccessible to experiments due to relatively coarse measurement techniques. Adequately resolved simulations provide intricate flow details necessary to fully understand and implement this approach. Additionally, nearly any geometry and configuration may be simulated while similar modifications to experimental conditions are difficult and expensive yet are critical to design optimization.

Simulation of pulse actuation and the subsequent reattachment process presents a significant modeling challenge. At Reynolds numbers of interest ($\mathcal{O}10^6$) and necessary convective times ($\mathcal{O}10t_{conv}$), direct numerical simulations are not feasible. Reynolds averaged Navier Stokes (RANS) simulations are by design unable to directly simulate the complex transitory flow features responsible for reattachment while also not accurately modeling the effects of such highly geometry-specific turbulent structures. Large eddy simulations (LES) are ideally suited for resolving large anisotropic features of interest to this study. However, near-wall turbulent boundary layer simulations remain computationally expensive due to the scale of the "large" eddies being smaller than the boundary layer thickness. Presently, the only viable modeling option is a hybrid RANS-LES approach.

Driven by the need to optimize simulation capabilities against available computational resources, hybrid modeling approaches have become the leading candidate for the simulation of complex flow scenarios. Significant savings are achievable by direct simulation of only unsteady and turbulent flow features of particular interesest to an investigation while modeling the remaining regions and scales. However, the delicate interaction between resolved and modeled turbulence has been broadly neglected or greatly simplified. Additionally, the degree of physically meaningful turbulence which can be dynamically supported by the available resolution has been typically reduced to a comparison between a scalar measure of the local grid and the modeled quantities with no consideration for the state of the resolved field. Worse still, the degree of simulated turbulence is sometimes declared beforehand effectively "hardcoding" the simulation without any regard for what it is actually doing.

The simulation of pulse-actuated stall control is in many ways the "perfect storm" for hybrid techniques. While the separation point of massively separated flows is largely predetermined by the geometry (*e.g.* the leading edge of airfoils), for stalled airfoils at moderate angles of attack, flow will separate along its smooth surface. Further complicating the matter is that for dynamic stall, the separation point location will fluctuate with the shedding of trailing edge vortices. The location of such a separation point is not strongly defined by the airfoil geometry and is very sensitive to modeling errors and resolution while being critical to accurately simulating separated flows [15]. The specific case of interest to this study is particularly susceptible to hybrid model transition issues due to the physical actuator being located near the origin of the separation layer. The small scale of the actuator ($\mathcal{O}10^{-4}c$) requires high resolution complicating transition and separation behavior which are already problematic to a hybrid methods. Additionally, at least partial direct simulation of pulse-induced turbulent flow structures is required to capture the reattachment process. These structures are generated at and move along the airfoil surface while interacting with the attached boundary layer and recirculation region *i.e.*, precisely where hybrid models will attempt to model all turbulence. For hybrid simulations to progress to a level of robustness and accuracy required by the problem at hand, these issues must be addressed.

1.2 Overview of Research

Preliminary studies of pulse-actuated stall control have been performed with detached eddy simulation (DES) yielding poor results. However, the deficiencies and critical issues identified from these simulations have lead to the development of a new hybrid modeling method comprised of three main components. First, a structure function based subgrid stress model which accounts for anisotropy in both the resolution and resolved turbulence is proposed. This model is used to guide the development of a complete hybrid RANS/LES modeling framework. In general, modeled turbulence is returned to resolved scales by reduced or negative model viscosity until a balance between theoretical and actual modeled turbulence is attained provided the available resolution. Additionally, a general viscosity-based correction is proposed for grid/resolution inhomogeneities. Both the hybrid framework and resolution gradient corrections are energy conserving through an exchange of resolved and modeled turbulence. The new modeling and hybrid framework approach presented here is anticipated to solve problems associated with dynamic smooth body separation and complex geometries manifesting in anisotropic and inhomogeneous grids.

Numerical studies using the new hybrid modeling approach on a stalled airfoil with a spanwise uniform actuation region experiencing single pulse actuated flow reattachment are performed. The simulations are in general agreement with experimental measurements and provide detailed information of the reattachment process which may be used to guide further development of the proposed technology. In particular, these simulations may be used to determine optimal impulse strength, actuator spacing, orientation, geometry, and pulse scheduling. Maturation of pulsed jet actuation technology may lead to significantly enhanced aerospace platform performance by improving maneuverability, increasing payload, increasing range, and lowering overall cost.

This dissertation is organized as follows. Background for this work is separated into three chapter. First, (§2.1) general flow control methodology is reviewed followed by (§2.2) a summary of the wind tunnel pulse actuation experiments of Glezer and colleagues at GaTech in Chapter 2. Second, (§3.1-§3.3) relevant turbulence modeling approaches are reviewed with emphasis given to the (§3.4) general methods used in hybrid modeling in Chapter 3. In particular, Detached Eddy Simulation (DES) is discussed as an exemplar for typical deficiencies exhibited by existing hybrid methods. And third, Chapter 4 reviews relevant existing simulations in the literature (§4.1) and discusses previous attempts of simulating pulse actuated stall control using SA-based DDES (§4.2) are recounted to illustrate the necessary improvements for the simulation of pulse-actuated dynamic stall control. Chapter 5 describes modeling innovations and developments related to subgrid stress anisotropy (§5.2), hybridization (§5.3), and grid inhomogeneities (§5.4). Demonstration and validation are presented in Chapter 6. Finally, the complete new hybrid modeling framework is applied to the problem of pulse actuated stall control with assessment of agreement with available experimental measurements and discussion of revealed insights into the mechanisms driving the process in Chapter 7.

Chapter 2

Experimental Background

This chapter provides a brief description of general flow control methods and applications with focus on pulsed jets. The impetus for developing a new hybrid framework discussed in Chapter 5 was provided by the desire to further understand pulse-actuated stall control mechanisms through information attainable via simulations. The simulations performed in Chapter 7 follow from wind tunnel experiments at the Georgia Institute of Technology. Details of their pulsed actuation experimental setup and results are presented and discussed.

2.1 Flow control

The central idea of flow control is that small local perturbations may induce large global changes in the flow. Since Prandtl first hypothesized in 1905 that separated flows are extremely sensitive to boundary layer conditions [16], flow control has been an active subject of fluid physics research and engineering application. In addition to separation and stall control, a rich variety of applications has emerged including maneuvering, thermal management, vibration reduction and noise control, and drag reduction [17–22]. In general, the flow around some object is manipulated with a perturbation, be it passive (some fixed structure such as fins and winglets) or active (suction, blowing, pulsed jets, *etc.*). Such manipulations typically manifest in the displacement of streamlines, virtual modification of the surface shape, entrainment of fluid via vortex formation and advection, and/or enhanced turbulent mixing.

Two prominent types of active flow control are synthetic and impulsive jet-based methods. A comprehensive review of synthetic jets and their issues are presented by Glezer [23, 24]. Defined by zero net mass flux into the flow system, synthetic jets are formed entirely by entraining the surrounding fluid. Typically, some sort of oscillating surface (piston, vibrating diaphragm, *etc.*) is used to generate periods of suction and ejection through an orifice. Thus, momentum is imparted into the system via a boundary interface and not accompanied by additional mass. Similar effects can be produced be directly inducing local pressure gradients using purely acoustic means [25, 26]. Often the orifice design is exploited to generate unstable shear interfaces with the exiting fluid to generate vortices which are responsible for fluid entrainment. However, it is often seen that only one period of the blowing/suction cycle produces the desired flow control effects. Additionally, the duty cycle of these synthesized jets is directly related to the strength of the perturbation. That is, the amount of momentum that can be introduced into the flow is coupled with the frequency of the displacement and speed of the oscillating surface.

Impulse jets have been developed more recently and have seen primary application to separation control [10, 14, 27]. Contrary to their synthetic counterpart, impulse jets introduce momentum into the flow by means of mass injection. By using an external source of fluid to introduce momentum into the surrounding flow, they are free to operate at nearly any combination of impulse strength and frequency (or even discontinuous anharmonic applications). Thus, mass-flux based jets may be used to generate strong vortices and potentially be used in high-speed situations. The downside, of course, is that one must design the delivery system for this additional fluid which tends to be more complicated and possibly more bulky and massive than synthetic jets. The simulations performed here are concerned with this type of flow control and is intended to investigate and optimize the effects of actuation on the flow, not the systems needed to deliver flow to the actuator.

Jets with blowing periods on the order of the convective time or the vortex shedding period ($St_{jet} \approx 1$) have been used to achieve moderate levels of unsteady reattachment. Such methods act on the timescales of global flow instabilities and result in Coanda-like deflection of high momentum fluid towards the jet and solid surface thereby increasing lift. Sustained lift enhancements of 35% have been observed with post-stall angle NACA 0015 airfoils [28]. More recently, jets with a characteristic frequency of an order of magnitude greater than global instabilities have been used to achieve more significant levels of flow control. The higher frequency and shorter duration results in a decoupling from global flow instabilities while strongly interacting with local flow instabilities such as the separation shear layer [24, 29]. Additionally, domains of trapped vorticity have been used to alter the effective shape of the structure [30, 31] where a reduction in pressure drag of over 50% was observed.

2.2 GaTech Experiments

The simulations performed here follow directly from experiments performed at the Georgia Institute of Technology under the guidance of Professor Ari Glezer. The Fluid Mechanics Research Laboratory has been a leader in the area of active flow control for 20 years, with studies ranging from aerodynamic flow-control, multi phase heat transfer processes, thermal management, small-scale mixing in reacting flows, biological flows, fluidic-controlled bioreactors, and most recently energy conversion. Their experiments in active flow control have used electromechanical, synthetic jet, fluidic oscillator, aero-bleed, and combustion actuators [32].

Relevant pulsed jet experiments were performed by Woo *et.al.* [2,13,14] and Brzozowski *et.al.* [3,10]. Both use a NACA 4415 (457mm chord length) in an approximately 2.19c square cross-sectional wind tunnel at Reynolds number of 0.57x10^6 (U_∞=20m/s, t_{conv}=22.85ms) and Mach number of 0.058. Moveable walls are affixed to the airfoil to constrain the flow to be approximately two dimensional, as spanwise coherent vortices can form with termination at these walls. A series of pitch and plunge motors allow for large vertical translation and angle of attack variation. The airfoil is instrumented with 75 static pressure ports along the midspan. Rise times and sample rates for the pressure gages are not provided. Full-field velocity measurements are phase-lock averaged over a 0.5c square field of view with a 5x10^{-4}c/pixel (224μm/pixel) resolution PIV system. Flow is seeded with 2x10^{-6}c particles and illuminated 100 times per t_{conv} (500 fps) with an Nd-Yag laser. Each field is phase-averaged over 200-250 images and therefore reveal ensemble average flow fields.

Located at 0.15c, an actuator array of width 4.2x10^{-2}c by 6.6x10^{-4}c with 7.0x$10^{-3}c$ spacing in-between individual actuator orifices can be selectively fired to study finite and nearly uniform actuation zones. The pulsed jet array is composed of seven simple spark-initiated combustion chambers coined the COMPACT system (COMbustion Powered ACTuators) [33, 34]. Each chamber is 1x$10^{-5}c^3$ ($1cm^3$) with operating frequencies of up to 500 Hz. Exact measurements of the hot COMPACT exhaust gas is difficult due the size and duration of the pulses. The total duration of the pulses is approximately $0.118t_{conv}$ (2.7ms) with a rapid rise occurring over 25% of the total pulse duration with a gradual decent over the remaining 75% of the total active actuation time. Fuel is premixed hydrogen and air and achieves peak conditions of 2400K, 2.8atm, and velocities of $17.16U_\infty$ (mach one owing to choked flow) at $0.0306t_{conv}$ (0.7ms) after spark initiation. An approximate peak thrust of 0.35N and a net impulse of 0.45mN-s per pulse has been demonstrated corresponding to a momentum flux of 6KPa. Exhaust gas expands with a cone of slope 0.25 as measured from phase-locked Schlieren imagery. Experimental findings are summarized next.

Various available data from GaTech experiments are summarized in Table 2.1 . Baseline stalled circulation is calculated to be $5.3m/s^2$ [13]. No variances or uncertainty in these data are currently available. The variability observed for ostensibly the same or very similar experimental conditions is worth noting. For instance, while the decrease in lift from a degree of additional angle of attack is certainly expected, the decrease in drag is not. Additionally, studies conducted at $\alpha = 19°$ during the same year (2010) [10, 14] have largely different lift coefficients and stall angles. For comparison, $C_L \approx 1.4$ at 20° and $Re = 0.5\text{x}10^6$ as predicted by xfoil[1] code [35]. Thus, a more qualitative comparison to simulations is merited provided the large degree of experimental variability.

Separation	Stall Angle	C_L	C_D	α	Source
0.15c	17°	1.16	0.16	20°	[13]
0.2c	17°	1.16	0.16	20°	[2]
0.3c	16°	1.33	0.21	19°	[10]
not provided	14°	1.7, 1.5*	not provided	19°	[14]

Table 2.1: List of nominal baseline experimental results and corresponding publications from GaTech. All experiments utilize a NACA 4415 airfoil with free stream velocity of 20m/s and $Re = 0.57\text{x}10^6$. *(*) First* C_L *is recorded from static pressure ports with second from load cells.*

As the combustion jet is expected to be a source of significant modeling difficulty, it is worthwhile to examine all details provided [3, 33, 34]. If possible, a greatly simplified approximation will be made. The actuation process is comprised of the formation of two opposite-signed vortices at the edges of the physical actuator which extend well past the boundary layer (≈0.03c) (Fig. 2.1a). Both vortices begin to advect downstream with the upstream positive sign vortex being advected upward and along the boundary of the more downstream negative sign vortex ($0.25t_{conv}$) (Fig. 2.1b). This behavior is consistent with the direction of fluid rotation in the downstream vortex where the fluid is rotating upward and downstream at their interaction region. Subsequently, the positive vortex switches positions and becomes the downstream vortex ($0.28t_{conv}$) (Fig. 2.1c). The positive rotation of the fluid associated with the new downstream vortex causes the trailing vortex to roll-up and

---

[1] web.mit.edu\drela\Public\web\xfoil results available: airfoiltools.com

follow the contour of the airfoil ($0.28t_{conv}$ and onward). The positive vortex is then shed while the now larger negative vortex severs the separation shear layer (0.3-$0.8t_{conv}$) (Fig. 2.1d). The severed shear layer rolls up into a large negative sign vortex and advects into the wake. The remaining negative vortex travels along the airfoil until finally detaching at 0.6c at about $1.8t_{conv}$. The separation point is moved down the airfoil surface by this vortex. The separation region gradually returns to the pre-actuated baseline conditions over a significantly longer time period of about $10t_{conv}$. A requirement for any modeling simplification for the actuator is reproduction of this general (and not simple) post-pulse behavior.

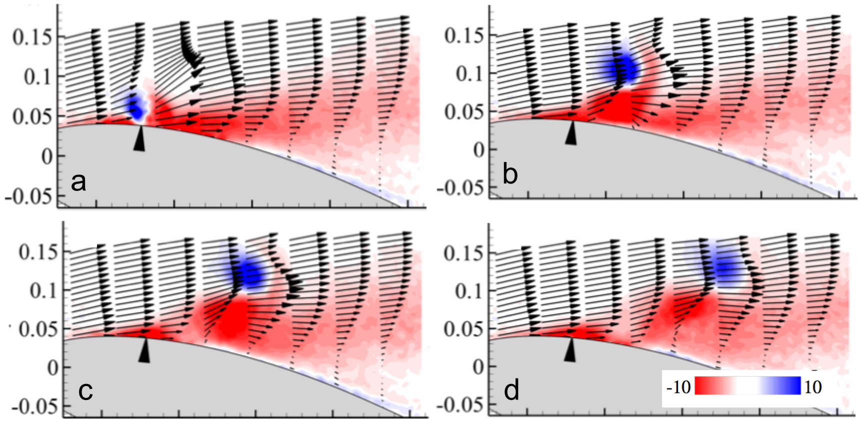

Figure 2.1: Phase-averaged spanwise vorticity and velocity field after application of a single actuation pulse at t_{conv} of a) 0.2, b) 0.24, c) 0.28, and d) 0.32. Reproduced from [2].

Using a single pulse, circulation, as calculated from vorticity flux measured in the near wake[2], is shown to increase by approximately 30% at its peak, which is at about $3t_{conv}$ [13]. Using trains of 10 pulses delayed by a single convective time, the wake circulation enhancement is increased to about 50% with drops of about 10% in-between each pulse [10]. Shorter intervals between pulses is observed to reduce the extent of circulation drop between successive pulses. Using continuous

---

[2] Per a private communication, the exact location and extent over which vorticity flux is measured is not known.

pulses at intervals of t_{conv} and shorter, the corresponding average lift enhancement saturates at approximately 35% [2].

With a finite span actuator covering 21% of the span, and using a harmonic actuation frequency ($St_{act} = 1$), a sustained increase in lift of 10.5% was attained as measured by load cells [14]. Measurements of lift for the same experiment using centerline static pressure ports yield an increase in lift of 21.7%. The difference is attributed to strong 3D affects when using finite actuation zones.

It is important to note that the circulation calculations from measurements in the wake are along a single line and cannot be used to extract a lift. Vorticity measurements along a closed curve would be necessary to use the Kutta-Joukowski theorem. Dynamic body forces for single and multiple pulses are not provided. Therefore, it is only assumed that the long circulation transients directly indicate a similarly long period of increased lift and reduced drag. Additionally, there has been no attention given to the point in the dynamic vortex shedding period and corresponding fluctuating separation point location at which the pulses are applied. This may be significant as the shear layer severing and surface vortex roll-up process appears to rely on the actuator location relative to the separation point. Nonetheless, it is quite remarkable that such enhancements are sustainable from such relatively short actuation periods.

From averaged images we are provided with an important, yet incomplete, description of the underlying mechanisms responsible for reattachment. At best, quantities derived from multiple PIV images are accurate only for a statistically-steady state description of the flow phenomena. They are equivalent to the information discernible from a RANS-based simulation (were RANS models capable of actually modeling the highly anisotropic features being studied). Consummate understanding of the pulsed actuation process requires knowledge of the instantaneous flow conditions throughout the complete process. This is precisely what an LES provides.

Chapter 3

Modeling Background

This chapter discusses modeling techniques and their associated deficiencies. A brief review of RANS and LES are presented with emphasis on Durbin's $\overline{v^2}f$ RANS model [36,37] and Metias and Lesier's structure function SGS model [38] which are both heavily relied on in the development of the new hybrid modeling framework in Chapter 5. For more comprehensive reviews of RANS and LES, the reader is referred to the modern classics of Pope [39] and Durbin [40]. Building on RANS and LES, current hybrid modeling goals and techniques are discussed with emphasis on DES [41]. A comprehensive review of DES is given by Spalart [42] and Mockett [15], only a brief review and discussion of germane issues is presented here. The more recent approach of Perot [43] is covered in greater detail as there have been no applications of this method to complex geometries to date and it provided the launching point for the new method discussed in §5.3.

3.1 The Problem of Turbulence

The oft used description of turbulence as being chaotic and tumultuous fluidic motion belie its underlying order and structure. Turbulence is characterized by a distribution of kinetic energy across a wide spectrum of scales of motion. This distribution is physically manifested in the formation of eddies of varying size and orientation. It is the interactions of these eddies and their accompanying distortions which are responsible for the process of energy transfer from the large energy containing mean and unsteady scales of motion to the small dissipative scales where molecular viscosity transforms coherent structures into random molecular-scale thermal motion. When simulating turbulent flows, we are often only directly concerned with the motion of the large scales yet their accurate prediction requires knowledge of all scales of motion. From the computational standpoint, this is the problem of turbulence.

Direct simulation of the interactions and dynamics of the entire turbulent spectrum is an extraordinarily expensive endeavor requiring computational resources scaling with $\sim Re^3$ and memory storage requirements scaling with $\sim Re^{\frac{9}{4}}$ [39]. For instance, direct simulation of a Boeing 747 at cruising speed for just a few convective times using the fastest petaflop computers available today would take on the order of a million years. Fortunately, though the instantaneous state of turbulence is chaotic, the statistical properties of the motion, and therefore their net effect on the large scales, may be quite predictable. This is due to the formation of the inertial range at high enough Reynolds numbers where the turbulent motion is effected by neither the large nor dissipative scales but only eddies of similar size. Given the statistically consistent behavior in the inertial range, we may formulate turbulence models with very few assumptions. Unfortunately, while inertial range resolution reduces computational resource scaling to only $\sim Re^{\frac{1}{2}}$ in unbounded flow, boundary layer requirements scale with $\sim Re^{2.4}$ [44]. Thus, for flows of engineering interest, we must resort to modeling turbulent scales which are larger than those amenable to universal inertial range theory. This necessitates more complex and geometry-specific models as now the modeled scales are directly affected by the mean and unsteady flow. Review of the different regimes of model resolution is the focus of this chapter.

3.2 Reynolds Averaged Navier Stokes

RANS simulations are designed to directly simulate only the slowly evolving mean field while modeling the effects of all turbulence. Such models use the available information in the resolved field as inputs to predict the statistical behavior of the unresolved scales based on turbulence theory. In this way, we need not devote computational resources to resolving the turbulent scales of motion responsible for transferring energy from the large momentum carrying scales to the small dissipative scales. Under the conditions of relatively simple turbulence where the statistical behavior and therefore the cumulative effects of turbulence are consistent and predictable, RANS simulations can be quite successful in this capacity. However, therein lies the inherent deficiency of RANS, they are only applicable to conditions under which the models are specifically designed for. That is, they are not generally predictive. The structure and evolution of the largest of the turbulent scales are strongly dependent on the presence of boundaries and mean-flow gradients. The evolution of turbulent structure *is* the decay process and is directly responsible for effect of turbulence on the large scales. Therefore, generally applicable RANS models are not attainable and their use should be confined to conditions for which they are specifically designed.

3.2.1 Basic Equations of RANS

Derivation of the mean equations of motion begin with definition of the mean by taking the average of an ensemble of samples from the variable velocity field. The ensemble itself is not strictly defined. Loosely, the interval of sampling which comprise the ensemble is determined by the unsteady frequency of the laminar portion of a specific flow scenario. It is therefore generally a function of time. Under the special condition of a statistically stationary flow, the interval of sampling is irrelevant and the ensemble average is equivalent to taking the time average with $T \to \infty$. The mean of a variable, ϕ, is thus understood as the expected value of the variable as determined by the ensemble average, $\langle \phi \rangle$. Reynolds decomposition is performed on the total velocity field, U_i, yielding contributions from the mean field, $\langle U_i \rangle$, and the fluctuating field, $\langle u_i \rangle = 0$, such that $U_i = \langle U_i \rangle + u_i$. Application of ensemble averaging to the Navier-Stokes equations and noting that it is a linear operation, results in

$$\partial_t \langle U_i \rangle + \langle U_j \rangle \partial_j \langle U_i \rangle = -\frac{1}{\rho} \partial_i \langle p \rangle + \nu \partial_j \partial_j \langle U_i \rangle - \partial_j \tau_{ij}, \tag{3.1}$$

and

$$\partial_i \langle U_i \rangle = 0, \tag{3.2}$$

where $\tau_{ij} = \langle u_i u_j \rangle$ are the velocity covariances or the Reynolds stress tensor resulting from the convective term with $\langle \langle U_i \rangle u_j \rangle + \langle \langle U_j \rangle u_i \rangle = 0$. The form of the mean equations differs from the total equations of motion only in the addition of the divergence of τ_{ij}. The additional term is intended to represents the total action of the fluctuating field on the mean flow. As the only unclosed term in the mean flow equations, representing this term using the available information provided by the resolved field and turbulence theory is the sole focus of RANS modeling.

Definition of the mean using the expected value allows for unsteady $\langle U_i \rangle$. This is commonly referred to as unsteady RANS (URANS). As turbulence is fundamentally different than simple unsteady motion, turbulence models should never be used to account for the effects of unsteady flow features. Whereas turbulence primarily removes momentum, unsteadiness simply moves momentum. There can be no construction of models which account for the effects of unsteady flow; there is no theory which generally accounts for their effects other than conservation of mass and momentum that already constitute the Navier-Stokes equations. The associated difficulty with URANS is that the length and time scales of the unsteady flow features should be larger than those of the largest turbulent fluctuations. This is rarely the case and often results in unintentional misuse of turbulence models. Resolution of enough of the velocity field such that the separation of scales between all unsteady motion and modeled turbulence is achieved is desirable.

The full transport equations for the unclosed Reynolds stress maybe be found by subtracting the mean field equation (3.1) from the total field momentum equation, taking the product of the resulting fluctuating conservation of momentum equation with the fluctuating velocity field, again applying the averaging operation, and adding its transpose. The resulting Reynolds stress transport equation then reads

$$\partial_t\langle u_i u_j\rangle + \langle U_k\rangle\partial_k\langle u_i u_j\rangle = \mathcal{P}_{ij} - \frac{2}{3}\epsilon_{kk}\delta_{ij} - \partial_k\langle u_k u_i u_j\rangle + \nu\partial_k\partial_k\langle u_i u_j\rangle + \mathcal{R}_{ij}, \tag{3.3}$$

where

$$\mathcal{R}_{ij} = \frac{2}{3}\epsilon_{kk}\delta_{ij} - \phi_{ij} - \epsilon_{ij}, \tag{3.4}$$

$$\mathcal{P}_{ij} = -(\langle u_j u_k\rangle\partial_k\langle U_i\rangle + \langle u_i u_k\rangle\partial_k\langle U_j\rangle), \tag{3.5}$$

$$\phi_{ij} = \frac{1}{\rho}(\langle u_j\partial_i p\rangle + \langle u_i\partial_j p\rangle), \tag{3.6}$$

and

$$\epsilon_{ij} = \nu\langle\partial_k u_i\partial_k u_j\rangle. \tag{3.7}$$

In deriving an exact evolution equation for the Reynolds stress in an attempt to close (3.1), additional non-closed terms have appeared in the form of the triple product turbulent transport term and a velocity-pressure correlation term. The process of closure through exact representation of higher-order terms will continually introduce added terms which are inexpressible from the resolved field such that modeling will always be necessary for anything other than DNS. We now briefly review the most basic gradient diffusion model which is used as the basis of the hybrid modeling proposed in §5.2.

3.2.2 Eddy Viscosity

In the same way molecular viscosity represents the net flux of momentum via the random interactions between molecules at length scales characterized by their average mean free path, eddy viscosities represent the net flux of momentum via the interactions between turbulent eddies at characteristic mixing length defined by their size. The Boussinesq turbulence hypothesis

$$\langle u_i u_j \rangle \approx \; -\nu_t(\partial_j \langle U_i \rangle + \partial_i \langle U_j \rangle) + \frac{1}{3}\langle u_k u_k \rangle, \tag{3.8}$$

assumes the Reynolds stress is linearly proportional to the mean rate of strain tensor by a hypothetical "eddy viscosity" which is in turn linearly related to the turbulence intensity and length scale ($\nu_t \sim u_c L$). In addition to the generally incorrect assumption of alignment with mean strain, linear eddy viscosity models result in often completely incorrect behavior under many conditions such as rapidly distorting turbulence or un-strained decaying turbulence [39, 45, 46]. In general, (3.8) fails due to its implicit assumption that the timescales of turbulent equilibrium are much smaller than the mean strain time scales and reliance on ν_t to represent history effects. It is, however, the simplest and remains the most widely used closure of (3.1) to date.

The burden of capturing the complexity of the Reynolds stress evolution evident in (3.3) is placed on ν_t. Though many eddy viscosity models have been proposed [47] which vary in how ν_t is defined, the most common is the k-ϵ model which uses the exact turbulent kinetic energy equation obtained as half the trace of (3.3), and approximates the turbulent transport and redistribution terms using an additional gradient-diffusion model. It also uses the same form as a template for modeling the dissipation equation. The most common form [48] of the two equation system reads

$$\partial_t k + \langle U_j \rangle \partial_j k = \mathcal{P}_k - \epsilon + \partial_j \big[\big(\nu + \tfrac{\nu_t}{\sigma_k}\big) \partial_j k \big], \tag{3.9}$$

$$\partial_t \epsilon + \langle U_j \rangle \partial_j \epsilon = \frac{1}{T}(C_{\epsilon 1} \mathcal{P}_k - C_{\epsilon 2} \epsilon) + \partial_j \big[\big(\nu + \tfrac{\nu_t}{\sigma_\epsilon}\big) \partial_j \epsilon \big], \tag{3.10}$$

where

$$\mathcal{P}_k = -\partial_j \langle U_i \rangle \langle u_i u_j \rangle, \tag{3.11}$$

and the turbulent timescale, T, is defined in terms of the large-scale value (k/ϵ) and the exception for the Kolmogorov limit[1]

$$T = \mathsf{max}\left[\frac{k}{\epsilon}, 6\left(\frac{\nu}{\epsilon}\right)^{\frac{1}{2}}\right]. \tag{3.12}$$

The resulting eddy viscosity is then

$$\nu_t = C_\mu \frac{k^2}{\epsilon} \tag{3.13}$$

where $C_\mu = 0.09$ based on an approximate relation between $\langle uv \rangle$ and k in shear flows where $\mathcal{P} = \epsilon$. The exact equation for the evolution of ϵ (not shown here) is unclosed. The argument for (3.10) follows from the high Reynolds number limit where ϵ is determined by the large scale motions, independent of viscosity, so that it would loosely follow the behavior of k and the mean flow.

3.2.3 Durbin's $\overline{v^2}f$ Model

Eddy viscosity models which approximate the effects of modeled turbulence through k are based on isotropy assumptions, with all turbulence properties (correlation length and time scales) invariant to orientation. In region of flow anisotropy, they are destined to fail. The quintessential example of their shortcomings is in boundary layers where they will drastically over-predict turbulent stresses. Typically, the remedy has been to introduce ad-hoc wall damping-functions which are tuned to some set of data [50, 51]. These models become generally non-predictive with their short-comings particularly exposed in cases of flow separation. Eddy viscosity formulations using the wall normal component of the Reynolds stress as opposed to the trace have been shown *a priori* to greatly enhance the near wall accuracy of the general model form using DNS data [52]. The challenge to formulating such models is then to determine near wall anisotropy in $\langle u_i u_j \rangle$ without employing full Reynolds stress modeling (RSM).

---

[1] The stagnation point anomaly correction of Durbin [49] is also used for T_m and L_m in the subsequent simulations presented in Chapter 6 and Chapter 7.

Instead of resorting to arbitrary wall-damping functions, Durbin's $\overline{v^2}f$ RANS[2] model directly accounts for near-wall effects through a redistribution of streamwise turbulent kinetic energy [36]. Of the full Reynolds stress transport equation (3.3) only the wall-normal component ($\overline{v^2} = \langle u_n u_n \rangle$) is considered in addition to the standard models for the turbulent kinetic energy (3.9) and dissipation (3.10). The corresponding unclosed redistribution tensor ($\mathcal{R}_{ij}$) is modeled based on an assumed form of the velocity-pressure gradient correlation term ($\langle u_i \partial_j p \rangle$). If the correlation of the velocity and pressure diminishes due to statistical decorrelation between eddies of increasing separation and due to distance from a source in the pressure field, the term will behave elliptically as a modified Helmholtz operator of the form $\nabla^2(\cdot) - \frac{(\cdot)}{L^2}$ where the correlation distance has been assumed to be constant. A model for $kf = \mathcal{R}_{nn}$ is proposed as

$$L^2 \nabla^2 f - f = \frac{1}{T}(C_1 - 1)\left(\frac{v^2}{k} - \frac{2}{3}\right) - C_2 \frac{\mathcal{P}_k}{k} \tag{3.14}$$

where the source term follows from the Rotta model for the slow part of $\mathcal{R}_{ij}$ and the Isotropization of Production (IR) model of Launder *et.al.* [53, 54] for the fast portion ($C_1 = 1.4$ and $C_2 = 0.3$). The Rotta model simply assumes a return to isotropy at a rate of $1/T$ while the IR model assumes anisotropy in $\mathcal{P}_{ij}$ (3.5) diminishes at a rate proportional to the production itself. Substituting kf for $\mathcal{R}_{ij}$ into (3.3) for the wall-normal component with the standard eddy diffusivity closure for $\partial_k \langle u_k u_i u_j \rangle$ results in

$$\partial_t \overline{v^2} + \langle U_j \rangle \partial_j \overline{v^2} = kf - v^2 \frac{\epsilon}{k} + \partial_j \left[\left(\nu + \tfrac{\nu_t}{\sigma_k} \right) \partial_j \overline{v^2} \right]. \tag{3.15}$$

where it has been assumed production is in balance with dissipation. Additionally, the separation of k and f in (3.14) assumes that k is homogeneous. The latter two assumptions speak to the quasi-homogeneous form of the $\overline{v^2}f$ model. That is, were the spatial gradients of $\langle u_i u_i \rangle$ are on the same order as the gradients of anisotropy, the model may be seen as being questionable. However,

---

[2] In the RANS context $\overline{v^2}$ should be written as $\langle v^2 \rangle$ to be consistent with the ensemble average symbol used here. However, overbar notation is customary with the $\overline{v^2}f$ model and as we will use this model later on in the context of a filtered variable, $\overline{v^2}$ will be used throughout.

Durbin described the model as more of a “template for elliptic relaxation” which allows near-wall induced anisotropy to be introduced into second moment closure models through boundary conditions on f [40]. Indeed, the $\overline{v^2}f$ model and its variants have been validated over a wide range of incompressible [36,55] and transonic [37,56] flows without the need for tuning which is commonplace in k-ϵ and k-ω models.

3.3 Large Eddy Simulation

Large eddy simulations offer an attractive compromise between accurate yet computationally expensive DNS and computationally efficient yet often inaccurate RANS modeling. In theory, an LES resolves turbulent structures of interest while not requiring resolution of the smallest and most numerically expensive features. For high enough Reynolds number flows, their is a separation of scales from the large energy containing scales to the small dissipative scales. Between these lies the inertial range, unaffected by viscosity and boundary conditions, which transfers energy from the large to small scales. Small scale features tend to be isotropic and their only practical importance is how they effect the large scale turbulent characteristics. The *effect* of small scale turbulence may be modeled, thus alleviating the need to simulate all scales of the flow.

Typical LES models are formulated based on the assumption of isotropic unresolved turbulence in equilibrium with the large scales and isotropic LES filtering. When one or more of these assumptions is violated, poor performance results [42]. In typical LES application to complex flows, all three of these conditions will often be violated due to grid resolution being strongly anisotropic and inhomogeneous, with the LES resolution quite coarse making subgrid isotropy and equilibrium unlikely. Inhomogeneous resolution leads to commutation error terms in the filtered Navier-Stokes equations [57] that have not generally been accounted for in LES models. The result is that fluctuation energy is not appropriately transferred between resolved and unresolved turbulence as the turbulence convects through changes in resolution or filter scale [58]. With anisotropic grid resolution, the effective subfilter diffusivity is anisotropic as well, with higher diffusivity associated with the coarsely resolved directions[3]. Using an isotropic subfilter viscosity model (*e.g.* Smagorinsky) will result in under-resolution in the coarse directions and/or over-resolution in the fine direction. Finally, when the subfilter turbulence is anisotropic, subfilter diffusivity will also be anisotropic. Isotropic eddy viscosity models will similarly result in nonphysical evolution of the resolved fields.

Separation of scale breaks down near discontinuities where the local Reynolds number becomes small such as at solid boundaries and shockwaves. In these cases, the large scales of interest *are* the small dissipative scales. In fact, any region of locally laminar flow is problematic for an LES. Many current SGS models rely on parameters which are determined *a priori* or dynamically during the simulation using spatial averaging even though it has been shown that these values are highly local and vary significantly in DNS [59]. Additionally, the assumptions of many SGS models lead to non-physical behavior under certain circumstances such as being overly dissipative in the vicinity of walls [44] or preventing physically possible back scatter of energy from the small scale to the large scale [60]. In order for LES to become a useful engineering and predictive tool, several issues must still be resolved.

3.3.1 Basic Equations of LES

LES is formulated by applying a filter, $\overline{(\cdot)} : f \to \overline{f}$, to the Navier Stokes equations to truncate the solution space to only those scales of motion above the filter cut-off size, Δ_c. The effects of the discarded scales are recovered through filtering the convective term in the form of a subfilter stress tensor, τ_{ij}. The resulting incompressible LES evolution equations are

$$\partial_t \overline{U}_i + \overline{U}_j \partial_j \overline{U}_i = -\frac{1}{\rho}\partial_i \bar{p} + \nu \partial_j \partial_j \overline{U}_i - \partial_j \tau_{ij} \tag{3.16}$$

---

[3] That is, the most coarse grid size does not necessarily coincide with the most coarsely resolved orientation

$$\partial_i \overline{U}_i = 0 \tag{3.17}$$

$$\tau_{ij} = \overline{U_i U_j} - \overline{U_i}\,\overline{U_j} \tag{3.18}$$

where it has been assumed the filter commutes with differentiation. The filtering operation $\overline{(\cdot)}$ for uniform filter size described by Δ_f is formally defined as the convolution of the total field with the selected filter G

$$\bar{f}(\xi) = \frac{1}{\Delta_f}\int_{-\infty}^{\infty} G\left(\frac{\xi - \eta}{\Delta_f}\right) f(\eta) d\eta. \tag{3.19}$$

Though any low-pass filter could be applied to the Navier Stokes equations to arrive at (3.16), the grid resolution is most often employed corresponding to an implicit spatial top-hat filter. The total velocity field would then be a combination of the filtered field and the discarded fluctuating field, $U_i = \overline{U_i} + u_i'$[4]. The resolved field of (3.16) is itself a fluctuating variable containing turbulent fluctuations in addition to unsteady fluctuations, this is one of the main differences between LES and RANS. Closure of the system is achieved by modeling (3.18) in terms of the resolved field giving rise to subgrid stress models.

It is relatively straight forward to extend the ideas of eddy viscosity models developed originally for RANS modeling to SGS models. This is certainly the simplest approach and we can expect the increased isotropy of the unresolved small scale turbulence in SGS models to be more amenable to simple eddy viscosity models than their RANS counterparts, since the latter attempts to model the turbulent stress over all scales. While there have been many proposed method of LES equation closure such as full SGS transport modeling [61], probability density function modeling [62], subgrid field construction through small scale vortices [63], and implicit LES where stabilization of the filtered Navier Stokes is achieved numerically with no regard for the actual turbulent SGS term [64] to name a few, we focus on eddy viscosity type models here in preparation for later consideration of

---

[4] Note: $u = u_{res} + u'$ where $u_{res} = \overline{U} - \langle U \rangle$ is the resolved turbulent velocity field.

hybrid models which blend between RANS and LES.

Smagorinsky related (3.18) to the filtered strain rate tensor $\bar{S}_{ij} = \frac{1}{2}(\partial_j \overline{U}_i + \partial_i \overline{U}_j)$ through an eddy viscosity as

$$\tau_{ij} = -2\nu_T \overline{S}_{ij} + \frac{1}{3}\tau_{kk}\delta_{ij}, \tag{3.20}$$

$$\nu_T = (C_s\Delta)^2|\overline{S}|, \tag{3.21}$$

where C_s is the Smagorinsky constant, $\Delta = \Delta_f$ is a measure of the grid size, and $|S| = (2\overline{S}_{ij}\overline{S}_{ij})^{1/2}$. The same assumptions discussed in §3.2.2 apply here. Though multiple Smagorinksy constant values have been proposed, Lilly derived a scale invariant $C_s = 0.23$ for isotropic turbulence with inertial range Δ by enforcing the balance between production and dissipation [65]. However, a universal Smagorinsky constant is not effective at describing a wide range of flow conditions as it relies on Δ being firmly in the inertial range to achieve isotropy and homogeneity. Near walls, for instance, this constant value is overly dissipative and requires correction using wall damping functions. This problem arises from the eddy viscosity overwhelming molecular viscosity where the former should vanish. Additionally, ν_t in (3.21) is always positive and thus, always dissipative. In some cases, such as large scale vortex growth through Kelvin-Helmholtz instability, small scales may transfer energy to the larger scales [66].

Germano *et.al.* first introduced a dynamic C_s to enhance the predictive capability of the Smagorinsky model [67]. While these dynamic coefficients have been largely successfully, especially at correcting behavior for regions of laminar flow, such as the viscous sub-layer, averaging in homogeneous directions is typically necessary to avoid large variations in C_s causing instabilities. This reduces how "dynamic" it really is as well as restricting its application to more simple flows which contain directions of homogeneity to average over.

Despite these short comings, the dynamic Smagorinsky model and its modification by Lilly [68] have been used successfully in a variety of simple flows [69]. In fact, a frequent comment amongst the LES community and literature is how remarkable it is that such a simple model has been so successful. As discussed in (§B.1), all SGS eddy viscosity models are approximations of the fluctuating portion of (3.18), $\overline{u_i' u_j'}$. These models all approximate the magnitude of the term from the modeled estimation of the fluctuating component, $(u')^2$, with anisotropy in τ_{ij} following directly from the filtered velocity gradient. Where they differ is in their approximation of $(u')^2$. For an improved method of determining the magnitude of $\overline{u_i' u_j'}$, we now examine the more complex structure function based SGS.

3.3.2 The Structure Function SGS

All turbulence models draw on the information provided by the resolved field to make some inference of the effects of the unresolved turbulence. The structure function SGS model is unique in that it relies upon exact relations between the resolved and unresolved fields from the theory of isotropic homogeneous turbulence. The two-point velocity correlation tensor, $R_{ij}(r_k) = \langle u_i(x_k) u_j(x_k + r_k) \rangle$, is a rich source of information about a turbulent flow. For instance, as $r \to 0$, the Reynolds stress tensor is recovered. Of interest to the construction of SGS models is its relation to the turbulent energy spectrum, Φ_{ij}, as

$$R_{ij}(r_m) = \int_0^\infty \Phi_{ij}(\kappa_m) e^{i\kappa_m r_m} d\kappa, \tag{3.22}$$

where κ_i is the wave vector and for incompressible isotropic turbulence, Φ_{ij}, can be expressed in terms of a single scalar function $E(|\kappa|)$, the so-called three-dimensional energy spectrum

$$\Phi_{ij} = \frac{E(|\kappa|)}{4\pi|\kappa|^4}(|\kappa|^2 \delta_{ij} - \kappa_i \kappa_j). \tag{3.23}$$

Through (3.22), knowledge of R_{ij} is equivalent to knowledge of the distribution of turbulent energy across all length scales. From a filtered field, only the portion of the total R_{ij} associated with resolved scales is known. Thus, formulating SGS models may be approached from the perspective of approximating the total correlation tensor as opposed to modeling the unresolved scales.

While the two-point correlation includes the small-scale information needing modeling, it is not convenient for LES modeling because for small separation, it's value is dominated by the large scale turbulent kinetic energy rather than the energy in the small scales. The same information is provided in a more convenient form in the second-order structure function F_{ij} defines as:

$$F_{ij}(r_m) = \langle \delta u_i \delta u_j \rangle, \tag{3.24}$$

where $\delta u_i = u_i(x_m, t) - u_i(x_m + r_m, t)$ and [70]

$$F_{ii}(r_m) = 4 \int_0^\infty E(|\kappa|) \left(1 - \frac{sin(|\kappa| r)}{|\kappa| r} \right) d|\kappa|. \tag{3.25}$$

While (3.25) essentially contains the same information as (3.22)[5], velocity differences across a separation distance that are much less than the scale over which the mean varies automatically removes its contributions.

The structure-function subgrid stress model (SF-SGS) of Metias and Lesieur [38] (3.27) determines the unresolved contribution to the total structure function by assuming a Kolmogorov inertial range which extends from κ_c to ∞ (infinite Re condition). Through this assumed spectrum and (3.25), a relation between the total unresolved kinetic energy and the filtered structure function is obtained (derivation in §B.3). A spectral wavenumber-dependent eddy viscosity is proposed of the form

$$\nu(\kappa, \kappa_c) = \nu^{+}(\kappa, \kappa_c) \left(\frac{E(\kappa_c)}{\kappa_c} \right)^{\frac{1}{2}}. \tag{3.26}$$

Upon transforming to physical space, an average eddy viscosity makes use of F_{ij} to approximate the effects of all unresolved turbulence over all resolved scales as

$$\nu(x, t) = 0.105 C_k^{\frac{3}{2}} \Delta \overline{F}_{ii}(x, \Delta, t)^{\frac{1}{2}}, \tag{3.27}$$

---

[5] For example, $R_{ij}(0)$ is recovered as $F_{ij}(r \rightarrow \infty)$

where C_k is the Kolmogorov constant, Δ is the grid spacing, and $\overline{F}_{ii}$ is the filtered contracted structure function (composed with $u - u'$ rather than u) related to the total structure function through a constant dependent on the ratio r/Δ ($F_{ii} = 2.53\overline{F}_2$ for $r = \Delta$).

Though seemingly more complex, the structure-function model varies only slightly form standard Smagorinsky-type models. Consider the standard algebraic subgrid stress models in the form of a resolved fluctuating velocity scale times a characteristic turbulence length scale defined by the grid. For instance, the Smagorinsky model (3.21) may be rearranged as $C\Delta(\overline{S}_{im}\Delta_{mj}\overline{S}_{in}\Delta_{nj})^{1/2}$ where $\Delta_{ij} = \Delta\delta_{ij}$. The product of the strain tensor and grid size is the resolved change in velocity at the filter length scale (as implied by the grid) in every direction ($\delta u^S_{ij}|_\Delta$) due to strain. Applying δu^S_{ij} to a unit vector, e_i, yields the total change in velocity across a separation distance defined by the grid in the direction of e_i, *i.e.* $\delta u^S_i(r_j) = \delta u^S_{ij} e_j$ where $r_j = e_j\Delta$ for a separation with magnitude Δ. Therefore, we may express Smagorinsky as

$$\nu_{sgs} = \sqrt{2}C\Delta|\delta u^S|, \tag{3.28}$$

where $|\delta u^S|$ is the magnitude of the resolved change in the velocity field at a separation distance of Δ due to strain alone. Comparing (3.28) with (3.27) and (3.24), we see the structure-function model is of the same general form. Where it differs is in its inclusion of rotational deformation in its estimation of the unresolved turbulent kinetic energy through velocity differences. Analysis of DNS has shown dissipation to be concentrated in both converging-diverging zones where strain is dominant and in eddies where vorticity dominates irrotational strain [71]. In many circumstances, the net effect of the vorticity may be recovered through a tuned coefficient in models based solely on strain. However, the structure of the smallest scales of resolved turbulence becomes even more questionable as the effects of vorticity are redistributed to regions of straining. Further, it is reasonable to assume the SF-SGS will outperform Smagorinksy in flows in which rotation is generally important in addition to straining motion.

3.3.3 Grid Inhomogineities

The discretization of complex geometries (or simply non-trivial geometries) necessitates heterogenous grid spacing. If the filtering operation in (3.19) is completely unrelated to the grid and associated derivative operators while also being everywhere larger than the grid, a homogeneous filtering operation may be applied everywhere. Where this is not true and given a filter which does not commute with differentiation, heterogeneous filter widths introduce additional errors into the LES formulation. As discussed by [58], these errors arise from the neglect of extra terms arising from non-commutivity and filter gradients as

$$\overline{\frac{\partial \phi}{\partial x}} = \frac{\partial \bar{\phi}}{\partial x} - \frac{\partial \Delta_f}{\partial x}\frac{\partial \bar{\phi}}{\partial \Delta_f}, \tag{3.29}$$

where Δ_f is the characteristic filter size. Thus, applying a heterogenous filter to the gradient of a field requires knowing both the gradient of the actual filter and the response of the filtered field to changing filter widths. The latter is not expressible as a function of the filtered field alone introducing an additional closure problem. Every spatial derivative in the implicit grid filtered LES equations introduces error when the second term in (3.31) is neglected.

Ghosal [57] examined this problem by defining a function which maps a variable grid spacing onto a uniform grid, $f : x \to \chi$, such that the variable spatial filter width, $\delta_f(x)$, is related to uniform spacing equal to the filter size as $\delta_f(x) = \frac{\Delta_f}{f'(x)}$. By introducing a change of variables to the field, $\psi(\chi) = \phi(f(x))$, the standard uniform filtering operation may be applied (3.19) to the new field. The resulting commutation error ($\mathcal{C}[\psi] = \overline{\frac{d\psi}{dx}} - \frac{d\bar{\psi}}{dx}$) is

$$\mathcal{C}[\psi] = \frac{1}{\Delta_f}\int_a^b G\left(\frac{f(x) - f(y)}{\Delta_f}\right)\psi'(y)f'(y)\left(1 - \frac{f'(x)}{f'(y)}\right)dy. \tag{3.30}$$

Upon expanding each terms of the integrand of $\mathcal{C}$ in powers of Δ_f and discarding odd-terms (G is symmetric), the filtered gradient may be expressed in terms of the local filter spacing as

$$\overline{\frac{d\psi}{dx}} = \frac{d\bar{\psi}}{dx} - \alpha\delta_f\left(\frac{\delta_f'}{\delta_f}\right)\frac{d^2\bar{\psi}}{dx^2} + \mathcal{O}(\delta^4), \tag{3.31}$$

where α is related to the filter type and size as

$$\alpha = \int_{-\infty}^{\infty} \zeta^2 G(\zeta) d\zeta, \tag{3.32}$$

and $\zeta = \frac{f(y)-f(x)}{\Delta_f}$. For a Gaussian filter, $\alpha = \frac{1}{4}$, for a top-hat $\alpha = 1$. When (3.31) is applied to the material derivative, the advective portion takes the form of an additional artificial diffusion term with "viscosity" resulting from the advective velocity and resolution gradient.

The heterogeneous filter commutation errors have been shown to be $\mathcal{O}(\Delta^2)$. When using a second-order numerical scheme we may be tempted to declare them negligible. Before doing so, let us examine the action of these errors in the context of an LES. In the same work [57], Ghosal analyzed its spectral distribution using channel flow with hyperbolic tangent grid spacing, revealing introduction of phase errors growing with wavenumber to a maximum at the cutoff. As opposed to standard central differencing errors in the convective term which are purely dispersive, variable filter widths result in either amplification or damping of the field depending on whether the filter is increasing or decreasing in the flow direction, respectively. When the direction of the advection is aligned with the filter gradient direction, the associated errors are amplified. In the context of high speed flows for which LES are typically applied, even mild grid gradients can translate to large variable filter errors. Further, it is important to realize errors that arise from filtering and numerical discretization are not isolated. For instance, when the filter width is increasing in the advection direction, heterogenous filter errors will amplify the magnitude of dispersion errors resulting from central differencing. To summarize, when the scales of motion of interest are on the order of the available resolution and the local resolution-based Reynold's number is much greater than unity, correction for heterogeneous filtering should be implemented. These conditions represent the exact conditions for which LES was designed.

3.4 Hybrid Methods and their Deficiencies

Hybrid models are a response to the limitations of available computational power for decades to come. Barring a computational revolution, complete resolution of all turbulent scales (DNS) will not be achievable for practical engineering flows until the turn of the next century [72]. At the opposite end of the spectrum, modeling of all turbulence while only simulating the slowly evolving mean flow (RANS) is well within current computational capabilities but suffers from numerous inadequacies [42, 47, 73]. Of paramount importance to this study, RANS is insufficient to accurately model geometry specific features in unsteady separation and wakes. While potentially capable of simulating transient flow features, unsteady RANS (URANS) still suffers from the shortcomings of RANS and is based on the assumption of non-turbulent unsteadiness time scales being greater than the largest turbulent time scales, which is seldom the case [74]. Large eddy simulation may be thought of as a compromise between complete simulation and complete modeling of turbulence. For high Reynolds number flow where there is a separation of scales between large energy containing eddies and small universal eddies, LES is an efficient and accurate compromise from a DNS. In the presence of strong flow anisotropy and in areas of low Reynolds number, such as near a wall, the benefits of an LES are lost. In these cases, requirements for resolution of the energy containing eddies are nearly identical to a DNS. Hybrid methods are a recognition of the limitations of currently available techniques and resources. Simply, LES is performed where computationally feasible with modeling, typically RANS, performed elsewhere.

Hybrid methods function by detecting if the local grid is capable of resolving some of the turbulence. Where this is found to be true, the modeled stress is reduced thereby allowing the formation of resolved turbulence and operation as an LES. The various methods of hybrid modeling differ in how they attempt to ascertain the adequacy of the local resolution to support simulation of turbulence and how the modeled stress is reduced in response. An ever growing list of hybrid models have been proposed and modified with varying degrees of overlap and success [75]. Indicators used to induce hybridization include comparisons of resolved and modeled turbulent kinetic energy [43], SGS and RANS eddy viscosities [76,77], and length scales. The latter is by far the most common and involves comparing a measure of the grid to the internal model length scale [78–81], Kolmogorov length scale [82,83], or wall distance [41,44,84]. The reduced hybrid model stress used in the conservation of momentum is then either a weighted combination of the full model stress and the subgrid stress or results from a hybridized version of the full model equation. That is, the resolution indicator is used to blend the results of distinct full and SGS model equations or it is used to internally blend the model equation so that it may function as both. Blending between distinct RANS and SGS models requires additional averaging of the resolved field such that the RANS equations remain consistent. Alternatively, RANS and LES operation may be segregated by zones such that a region of LES operation is embedded in a RANS [85,86]. The spatial interface is either fixed beforehand or dynamically adjusted throughout the simulation. In these cases, it is this interface which is either blended or coupled in some manner. Originally proposed and demonstrated by Spalart in 1997 [41], detached-eddy simulation (DES) and its variants [79–81,87,88] are the most pervasive and exhibit the common issues seen in many hybrid models. It will therefore be used as an exemplar and discussed in further detail.

3.4.1 Detached Eddy Simulation

In a DES, the internal length scale of a RANS model is modified based on its comparison with a scalar measure of the grid resolution. Where smaller than the local RANS length scale, this grid length scale, modified by a tuned constant, is used in its place. Length scale substitution reduces the source term (production less destruction) of the RANS equation, causing it to function as an SGS model with eddy viscosity scaling with Δ_{grid}^2 as opposed to L_{RANS}^2. The result is a local LES. The commonly used single equation Spalart-Allmaras (SA) [89] family of models use the wall distance while other models have a length scale determined by their scalar model variables (*e.g.*

$L_{RANS} = k^{3/2}/\epsilon$ for $k\epsilon$). For instance, the first proposed DES [41] used the SA model

$$D_t\tilde{\nu} = \mathcal{P}_{SA} - \frac{f(\tilde{\nu})}{L_{DES}^2} + \frac{1}{\sigma_{SA}}\partial_i\big((\nu+\tilde{\nu})\partial_i\tilde{\nu}\big) + C_{SA}\partial_k\tilde{\nu}\partial_k\tilde{\nu} \tag{3.33}$$

with hybridization accomplished by the length scale switch $L_{DES} = \min(d_{wall}, C_{DES}\Delta_{grid})$. Two or more equation models where the internal length scale does not explicitly make an appearance in any equation (like wall distance in SA) will have another scalar fixed by the LES length scale (*e.g.* $\epsilon_{DES} \sim k^{3/2}/\Delta_{grid}$ for $k\epsilon$).

In massively separated flows for which DES was originally intended, this hybridization approach can function well [15]. However, in more complex scenarios, such as smooth-wall separation, length scale switching is insufficient to properly govern the transition from full RANS to reduced levels of modeled turbulence (i.e., LES regions). Ad hoc corrections are often proposed for such cases. For instance, so-called “delaying” functions have been used with some success to prevent premature flow separation along smooth walls [87]. However, there is little theoretical justification for the form of this correction, and it requires additional coefficient tuning, rendering the models non-predictive for flows they have not been calibrated for. These deficiencies are typically attributable to the so-called “grey area problem” [42], where switching to LES operation results in “stress depleted” regions of no resolved turbulence and drastically lower modeled turbulence. Indeed, it is primarily this problem that leads to poor predictions of smooth wall separation. Let us examine this scenario in detail as it is of particular importance to the simulation of complex flows.

An intrinsic requirement of DES is that the transition from RANS to LES occurs outside the boundary layer. The main point of DES is to avoid LES grid requirements to simulate small streak-like eddies in the attached boundary layer. However, depending on the LES length scale definition and underlying grid, transition to LES operation may occur in a turbulent boundary layer. A particularly bad grid LES length scale definition is the cubic root of the cell volume ($(\Delta x\Delta y\Delta z)^{1/3}$) [79, 90, 91].

This definition has the wholly undesirable behavior of favoring the *smallest* dimension of the grid. When used in boundary layers with highly stretched cells, this definition tends to the wall-normal spacing. A DES will interpret this as an indication that the grid can support a properly resolved LES, which it cannot. The problem is exacerbated in the case of smooth-wall separation as there will be a lack of resolved turbulence in the highly refined boundary layer mesh immediately after the separation point. The result is so common amongst DES and hybrid methods that is termed “grid induced separation”, the result is premature detachment of boundary layers or reduced skin friction.

The main deficiencies of DES and other hybrid methods can be understood as follows. First, a simple scalar measure of the available resolution using the grid is insufficient. Multiple measures have been used and interchanged as dictated by whatever happens to give the best results. In general, some will favor the largest length across a cell (cell diagonal) and others the smallest (cube-root of the cell volume). None faithfully represent the effects of anisotropy and inhomogeniety in the grid which are unavoidable in complex geometries. This leads to the second main problem, using the grid size alone to determine available resolution implicitly assumes the *instantaneous* presence of resolved content at that precise grid scale. This is the root of the "grey area problem". Transition from RANS to LES occurs without consideration for the state of the resolved flow. Premature transition in attached boundary layers is partially due to neglect of the large resolved gradients in favor of a dubious measure of high-aspect ratio cells.

Other challenges to predictivity in hybrid models are related to the underlying RANS model. For instance, the use of any RANS model with wall-damping functions requires additional ad hoc corrections to suppress their activation away from walls. Taking DES as an example again, the most commonly used RANS model is the Spalart-Allmaras (SA) model [89]. The SA model not only contains many empirical closure functions dependent on distance to the wall but also uses the distance to the wall as its internal length scale. As the grid size is generally smaller than wall distance everywhere except very close to the wall, the result is LES mode of operation whether the grid can actually resolve any of the turbulence. Additionally, the use of the SA model results in a SGS model whose production scales with the magnitude of the rotation tensor. The resulting SGS in regions of a flow experiencing primarily symmetric distortions (an expanding jet, for example) will be under predicted. The deficiencies outlined here regarding the standard SA model in a DES provides just one example of how there is no one current "best" model which is applicable to a wide variety of flow and geometric situations.

Finally, the last major challenge to the success of hybrid models is the oft neglected general issue of commutation errors in the discretized Navier Stokes equations (§3.3.3) [57, 58]. If a resolved flow structure is convected through a coarsening grid such that the characteristic lengthscale of the structure becomes smaller than the grid, dispersion errors result causing the structure to lose coherency. Spalart acknowledged this in his guide for DES grid construction [92] where he advised only gradual changes in grid size to prevent non-physical build-up or removal of energy at high wave numbers. Thus, this final issue is due to grid inhomogeniety. As with anisotropy, grid inhomogenieties are unavoidable in complex geometries.

3.4.2 Perot Hybrid Method

As mentioned in the previous section, many hybrid models completely neglect the current state of the resolved field when transitioning from RANS to LES. Recently, Perot and Gadebusch [43] proposed a hybrid framework which considers the resolved turbulent content when transitioning. They begin by noting that while the theory behind RANS and LES may be fundamentally different, the final forms of their equations are mathematically identical . The only requirement for both sets of equations is that the velocity field can be split into two parts and that the splitting operation commutes with differentiation. It is therefore natural to construct a closure model which adapts without any discrete transition between theoretical regimes. They propose a simple modification whereby the model viscosity appearing in conservation of momentum and the production term in the k equation of k-ϵ are multiplied by a backscatter coefficient, α.

$$\partial_t \overline{U}_i, + \partial_j(\overline{U}_i \overline{U}_j) = -\partial_i \overline{p} + \partial_j\big((\nu + \alpha\nu_t)\partial_j \overline{U}_i\big), \tag{3.34}$$

$$\partial_t k + \overline{U}_j \partial_j k = \alpha\mathcal{P} - \epsilon + \partial_j\Big(\big(\nu + \tfrac{\nu_t}{\sigma_k}\big)\partial_j k\Big), \tag{3.35}$$

with the ϵ evolutions equation the same as in (3.10). Further, the typically constant $C_{\epsilon 2}$ is in (3.10) replaced with a function varying from theoretical limits of 11/6 at high turbulent Reynolds numbers to 3/2 at low turbulent Reynolds numbers ($Re_T = k^2/\nu\epsilon$) [93].

$$C_{\epsilon 2} = \frac{11}{6} f + \frac{25}{Re_T} f^2 \tag{3.36}$$

$$f = \frac{Re_T}{30}\left(\sqrt{1 + \frac{60}{Re_T}} - 1\right) \tag{3.37}$$

The backscatter coefficient is determined by some measure of the adequacy of grid resolution for the local instantaneous flow. If the grid is capable of resolving additional unsteadiness or turbulence, energy from the turbulence model is returned to the resolved scales via some α less than unity. The lower bound on α should be selected with not only realizability constraints (k bounded above zero) but also so that energy returned to the resolved scales can be redistributed to a physically realistic state from the somewhat unrealistic state resulting from a reduction in diffusion. Through the interchange of increased resolved content and reduced model kinetic energy, α will tend to a quasi-steady value dependent, yet not directly determined by, the local grid size. It should be noted that any value of α less than this quasi-steady value may represent backscatter, not just negative values.

The difficulty of the Perot method lies in choosing a proper resolution indicator and how α should scale with this variable. In the original work, an indicator constructed from the total resolved turbulent kinetic energy, its gradients, and grid size with a final backscatter coefficient of the form

$$\alpha = 1.5\left\{1 - C\left(\frac{k}{k+k_r}\right)\left[\left(\frac{\Delta_i}{\sqrt{k_r}}\sqrt{k_r}_{,i}\right)^2 + 0.11\right]^{-1}\right\}, \tag{3.38}$$

where $k_r = \frac{1}{2}(u_i - u_i')(u_i - u_i')$ and $(u_i - u_i')$ is the resolved fluctuating field, was used for demonstration on isotropic homogeneous turbulence in a periodic box. This form essentially considers the ratio of modeled to total turbulent kinetic energy modified by the presence of the grid-weighted divergence of resolved turbulence. While successful for their simple demonstration problem where the mean velocity is zero, application to complex flows of engineering interest becomes troublesome. Either time or spatial averaging will be needed to attain a measure of the resolved turbulence. The timescale over which to average is not clear in unsteady flows and consistent spatial averaging is difficult with complex geometries with varying grid densities. Additionally, in the boundary layer, while k_r goes to zero, so does its gradient. The indicator becomes ill-defined and boundary layer operation in full RANS mode will not be preserved. Further, (3.38) contains many empirical coefficients resulting in the aforementioned problem of nonpredictivity.

Finally, [43] also modified the standard eddy viscosity definition with the ratio of modeled to total turbulent energy,

$$\nu_t = C_\mu \frac{k^2}{\epsilon}\left(\frac{k}{k+k_r}\right). \tag{3.39}$$

While this modification does achieve the desired behavior in the limits of full modeling and full simulation, it has no theoretical justification and is inconsistent with the central ideas of reduction of model stress being controlled by the backscatter coefficient. The necessity of this additional reduction in model viscosity indicates the form of (3.38) does not have the correct dependance on the resolved field.

Despite the above identified issues, the Perot methodology is an attractive starting point for developing a hybrid modeling framework. It addresses the transition from RANS to LES operation in a less invasive manner than DES. With the addition of the backscatter coefficient the turbulence model is hybridized with consideration for both the resolved gradients and local grid size. If applied properly, this hybrid framework should replace the need for ad-hoc transition and shielding functions as well as alleviate the grey area problem. Chapter 5 describes how this can be achieved.

Chapter 4

Simulation Background

This chapter presents previous attempts and lessons learned from simulating dynamic stall control experiments using DDES (§3.4). The simulations performed follow from wind tunnel experiments at GaTech presented in §2.2. Through these attempts, many of the deficiencies with DES and hybrid modeling in general as presented in §5.1 were identified. Relevant numerical simulations of stall control in the literature are also reviewed.

4.1 Numerical Studies of Stall Control

While there are many numerical studies of general stall, particularly at high angles of attack, simulations of dynamic stall control, by any means, are sparse. A brief review of synthetic jet simulations is presented in [94] and no further attention to this type of jet is given here. The precursor to the current work [95] was later found to contain a coding error which masked modeling deficiencies and invalidated all its dynamic stall and reattachment results.

Charles Mockett performed a series of DES evaluations with various models and their parameters [15]. While the flow scenarios used in this study were comparatively basic, some findings can at least be used as a starting point in formulating the proposed modeling approach which are summarized next. The SA family of models require the addition of a low Reynolds number correction to prevent activation of wall damping functions away from the wall. Without the correction, substantial accumulation of energy at high wave numbers was observed. Excessive damping is still present with SA models in early shear layers for separated flows even with the correction. DES showed strong sensitivity to temporal filtering leading to recommendation of CFL numbers being constrained to unity. For massively separated flows as occurs on an airfoil at 60^o angle of attack, DES is largely insensitive to the underlying RANS model. However, for channel flow with a smoothed 35^o backward-facing bump, the separation location, recirculation region, and reattachment were found to be strongly altered by the selected RANS model. Using large values of the DES length scale constant, C_{DES}, in DIT caused an earlier roll off of energy near the cutoff wavelength. This is to be expected as larger C_{DES} essentially amounts to a larger LES filter (though the situation may be more complicated depending on the model). What was not an expected result is that an increase in energy at lower wavenumbers was also observed with large C_{DES}.

The work of Höll *et.al.* [96] is perhaps the most closely related to the proposed work. In their study, pulsed blowing of varying intensity, frequency, and arrangement were used to enhance lift of a trailing flap at $\alpha = 37^o$. Aerodynamic enhancements were attributed to a combination of longitudinal (streamwise) vortex generation which entrained high momentum fluid from above the separation layer and an increase of the circulation around the entire airfoil through the pulsed injection of fluid almost tangential to the surface. This increased circulation causes the boundary layer to be more resistant to adverse pressure gradient. Narrowing of the blowing slots resulted in increased performance though this effect was only explored up to incompressible limits. While not discussed by the authors, this is likely a result of increased blowing velocity rather than a direct geometric effect. Pulsed blowing out-performed harmonic actuation for most configurations with peak lift enhancements of 55% and 35%, respectively. Alternating blowing between adjacent slots was seen to damp lift enhancement to a nominal value with a slight overall increase for pulsed actuation. As mentioned earlier, SA-based DES suppressed shear layer instabilities and were deemed inadequate to simulate pulsed blowing reattachment while the linear-local realizable (LLR) $k - \omega$ [97] based DES performed acceptably to the authors standards. It should be noted, there was no comparison to experimental results.

In the work of You *et.al.* [98], a NACA 0012 airfoil at $Re = 8.96\text{x}10^5$ and angles of attack of 16.6° and 20° with harmonic synthetic jets are simulated using only LES. The simulations are directly comparable to the experiments of Gilaranz *et.al* [99] which show a suppression of stall from 12° to 17° resulting in an increase in lift of 0.8 to 1.4 at 16.6°. General details of the grid are as follows; the first boundary grid height is cited as $2\text{x}10^5$c with streamwise spacing from $2.84\text{x}10^{-4}$c to $3\text{x}10^{-3}$c at the airfoil surface and spanwise spacing of $5.6\text{x}10^{-3}$c. Total grids sizes of $8\text{x}10^6$ and $15\text{x}10^6$ over a domain of $6c \times 2.44c \times 0.2c$ with well resolved jet orifice and trailing edge are studied. (Preliminary work in this proposal use very similar grid details). The dynamic single test filter SGS model used in this work is based upon the Vreman model [100] and the double-test filtered dynamic modification of Park *et.al* [101]. The Vreman model features properly vanishing eddy viscosity in laminar flow regimes such that no wall damping functions are necessary. It is quite remarkable that the pure LES implementation not only accurately predicts mean body forces using harmonic synthetic jets at both angles of attack but also exhibits grid convergence towards the experimental values. There is no mention of GIS, MSD, or any further modifications to the model. The only drawback is the need for a test filter which is not straight-forward for complex geometries.

4.2 Previous SA-based DDES Experience

Described below are initial efforts to simulate the pulse actuated reattachment process using SA-based DDES, with the goal of reproducing the reattachment process from a single pulse with a spanwise uniform actuation zone in 2D and 3D. Issues and deficiencies are identified and used in the following section to formulate model improvements.

Given that turbulence is necessarily three dimensional, as is LES, 2D DES has fundamental deficiencies. Nonetheless, 2D DES can be used as a starting point to establish requirements for 3D simulations (grid, length scale, *etc.*) at considerable computational savings. Additionally, it is not clear what scale of flow features need to be resolved to properly simulate the reattachment process. It is probable that the dominant mechanisms causing flow reattachment is the actuation-induced spanwise vorticity interaction with the separated boundary layer which is a 2D effect for a short time after actuation. Thus, 2D simulations should be sufficient to determine adequate grid density and appropriate model length scale definition.

Simulations are performed in conditions similar to those at GaTech, (NACA 4415 airfoil at 20° AoA, Re of 0.57x10^6), approximations and modifications are as follows. The pulse is modeled as in [95] with a Dirichlet boundary condition of $8.8U_\infty$ applied for $0.05t_{conv}$. Maximum CFL numbers are ≈ 2. The grid is an O-mesh of radius 10c with initial wall normal spacing of 2x10^{-5} and wall tangent spacing varying from 1x10^{-4} around the actuator to 5x10^{-4} on the pressure side. Local cell Reynolds numbers based on total viscosity and diagonal cell length are, in general, well above unity. The pulse is approximated as a simple uniform Dirichlet boundary condition consistent with the net actuation momentum flux over $0.05t_{conv}$. Given that the pulse generated by the COMPACT system is a very hot mixture of combustion products and is sonic, this is a severe idealization. This crude treatment is based on the assumption that vortex formation resulting from momentum injection is the critical contribution of the pulse.

The boundary condition for the SA model's $\tilde{\nu}$ during actuation requires special attention. During the pulse, this value is convected from the actuation zone and largely determines the overall shape of the initial actuation structure by strongly influencing the structure's viscosity levels. Too little $\tilde{\nu}$ at the actuation zone and the structure will break-up prematurely, too much and pulse-induced vorticity will be greatly attenuated. This boundary condition approximates the effects of the entire turbulent stress of the actuation pulse resulting from combustion and can therefore be expected to be quite high. A value of $\tilde{\nu} = \frac{1}{4}\nu$ (or $4.5\text{x}10^{-7}c^2/t_{conv}$) was found to produce a reasonable approximation of the pulse structures observed in GaTech experiments as previously described. However, the complete roll-up of positive vorticity is not seen indicating a higher pulse inlet model viscosity may be necessary.

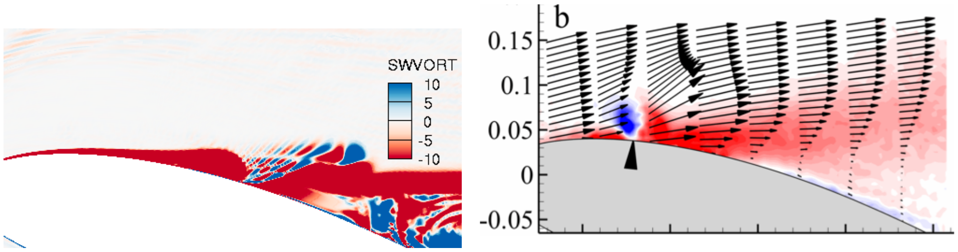

(a) Simulation (b) GaTech experiment

Figure 4.1: Comparison of simulated 2D actuation with SA-standard model and experimental phase-averaged PIV [2] near-actuation region at $0.2t_{act}$. Color bar scales are identical.

Unfortunately, there are no experimental PIV images available of the immediate actuation region just after the pulse has completed. This information would be greatly beneficial as a direct validation of the actuation approximation. The earliest image available is at $t_{act} = 0.2$ (Fig. 4.1). Comparison with 2D simulations shows substantial disagreement. The magnitudes of spanwise vorticity are significantly higher in the simulation. This may be due to the averaging that has been performed on the PIV data which indicate a high degree of spatial variability in the data. Additionally, the structures are completely different. The simulation shows a distinct roll-up of negative vorticity and suffers from dispersion error causing "ringing" in-between the pulse structure and the shear layer. The experimental image shows a positive vorticity region maintaining a position at the actuator while the simulation has already shed this structure by this time. Despite the disagreement at times shortly after actuation, the 2D simulations produces similar reattachment to experiments, as will be discussed next.

With a single pulse, the general reattachment process is successfully reproduced using 2D SA-based DDES (Fig. 4.2). An LES lengthscale floor, in which the LES resolved scales are defined significantly larger than the local grid size near the wall, was necessary to achieve satisfactory baseline flow and reattachment (discussed in detail later). The mean baseline lift coefficient is observed to be 1.8 which exceeds the average values reported by GaTech (Table 1). This discrepancy is likely due to the simulation being 2D. The reattachment process centers around the interaction between opposite-signed vorticity regions and the wall (Fig. 4.2a). A strong negative-signed vorticity region is created by the initial pulse. This structure is responsible for (i) walking the separation point down the airfoil surface (Fig. 4.2a-b) and (ii) pulling up a trailing region of positive vorticity which both severs the leading negative vorticity region into a coherent vortex and causes the trailing negative vorticity region to roll-up (Fig. 4.2b-c) . The leading negative vortex is then shed into the wake (Fig. 4.2d) leaving the trailing negative vortex to repeat the process of walking the the separation point downstream and creating a positive vorticity region in its own wake (Fig. 4.2e-f) . This process is continued for an extended time with return to stall not observed by $10t_{conv}$ after application of the pulse when the simulation was stopped. It is clear that such prolonged reattachment is due to the simulation being 2D which prevents real 3D turbulence from breaking-up the actuation-induced structures causing them to be unrealistically stable. However, it is likely that the early reattachment process is dominated by 2D-effects and that the identified mechanism is accurate.

For a finite volume based 2D simulation, the resolved scale in the direction normal to the simulated plane is essentially infinite and should have no affect on the results. This simple observation indicates that the model length scale definition should be independent of spanwise resolution in

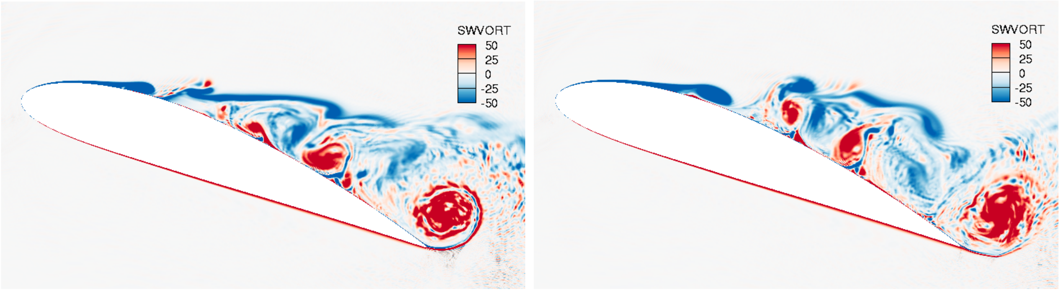

(a) $0.1t_{act}$

(b) $0.3t_{act}$

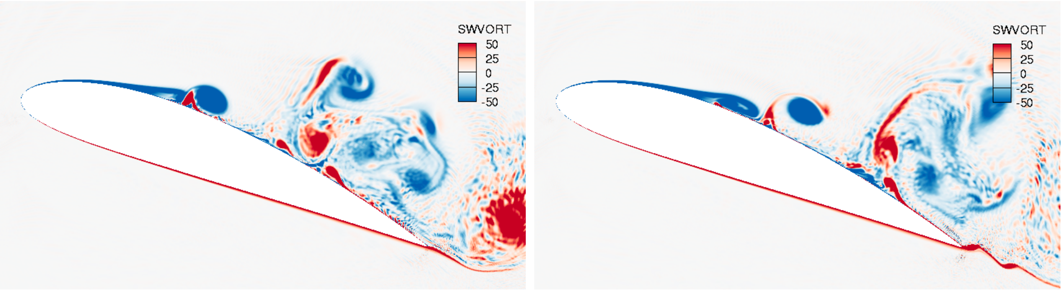

(c) $0.5t_{act}$

(d) $0.7t_{act}$

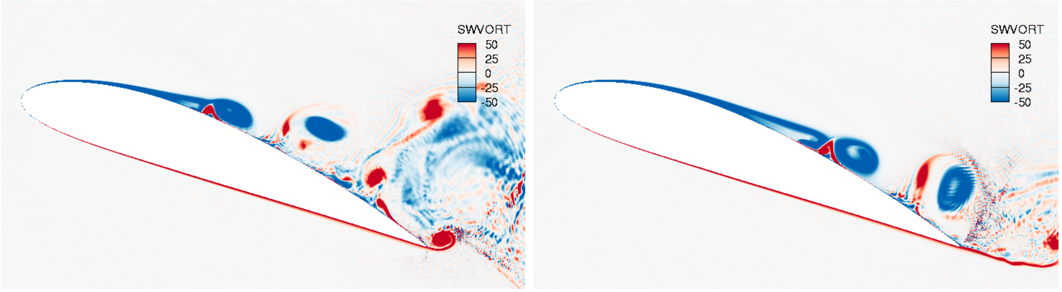

(e) $0.9t_{act}$

(f) $4.0t_{act}$

Figure 4.2: Spanwise vorticity details of reattachment process using 2D SA-standard DES simulation after application of a single actuation pulse. The actuation pulse is applied from convective time (t_c) of 0 to 0.05 with a slot width of $6.6\text{x}10^{-4}c$ *at a position of* $x = 0.15c$ *and a normal velocity of* $8.8U_\infty$. *The flow is brought to a quasi-steady state from an initial uniform field over* $30t_c$.

this case. The typical length scale definition as cell diagonal or the cube root of the cell volume is replaced by the simulation plane cell diagonal. The model length scale may be further modified to be larger than the local cell face diagonal (corresponding to a larger filter width) and may be limited to some length such that there is a consistent resolved scale in the region of interest rather than the constantly varying length scale introduced by directly linking the length scale to the underlying grid. The effects of such LES length scale definitions on the coefficient of lift for both baseline stall and actuation are shown in Figures 4.3 and 4.5.

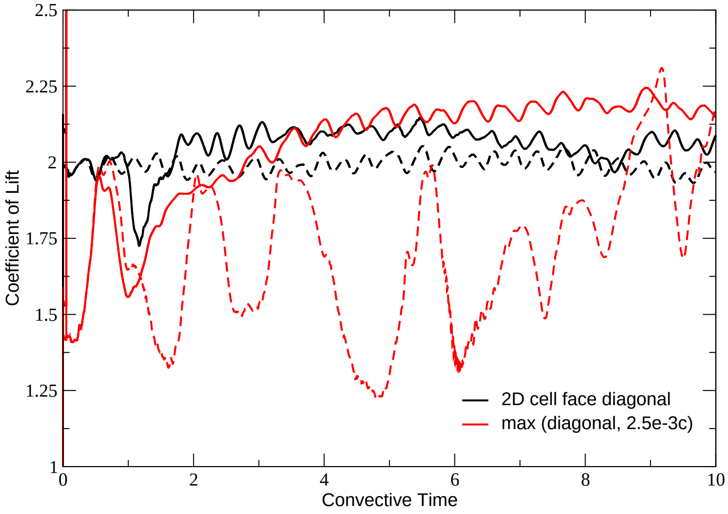

Figure 4.3: Coefficient of lift for baseline stall (- -) and pulse actuation (—) of NACA 4415 airfoil at 20° α, Re of 0.57×10^6*. LES length scale is set to the local cell diagonal (black) and the maximum of the local diagonal and* 2.5×10^{-3} *(red).*

Figure 4.3 reveals the sensitivity of DDES to small changes in length scale definition. The drastic change in baseline behavior (black line) is due to the small change in LES length scale definition as seen in Fig. 4.4. With the local actuator resolution allowed to dictate local transition to LES, the attached boundary is tripped causing the shear layer to roll-up and the entire baseline flow to enter an overly-stable mode of behavior similar to that initiated by the pulse. This behavior results from premature and local transition to LES from RANS operation, The vortex shedding frequency is very high and the oscillation in C_L is very mild which is inconsistent with dynamic stall. Additionally, the mean lift is well above any of the available experimental data (see Table 2.1).

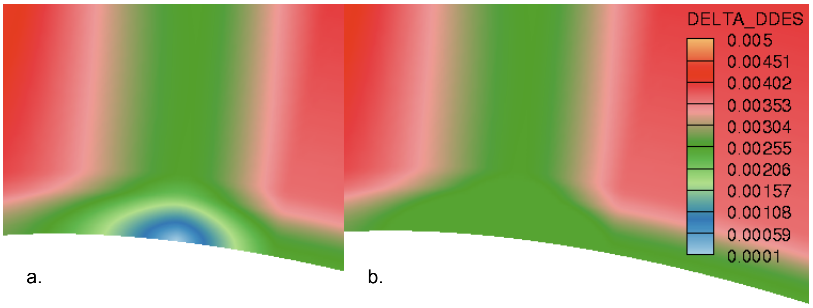

Figure 4.4: LES length scale fields in near-actuator region for (a) cell diagonal and (b) maximum of cell diagonal and $2.5\text{x}10^{-3}$*. Similar differences occur in the trailing edge and stagnation point regions.*

Figure 4.5 shows there is a critical flow feature size which must be resolved to capture the reattachment process. With the LES length scale floor set to $10\text{x}10^{-3}c$, the pulse has little effect on the flow as the associated model eddy viscosity washes out the critical actuation induced vortices. Additionally, the mean lift is again above the experimental data. However, where the diagonal-defined LES lengthscale (black line Fig. 4.3) caused the baseline behavior to behave similar to the pulse-induced behavior, the larger length scale floor simply makes the solution behave as in a RANS simulation.

Dictated by 2D feature resolution requirements, 3D simulations are performed with a grid of 10 cells in the spanwise direction of length 0.0025c. Such a spanwise spacing along with the cell diagonal definition of the LES length scale field automatically imposes a “floor” similar to the optimal case identified in 2D. Such a relatively small total spanwise domain means these simulations are only modestly 3D. Ideally, the spanwise domain would be identical to experiments with a grid spacing

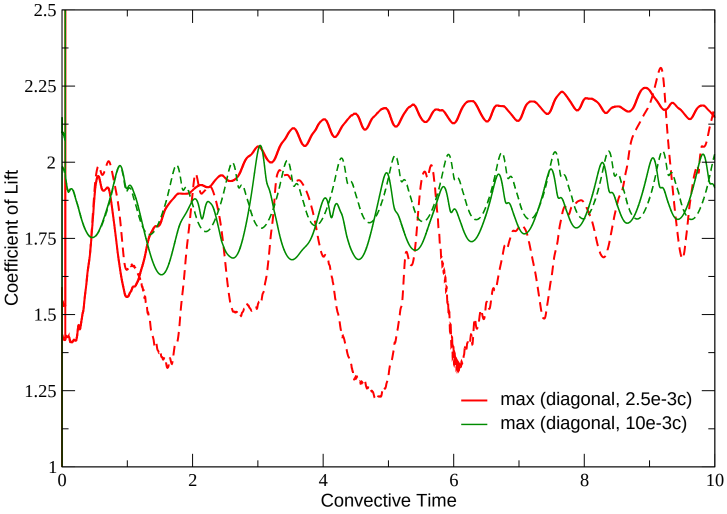

Figure 4.5: Coefficient of lift for baseline stall (- -) and pulse actuation (—) of NACA 4415 airfoil at 20° α, Re of $0.57\text{x}10^6$*. LES length scale is set to the maximum of the local diagonal and* $2.5\text{x}10^{-3}$ *(red) and the maximum of the local diagonal and* $1.0\text{x}10^{-2}$ *(green).*

equivalent to the streamwise direction. Computational expense discourages this, at least for this preliminary work.

Lift enhancement for the 3D simulation is presented in Fig. 4.6. As previously discussed, 2D simulations show large lift enhancements for extended convective times, 3D shows only a minimal increase in lift with return to baseline behavior after only approximately two convective times. The reason for this is clear when examining the pulse-induced structures (Fig. 4.7). A pulse-induced leading negative vortex is observable in experiments (4.7a) and is successfully reproduced in 2D (4.7b). Despite the crude COMPACT actuator model used in the simulations, it is encouraging that such subsequent large scale features appear to be accurate in 2D. However, this apparently critical feature is rapidly broken-up in 3D simulations even though the pulse structure immediately after actuation

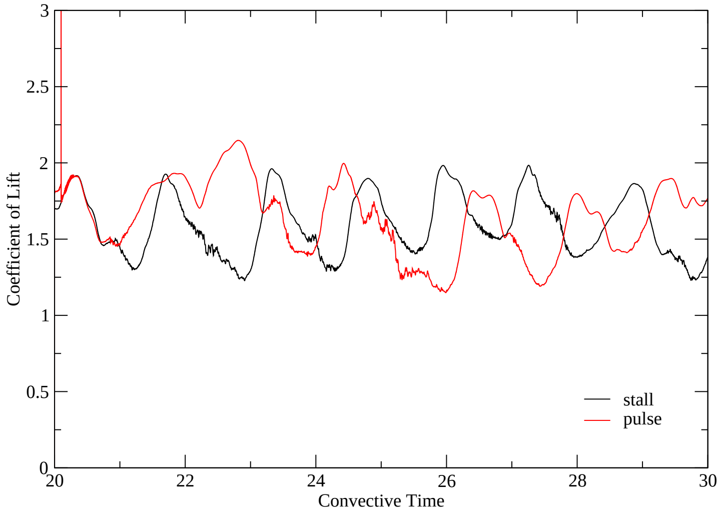

Figure 4.6: 3D SA-standard DDES coefficient of lift for baseline stall (black) and pulse actuation (red) of NACA 4415 airfoil at 20° α, Re of $0.57\text{x}10^6$*. Flow conditions are identical to previous 2D simulations with a spanwise domain of 0.025c using 10 cells.*

is very similar in 2D and 3D. This premature break-up is likely due to artificial amplification of 3D turbulence resulting from spurious oscillations associated with under-resolved LES. The severing and roll-up of negative vorticity in the shear layer occurs in both 2D and 3D simulations. This common feature in two simulations with only one producing reattachment is an indication that this process is inconsequential for reattachment.

To avoid modeled stress depletion, relatively large cell sizes are recommended in boundary layers [92]. This is not possible when small features are present, such as the actuator. Even with the use of the delaying function of Spalart [87], an LES length scale floor must be imposed to prevent GIS. The ad-hoc delaying function essentially dictates where and how the flow will separate from a smooth wall. Slight changes of the constants used in this delaying function results in drastically different

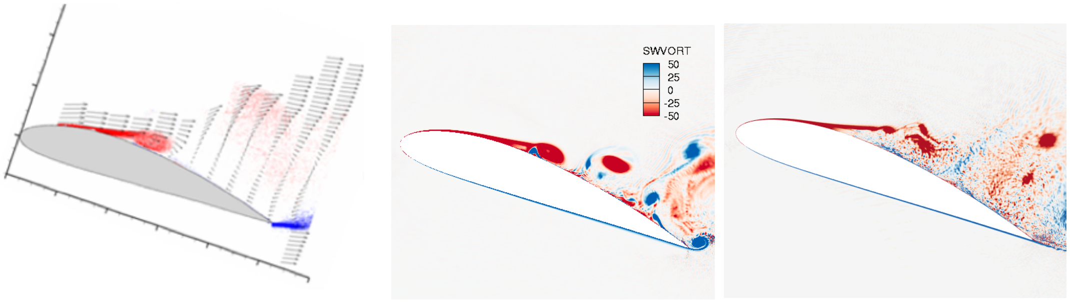

(a) PIV

(b) 2D

(c) 3D

Figure 4.7: Normalized spanwise vorticity $1.0t_{conv}$ *time after application of a single pulse (a) PIV measurements [3] (b) 2D SA-based DDES, and (c) modestly 3D SA-based DDES. The pulse-induced vortex responsible for initiating reattachment is clearly visible in both (a) and (b) while having lost coherency in (c). This deficiency of DDES is due to incorrect turbulence modeling for necessarily anisotropic grids.*

separation behavior. Essentially, one can dictate the flow behavior by altering these completely non-physical parameters. The model loses it predictive capability and becomes, for the most part, useless.

The failure to simulate the reattachment process in 3D is due to one of the main deficiencies with DDES. DES uses a scalar length scale measure of the physical grid and compares this to a scalar measure of the total large scale turbulence length scale. This comparison does not account for anisotropy in the grid or flow. Both the grid and the flow are highly anisotropic, especially near the actuator. The result is an inconsistent and inappropriate comparison of the relevant turbulence and grid length scales. Transition from RANS to LES suffers greatly and manifests in the need to introduce “patches” such as shielding functions or length scale floors. Such ad-hoc corrections may break-down in many scenarios. In our case, transition to LES was premature, resulting in amplification of dispersion error via three-dimensionality.

Exacerbating the transition problem, the SA model uses wall distance as its internal length scale. When compared with a measure of the grid size, the simulation will transition to SGS-type operation without regard for the grid support of an LES. The result is overly-reduced model viscosity away from the wall with accompanying dispersion error. This is visibly observable with “ringing” in 2D simulations. In 3D, these errors behave like enhanced turbulence via three-dimensional exchange of momentum and tear-up of coherent structures.

A basic assumption of DES is that the LES region will behave as with the Smagorinsky model when the flow is in equilibrium ($\nu_t \propto |S_{ij}|\Delta^2$). Wall terms in the SA model are supposed to be suppressed with the use of the aforementioned low Reynolds number correction. However, we have observed these terms remain significant throughout all resolved structures in the separation region. Therefore, the SA model is not an appropriate candidate for use as an SGS or in DES.

Chapter 5

A New Hybrid Modeling Approach

This chapter describes a new modeling and hybridization approach developed to solve commonly observed problems in hybrid simulations of turbulence in complex geometries, which require inhomogeneous and anisotropic meshes, and which typically include problematic flow features such as dynamic smooth wall separation. First, a structure-function-based subgrid stress model which accounts for anisotropy in both the LES resolution and resolved turbulence is presented. This model in turn informs the development of a hybrid RANS/LES formulation where modeled turbulence is returned to resolved scales by reduced model viscosity until a balance between theoretical and actual modeled turbulence intensity is attained for the available resolution. Additionally, a general viscosity-based correction is proposed for grid/resolution inhomogeneities. Both the hybrid framework and resolution gradient corrections conserve energy through an exchange of resolved and modeled turbulence energy. We anticipate the approach will address critical barriers to the predictivity of CFD for important engineering systems like those identified in the Grand Challenge problems outlined in the NASA CFD Vision 2030 Study [12].

5.1 General Approach

The hybrid RANS/LES modeling approach presented in the following sections address the previously identified challenges faced by both LES and hybrid RANS/LES models. Some of these challenges were identified as described in §4.2 through application of DDES [87] to the simulation of a separation flow control concept [3, 10, 13, 14] over the last several years. The critical challenges can be summarized as follows and will be later referred to as **C1-C5**.

1. Grid size alone is an insufficient and often misleading measure for accessing adequacy of the available resolution to support resolved turbulence;
2. Transition from RANS to LES must allow the resolved field to evolve naturally and maintain a statistically meaningful state;
3. Anisotropy in both the filter and the resolved field must be incorporated in the model;
4. The model must account for the changes in evolved turbulence caused by flow through gradients in the filter scale;
5. And the underlying turbulence model should respond to boundaries without explicit dependence on wall distance nor reliance on ad hoc treatments so that the model can remain valid in attached, separating/transitional, and detached regions.

To construct a hybrid modeling formulation that can robustly simulate complex engineering flows, these issues must be addressed. Our general approach is discussed next.

The goal of a hybrid RANS/LES simulation is to directly simulate turbulent features of particular interest in an LES mode of operation while modeling everything else using RANS. Significant computational savings are achieved by modeling costly regions, such as attached boundary layers, while still providing useful information about more complex unsteady turbulent flow structures whose effects RANS is often unsuccessful at modeling. The transition and interaction between RANS and

LES is governed by what may be referred to as a *hybridization framework*. The goal of a hybridization framework is to ensure as much physically meaningful[1] turbulence is simulated as possible given the available resolution. However, how much of the turbulence is actually represented as in LES does not depend solely on the local resolution. Instead, the balance between resolved turbulence and modeled turbulence is dynamic. Consider, for example, turbulence that is being convected from a region in which the local resolution only supports RANS to a region in which LES is supported. As the turbulence passes from one region to the other, turbulent kinetic energy should be transferred from representation by the model to representation as resolved turbulence. The hybridization framework needs to effect this transfer, but, if the resolved turbulence is to be physically realistic, the transfer can not occur too rapidly, so that the resolved turbulence will be able to equilibrate as it is introduced. This effectively sets a maximum rate at which energy transfer can occur. This is the main reason for the issue **C1**. This issue is commonly ignored in hybrid models, and the result is local modeled stress depletion, which can spoil the solution globally due to its effect on the mean.

We address this issue of evolving resolved turbulence (**C1**) by comparing a theoretical estimate of the unresolved turbulence energy, based on the two-point second-order structure function (3.3.2) as approximated by the state of the resolved turbulence at separations defined by the available resolution, to the modeled representation of unresolved energy. By driving these two measures of unresolved turbulence toward consistency through exchange of energy between resolved and unresolved turbulence, at a rate limited by the turbulent timescale (**C2**), statistically consistent turbulence will be produced without corruption of the large scales of motion.

Anisotropy of the grid and resolved turbulence (**C3**) is directly included in the theoretical estimation of the unresolved turbulence used to drive hybridization so that the *least resolved* orientation

---

[1] By "physically meaningful" it is implied the statistics of the resolved field are consistent with the theory being used to approximate the effects of the unresolved field.

will be considered rather than simply the smallest grid measure. In this way, we ensure enhanced turbulence resolution will only be attempted where is can be supported in every orientation of the grid. Furthermore, the anisotropy determined from the theoretical estimates can be built into the hybridized model when in LES modes of operation, ensuring full utilization of the available resolution in every direction. That is, resolution and associated computational expense in a more resolved orientation will not be wasted due to the existence of a coarser direction.

The issue of rapidly changing resolution can be viewed from the perspective of a variable filter width applied to the LES equations of motion (3.16) (§3.3.3). Based on the commutation error model of [57], we introduce a subgrid stress model response to convection through generally anisotropic resolution inhomogeneity (**C4**). The response rate is limited by the timescales of turbulence at the cutoff to be consistent with the overall requirement of an energy conserving exchange between resolved and modeled scales. The model assumes the form of an anisotropic artificial viscosity and is therefore easy to integrate into the existing hybrid framework. Further, it may be used in conjunction with the comparisons of estimated and modeled unresolved energy to influence hybrid transition behavior.

Finally, without resorting to full Reynolds stress modeling, only the $\overline{v^2}f$ model of Durbin provides a consistent physics based representation of near-wall effects (§3.2.3). As $\overline{v^2}f$ is founded upon the standard k-ϵ model, its use as the base turbulent model for the hybrid framework is straightforward and offers robust near-wall behavior for smooth-wall separation and reattachment (**C5**). Representation of turbulent structures as in LES of attached, separating, and detached regions of flows experiencing smooth-wall separation and reattachment is not amenable to near-wall corrections tuned to reproduce attached boundary layer statistics. Such ad-hoc treatments limit the validity of the entire model to when the flow is firmly within in one regime, most likely fully attached. They will corrupt the fidelity of resolved near-wall structures elsewhere. Additionally, estimates of the unresolved turbulence using $\overline{v2}$ obviate hybrid wall distance based delaying functions [87] as they are naturally reduced in the presence of attached boundary layers.

In the following sections, we discuss each of these developments in detail.

5.2 Anisotropic SF-SGS model

With the goal of developing models generally applicable to complex geometries and flows, we now extend the scalar SF-SGS to account for anisotropy in both the grid and resolved field. This is achieved by first introducing a tensor description of filter resolution, $\mathcal{M}_{ij}$, and second, approximating the structure function (3.24) as a linear composition of this tensor and the resolved gradients. This extension removes the implied assumption that velocity differences across a separation distance are independent of orientation in (3.27) and provides the most complete description of the structure function with separation at the filter scale that is possible given all available information.

The structure function of (3.24) can be evaluated at separation distances as defined by a tensor measure of the local grid as opposed to a single scalar distance. This generally anisotropic tensor, $\mathcal{M}_{ij}$, can be understood in terms of a local transformation from coordinates in which the grid resolution is isotropic with unit resolution to the physical coordinates. Let $\mathcal{J}$ be the Jacobian of this transformation, then $\mathcal{M} = (\mathcal{J}^T \mathcal{J})^{\frac{1}{2}}$. This is similar to the mapping from a unit master element to a global element in finite element methods[2]. The anisotropic resolution scale, $\mathcal{M}$, is analogous to Δ in (3.27) and as with Δ, we can choose to define it independently of the grid resolution (provided the grid resolution is fine enough), or we can define $\mathcal{M}$ in terms of the local grid cell geometry. This flexibility can be used to prevent changes in grid resolution from adversely affecting resolved flow

---

[2] See §**??** for a description of determining $\mathcal{M}$ for the finite volume code used in this work

structures in regions where the grid resolution is finer than necessary to resolve the desired scales, which often occurs in meshing complex geometries.

Using a linear approximation of the velocity differences at separation $\mathcal{M}$ based on the resolved velocity gradient, the filtered two-point, second-order structure function can be approximated by

$$Q_{ij} = \frac{\partial \overline{U}_k}{\partial x_m} \mathcal{M}_{mi} \frac{\partial \overline{U}_k}{\partial x_n} \mathcal{M}_{nj}, \tag{5.1}$$

where Q is the anisotropic tensor analog of $\overline{F}_2$ representing the structure function and assuming $\bar{u}_i$ is filtered to scales consistent with $\mathcal{M}$, $e_i Q_{ij} e_j$, where $\mathbf{e}$ is an arbitrary unit vector, is an estimate of $|\delta u|^2$ where δu is the velocity difference between points separated by $\mathcal{M}_{ij} e_j$. This relation will be discussed further and made use of in the following section (§5.3). Were the contraction in velocity indices to be dropped, the resulting fourth-rank tensor would describe the full orientation-dependent two-point second-order structure function with separations described by $\mathcal{M}$. Though this form contains a great deal of information, it is entirely unwieldy to use in practice and we will use the contracted form on which the SF-SGS is founded.

In [38], the authors suggest approximating the condition average of the structure function by averaging over a stencil of four neighboring cells in every direction. For unstructured meshes, this becomes impractical. For this reason, we will use instantaneous values of (5.1) and approximate the net effects of averaging using a multiplicative constant. As we will see later in Chapter 6, this constant is found to be simply $\frac{1}{3}$.

Using (5.1) and (3.27), an anisotropic eddy viscosity tensor, ν_{ij}, can be formulated. The simplest model for the subgrid stress tensor τ_{ij} in terms of ν_{ij} is given by

$$\tau_{ij} = \nu_{jk} \partial_k \overline{U}_i + \nu_{ik} \partial_k \overline{U}_j. \tag{5.2}$$

Under the conditions of an isotropic and diagonal eddy viscosity, (5.2) collapses to the standard Boussinesq eddy viscosity model (3.8). However, where this is not true, the principle axis of the SGS tensor are no longer assumed to be aligned with those of the filtered strain tensor and is affected by the anisotropy in the filter itself and the entire velocity gradient tensor. While τ_{ij} is still symmetric, the terms on the RHS of (5.2) are in general not symmetric. This is due to the inclusion of changes in rotational deformation in the structure function which is preserved in its approximation through Q. This is not to say rigid body motion is included in approximating the effects of the unresolved field, just *changes* in rigid body motion are. These last points are significant departures from the standard eddy viscosity model.

There are several possible ways to write ν_{ij} in terms of the velocity gradient tensor and $\mathcal{M}$. First, the scalar form given in (3.27) suggests

$$\nu_{ij} \sim Q_{ik}^{\frac{1}{2}} \mathcal{M}_{kj}. \tag{5.3}$$

Another possibility is suggested by the fact that the physical space form (3.27) results from spectral expression $\left(\frac{E(k_c)}{k_c}\right)^{\frac{1}{2}}$, which suggests a more natural form is

$$\nu_{ij} \sim \tilde{Q}_{ij}^{\frac{1}{2}} \tag{5.4}$$

where $\tilde{Q}$ is defined

$$\tilde{Q}_{ij} = \mathcal{M}_{im} Q_{mn} \mathcal{M}_{nj} \tag{5.5}$$

Both forms are evaluated in §6 with (5.5) found to be the slightly superior form of anisotropy. Thus, the final form of the proposed anisotropic algebraic SGS eddy viscosity is

$$\nu_{ij} = \frac{0.105}{3} C_k^{\frac{3}{2}} \tilde{Q}_{ij}^{\frac{1}{2}}. \tag{5.6}$$

As will be discussed in the following sections, the anisotropy representation developed here will be integrated into both the estimate of unresolved turbulence for driving hybridization and also incorporated into the final hybrid model form.

For the most part, existing so-called "anisotropic" treatments [69, 102] do not have filter anisotropy directly built into the structure of the SGS model as we have done here. Instead, adjustments to the scalar measure of the modeled turbulent velocity scale are made to consider filter anisotropy while the final model still adopts anisotropy from the filtered strain. The Clark model [103] takes anisotropy directly from the approximation of the modeled velocity scale using a contraction in the gradient indices (instead of velocity indices as in Q_{ij}) as $\tau_{ij} \sim \Delta^2 \partial_k \overline{U}_i \partial_k \overline{U}_j$. Clearly, (5.1) could be rearranged similarly so that filter anisotropy would be directly incorporated into the Clark model. The rationale for doing so is to construct a direct model for the Reynolds stress tensor. However, consistent with the original findings in [103], doing so results in a model where the constant must be artifically set to zero when the model becomes anti-diffusive to preserve stability. The likely reason for this necessity is that there is no simple scaling relation between the filtered anisotropic velocity gradients and the unresolved anisotropic Reynolds stress (such as in the isotropic homogeneous structure function (3.25)). Such arbitrary "clipping" of model coefficients is highly undesirable when trying to construct robust and physical models. However, returning to this formulation, perhaps in conjunction with the the form represented by (5.1) to construct the combination of filter anisotropy and Reynolds stress anisotropy, is an intriguing possibility for future research.

5.3 RANS/LES Hybridization

The Perot and Gadebusch (§3.4.2) modification to the Reynolds stress term in the conservation of momentum equation and the corresponding production term in the modeled turbulent kinetic energy equation based on a blending parameter, α, serves as a starting point for developing a hybridization scheme. This simple modification achieves the goal of being conservative and allowing free exchange of energy between resolved and modeled scales. However, due to drawbacks discussed in §3.4.2, the other components of the specific approach detailed in [43] are not used. In the following, we develop a more general formulation for the blending parameter and utilize the anisotropic subgrid stress model developed in §5.2.

5.3.1 Blending Formulation

The blending parameter proposed here is formulated to drive the estimate of unresolved energy based on the state of the resolved turbulence, k_{est}, to be consistent with the modeled unresolved energy k_m. Quite simply, the model and resolved turbulence should be adjusted such that $k_{est}/k_m \to 1$. However, anisotropy in the filter separating the resolved and modeled scales complicates this requirement as now k_{est} is direction dependent. Further, though k_m is a scalar quantity representing the aggregate of the unresolved turbulence, the largest of the unresolved turbulent fluctuations will also depend on orientation due to the anisotropic filter and anisotropy in the turbulence itself. Therefore, it is beneficial to consider blending based on estimates of the turbulent fluctuations rather than solely the kinetic energy. Such information is contained in the Reynolds stress tensor, R_{ij}. Finally, to prevent attempted simulation of turbulence not supported in every orientation of the grid, defining the equilibrium between resolved and unresolved turbulent fluctuations requires consideration of the least resolved direction with respect to modeled turbulence.

To measure the the balance between the largest estimate of the unresolved turbulent fluctuations based on the state of the resolved turbulence and the modeled turbulence, we use the ratio r_k:

$$r_k = \frac{\lambda_{max}^{R^{est}}}{\lambda_{min}^{R^m}}, \tag{5.7}$$

where $\lambda_{max}^{R^{est}}$ is the largest eigenvalue of the subgrid stress as estimated based on the resolved field and $\lambda_{min}^{R^m}$ is the smallest eigenvalue of the model stress.

The objective of blending is to achieve $r_k = 1$. When this is achieved, the resolved and modeled turbulence are balanced with respect to the least resolved orientation in the field and the current level of RANS/LES blending should remain constant. Alternatively, when $r_k \neq 1$, the amount of blending must change to guide the resolved field to equilibrium with the model. In the interest of only resolving physically meaningful turbulence, the rate at which energy is returned to or removed from the resolved scales must be limited. This limiting is achieved by controlling the rate of change of α using the local turbulent timescale of the modeled turbulence, T_m. Specifically,

$$\frac{d\alpha}{dt} = \frac{1}{T_m}(r_k - 1), \tag{5.8}$$

Assuming the resolved and model turbulence are not far out of equilibrium, T_m is also the time scale associated with the smallest resolved eddies, making it an appropriate time scale for the exchange of energy between resolved and unresolved turbulence. A timescale could be derived from the resolved scales as $T = |\mathcal{M}|/|Q|^{1/2}$ however, in regions where the resolved gradients are very small, this measure becomes large potentially causing the hybridization to respond at too slow of a rate.

To ensure full RANS behavior in regions where $r_k > 1$, α is limited to be less than or equal to one. The lower limit for α can be determined by neglecting the transport terms of the k equation (3.9) and solving for α such that k cannot go to zero at a rate faster than T_m^{-1}. That is,

$$\partial_t k \approx \frac{0 - k}{T_m} \leq \alpha \mathcal{P}_k - \epsilon. \tag{5.9}$$

With $T_m = k/\epsilon$, this reduces to the simple requirement $\alpha \geq 0$. Ideally, under the conditions of $k_{est} > k_m$ while $k_{est} < k_{tot}$, r_k should be free to exceed one. Such conditions arise when some resolved turbulence is being convected through a coarsening grid. As we do not have a reliable estimate of the total turbulent kinetic energy, due to a general inability to differentiate resolved turbulent from unsteady kinetic energy, α is capped at one everyone in the present work.

To compute α, we must estimate the eigenvalues appearing in (5.7). Recall from §5.2 that the tensor Q provides a representation of the second-order structure function, with separations at the resolution scale. Given a form for the turbulent energy spectrum, the second order structure function at scale r (i.e., $F_2(r)$) can be related to the energy at scales smaller than r [104]. Assuming that r is in a Kolmogorov inertial range, the energy $k_<$ in scales smaller than r is just $k_< = C_F \overline{F}_2(r)$ where $C_F \approx 0.367$ from the Kolmogorov spectrum (see §B.3 for derivation). Thus, the maximum eigenvalue of the unresolved Reynolds stress tensor may be estimated using the resolved field as

$$\lambda_{max}^{R^{est}} \approx \tfrac{2}{3} C_F \lambda_{max}^{Q},$$

where λ_{max}^{Q} is the maximum eigenvalue of Q. That is, $\lambda_{max}^{R^{est}}$ is the largest isotropic estimate of R_{ij} given the aniostropic estimates of the unresolved kinetic energy stemming from the anisotropic resolved field and filter. The estimate

$$k_{ij}|_{\mathcal{M}} = C_F Q_{ij}, \tag{5.10}$$

is to be understood as representing the approximate unresolved turbulent kinetic energy corresponding to every direction of the anisotropic resolution. That is, in every orientation, we have a unique estimation. It is important to note the use of an isotropic homogeneous relation in Eq. B.7 with an anisotropic structure function approximation in Q_{ij}. While the resolution may be anisotropic and therefore the resolved turbulence also anisotropic, if the actual *total* turbulence is still isotropic in the range of $\mathcal{M}$, there have been no additional approximations implied beyond that of the existence of a Kolmogorov initial range. Where this is not true, the estimation in (5.10) becomes approximate with its validity based on the expectation that the modeled small scales are only weakly anisotropic; certainly more isotropic than the resolved scales. This approximation is consistent with the use of a k-ϵ model for the small scales.

Using standard k-based RANS models, $\lambda_{min}^{R^m}$ would simply be $\frac{2}{3}k_m$. However, the use of Durbin's $\overline{v^2}f$ model [36, 56] allows us to incorporate anisotropy in the Reynolds stress without introducing any ad hoc wall functions by taking

$$\lambda_{min}^{R^m} \approx \overline{v^2}.$$

The $\overline{v^2}$ based estimate of the smallest of the largest scale fluctuations of the modeled turbulence ($\overline{v^2} \approx \inf(\sup(R_{ij}))\ \forall u_i \in nullf(u_i))$ will be less than the basic $\frac{2}{3}k$ estimate in attached boundary layers and prevents inappropriate reduction of the modeled turbulence (*i.e.*, inappropriate reduction of α) in under-resolved boundary layers.

As previously commented, for (5.3.1) to be valid $\mathcal{M}$ must be everywhere in the inertial range. This is due to both its derivation assuming a Kolmogorov inertial range spectrum and the construction of Q using total gradients to approximate velocity differences. If the total gradient contains more than negligible mean gradient contributions, the approximation of fluctuating velocity differences is invalid. Where the length scale implied by $\mathcal{M}$ is larger than in the inertial range, the estimate of the unresolved energy will be greater than the total turbulent kinetic energy. While completely inaccurate, this is of no consequence since it will simply result in the selection of RANS mode, which is the correct outcome.

5.3.2 Hybrid Eddy Viscosity

Since we propose to use typical scalar eddy viscosity RANS models rather than full Reynolds stress models, the blending process has been reduced to scalar parameter α resulting in a scalar eddy viscosity based on the standard RANS form. However, given our knowledge of the anisotropy in the estimation of the unresolved average turbulent fluctuations through Q_{ij}[3], we can introduce directional dependence in the hybrid model eddy viscosity. The resulting subgrid stress model has the form of (5.2) but with a different viscosity tensor resulting from the blended transport model equations.

---

[3] Note that Q_{ij} provides no information about the anisotropy in SGS tensor, τ_{ij}^{sgs}, but does indicate the anisotropy in the *approximation* of τ_{ii}^{sgs} given the anisotropy of the filter, $\mathcal{M}$, and the resolved field.

The hybrid eddy viscosity ν_{ij} is formulated to have the same anisotropy as developed for pure LES in §5.2 when the resolution is sufficient—i.e., when $\mathcal{M}$ is in the inertial range. Alternatively, in full RANS mode, when $r_k > 1$, the hybrid eddy viscosity must of course be the usual eddy viscosity from the RANS model. To accomplish this, we introduce the following hybrid eddy viscosity:

$$\nu_{ij} = \nu_t a_{ij}, \tag{5.11}$$

where the anisotropy tensor a_{ij} is given by

$$a_{ij} = \delta_{ij}(1-\beta) + \left(\frac{3}{\tilde{Q}_{kk}}\right)\tilde{Q}_{ij}^{\frac{1}{2}}\beta, \tag{5.12}$$

and

$$\beta = \min\left(\frac{1}{r_k}, 1\right). \tag{5.13}$$

Equation 5.11 acts to redistribute the scalar hybrid eddy viscosity ν_t to be consistent with the estimated anisotropy in the unresolved field. When the model is consistent with or exceeds the estimate of the unresolved k in (5.10), $r_k \leq 1$ and $\beta = 1$; the anisotropy will then have the same form as that developed in §5.2. Alternatively, when operating as a RANS, $\beta \to 0$ with increasing r_k, so that a_{ij} becomes the identity tensor, and ν_{ij} is equivalent to the usual isotropic RANS eddy viscosity. The drawback of the blending in (5.12) and (5.13) is that in a_{ij} only asymptotically goes to δ_{ij} so that intermediate conditions which are still operating as a RANS but are near LES resolutions will also experience some anisotropy in ν_{ij}.

5.4 Resolution Inhomogeneity Correction

The estimates of unresolved energy and subsequent blending discussed in the previous sections respond only to the local state of the flow. That is, they are constructed only using the local gradients and grid size. They do not respond to changes in the grid size. Given a Lagrangian viewpoint where the resolved field and model must adjust to changing resolution proportional to the convective speed and the resolution gradients, these static grid estimations, may be insufficient. We now introduce corrections to account for flow through complex grids.

As discussed in §3.3.3, LES and hybrid methods can be corrupted by commutation errors in the presence of grid resolution inhomogeneities. In principle, this problem can be corrected by imposing a uniform filter across the domain. When the grid spacing is everywhere smaller than the filter size, grid resolution gradients will be prevented from corrupting the resolved turbulence. However, in realistic applications, this approach is generally impractical, since resolution requirements for the simulation of complex turbulent flows are typically heterogeneous. That is, imposing a uniform length scale field would result in failure to resolve flow structures of particular interest to one's study. Instead, we propose a model which transfers energy between resolved and unresolved scales as turbulence flows through resolution inhomogeneities.

5.4.1 Idealized formulation

The proposed model is based on the variable filter width analysis by Ghosal [57] (§3.3.3) with adaptation for the resolution definition in $\mathcal{M}$. A heterogenous filter applied to a gradient operator is approximated as

$$\overline{\frac{\partial \phi}{\partial x_j}} = \frac{\partial \overline{\phi}}{\partial x_j} - \frac{\alpha_{\mathcal{M}}}{2} \frac{\partial \mathcal{M}^2_{mn}}{\partial x_j} \frac{\partial^2 \overline{\phi}}{\partial x_m \partial x_n} + \mathcal{O}(\Delta^4), \tag{5.14}$$

where $\alpha_{\mathcal{M}}$ is a coefficient of order one related to the specific filter ($\alpha_{\mathcal{M}} = 1$ for spatial top hat filters). Let us define a heterogeneous filtered gradient operator as

$$\partial^{\mathcal{M}}_j(\cdot) = \{\partial_j + \mathbf{T}_j\}(\cdot), \tag{5.15}$$

where $\mathbf{T}_j = -\frac{1}{2}\alpha_{\mathcal{M}}\mathcal{M}^2_{mn,j}\partial_m\partial_n$ and higher order terms have been neglected. Such filtering errors will be present in every spatial derivative term in LES equations. However, molecular viscosity is only significant in the DNS limit where the effects of varying filter width vanish. Additionally, errors associated with the gradient of pressure may be neglected for incompressible LES as the pressure term only effectively enforces continuity. Correction of the convective term results in

$$\overline{\partial_j U_i U_j} = \overline{U}_j \partial_j \overline{U}_i + \partial_j \tau_{ij} + \mathbf{T}_j (\overline{U}_i \overline{U}_j) + \mathbf{T}_j \tau_{ij}, \tag{5.16}$$

where we also made the approximation that $\mathbf{T}_j \overline{U}_j$ is negligible. This term is related to the convection of errors in incompressibility due to variable filter widths. It is assumed negligible because this correction is presumed to be included in the pressure correction, ∇p, to enforce continuity. We will refer to $\mathbf{T}_j (\overline{U}_j \overline{U}_i)$ and $\mathbf{T}_j \tau_{ij}$ as the large scale and subfilter scale correction terms, respectively. Had we the entire velocity field containing all scales of motion, both terms would adjust the resolved and subfilter contribution to $\partial_j (\overline{U_i U_j})$ in response to the change in the filter size. However, as the subfilter scales have been discarded, the action of the subfilter correction can only be recovered through the SGS model. That is, we will apply the correction to the resolved field directly using the large scale term and indirectly through the corresponding change in modeled turbulent kinetic energy production to account for the response of the subfilter term. The LES equations will then see the subfilter correction term manifest only through changes in the SGS model. In this way, energy removed or added to the resolved scales is balanced with the modeled energy conserving overall turbulent energy.

For convenience of implementation, the large scale term may be rearranged as

$$\overline{U}_j \mathbf{T}_j \overline{U}_i = -\nu^*_{jk} \partial_j \partial_k \overline{U}_i, \tag{5.17}$$

where

$$\nu^*_{ij} = \tfrac{1}{2} \overline{U}_k \partial_k \mathcal{M}^2_{ij} \tag{5.18}$$

showing how the correction behaves like artificial diffusivity in the direction of alignment between the velocity and grid gradient. Naturally, the opposite, where convection is in the direction of refining resolution, also occurs. In such cases, the model would be anti-diffusive and attempt to backscatter energy from the modeled energy to the resolved scales. While implementation of the correction in the conservation of momentum follows directly from (5.17), the resulting production in the model equation takes the form

$$\mathcal{P}_c^* = -\tfrac{1}{2}\overline{U}_i\overline{U}_j\mathbf{T}_j\overline{U}_i \tag{5.19}$$

as opposed to including the additional ν_{ij}^* through (5.17) in the standard $\mathcal{P}_k$ definition. This is a result of using (5.14) where the divergence is taken only over the gradient of the velocity and not including the resolution gradient term ($\overline{U_j}\partial_j\mathcal{M}_{mn}^2\partial_m\partial_n\overline{U_i}$ and not $\partial_m(\overline{U_j}\partial_j\mathcal{M}_{mn}^2\partial_n\overline{U_i})$).

5.4.2 Limited formulation

As presented, the heterogeneous correction is generally unstable and may introduce behavior which contradicts hybridization. While partially a result of using a truncated Taylor series approximation in (5.14), instability is primarily due to incomplete knowledge of the turbulent field; that is, we rely on a model for the total unresolved field kinetic energy instead of actually knowing all the sub-filter scales of motions. Constraints must be imposed based on the available information. In particular, the model is to behave in a different manner when removing resolved energy as opposed to returning energy to the resolved scales. With this in mind, three factors are introduced to limit the action of the proposed term: rate of energy transfer ($\mathcal{C}_k$), resolution adequacy ($\mathcal{C}_r$), and non-negative values of modeled turbulence ($\mathcal{C}_\mathcal{P}$). Each parameter is discussed next.

To be consistent with the overall blending approach as discussed in §5.3, the rate of exchange between resolved and modeled kinetic energy is limited by the timescales of the resolved turbulence (in the diffusive limit) and the modeled turbulence (in the backscatter limit). Whereas in (5.8) we could control the timescale directly, here we control the magnitude of the convective velocity appearing in (5.18). The diffusive limit velocity should only be composed of the resolved turbulence ($\overline{U} - \langle U \rangle$). However, it is not clear how to generally remove contribution from the unsteady portion of U^4.

---

[4] Time averaging over any interval is not equivalent to ensemble averaging except for the case of a statistically

Without being able to do so, a good approximation of $(\overline{U} - \langle U \rangle)$ is not possible. Therefore, we fall back to using the model kinetic energy in both modes of operation ($\mathcal{P}_c^* \geq 0$ and $\mathcal{P}_c^* < 0$) and use the modifier

$$\mathcal{C}_k = \min\left(\frac{(2k_m)^{1/2}}{|\overline{U}|}, 1\right), \tag{5.20}$$

the argument being the same as the use of T_m in (5.8). When the resolved field is in near equilibrium with the model, the estimate of the largest of the unresolved velocity scales through k_m is approximately equal to the smallest of the resolved scales.

Unlike the hybridized RANS/SGS model which adjusts to each mode of operation as discussed in the previous section, (5.18) should only be activated in LES regions. Provided the grid is sufficient to resolve the mean flow, grid heterogeneity has no effect on a RANS simulation. In full RANS operation, activation of this term in the diffusive limit erroneously produces extra model kinetic energy. Implementation of (5.18) necessitates some indication of local RANS or LES operation. As previously discussed, it is not possible to separate the unsteady component of U from the resolved turbulent component and so using the ratio of resolved turbulence to modeled turbulence is not possible. However, an indication of full RANS operation is when $\alpha \approx 1$ and $r_k \gg 1$ and full LES operation when $\alpha \approx 1$ and $r_k \approx 1$ or $\alpha < 1$ and $r_k < 1$. Further, if the grid is capable of resolving additional turbulence (r_k<1), (5.18) should not be permitted to remove resolved energy. Similarly, if the grid is incapable of resolving additional turbulence (r_k>1), (5.18) should not be permitted to add resolved energy. A resolution modifier which combines the above requirements is

$$\mathcal{C}_r = \begin{cases} \alpha\left(\frac{\min(r_k,1)}{\max(r_k,1)}\right) & \text{if } \mathcal{P}_c^* \geq 0, \\ (1-\alpha)\left(\frac{1-\min(r_k,1)}{\max(r_k,1)}\right) & \text{if } \mathcal{P}_c^* < 0. \end{cases} \tag{5.21}$$

The behavior of $\mathcal{C}_r$ is qualitatively correct with diffusive operations active only in the vicinity of both α and r_k equal to one. The anti-diffusive limit activates only in the regions of both α and r_k

---

stationary flow. Attempting to use time average for unsteady flows results in an estimation of $u - u'$ which is corrupted with (and likely dominated by) the unsteady component.

less than one. A better method to determine full RANS operation is still necessary and remains a general issue with the entire new hybridization method. However, without this modifier, (5.18) may act in a contradictory fashion with respect to the overall hybridization.

Finally, we must prevent the modeled kinetic energy from becoming negative. While (5.20) prevents backscatter where there is no modeled turbulence, it may still allow negative k_m where the total production is negative. As discussed in §5.3 (5.9), the approximate condition for reduction in modeled k at a physical rate through blending is $\alpha \geq 0$. However, if using (5.23) as a backscatter mechanism to return modeled energy to the resolved scales, the additional condition that $\alpha\mathcal{P}_k + \mathcal{P}_c \geq 0$ must also be enforced. The most straight-forward way to satisfy this constraint is to use the modifier

$$\mathcal{C}_{\mathcal{P}} = \begin{cases} 1 & \text{if } \mathcal{P}_c^* \geq 0, \\ \frac{\max(\alpha\mathcal{P}_k + \mathcal{P}_c, 0)}{\alpha\mathcal{P}_k + \mathcal{P}_c} & \text{if } \mathcal{P}_c^* < 0, \end{cases} \tag{5.22}$$

The final heterogeneous correction term is then

$$\nu_{ij}^c = \mathcal{C}_r \mathcal{C}_k \mathcal{C}_{\mathcal{P}} \nu_{ij}^*, \tag{5.23}$$

with the corresponding modifications to $\mathcal{P}_c^*$.

It can be shown (§B.6) the large scale correction behaves like selective upwinding of the convective term, $\overline{U}_j \partial_j \overline{U}_i$, as weighted by the resolution gradient. As discussed in [15] and §A.2, upwinding in LES prevents the formation of resolved scales of motion near the cutoff length scale. While the effect of this term on the resolved scales are similar in some ways to the artificial viscosity added by upwinding the convection term in the momentum equation—i.e., spurious oscillations due to convection of resolved structures through a coarsening grid are removed—the construction here is formulated so that this removal of oscillations corresponds only to resolved turbulent scales of motion which become unsupported by the changing resolution, with their energy directly deposited into the aggregate modeled unresolved turbulent kinetic energy. By modifying the production in the model k equation (3.9) with (5.19), the exchange between resolved and modeled turbulence is energy conserving. This is not the case in upwinding where such energy is lost.

The model proposed here is a model of the correction in [57]. It is preliminary in nature and requires further evaluations and probable refinements. It does, however, appear to be the first heterogeneous resolution treatment for rapid convection LES flows with non-trivial grids.

Chapter 6

Model Demonstration

This chapter will demonstrate the individual components of the new method presented in Chapter 5. The form of SGS anisotropy is demonstrated quantitatively using isotropic homogeneous turbulence with anisotropic filtering. The behavior of the hybrid blending and grid inhomogeneity corrections are first qualitatively shown separately. All hybrid simulations use a heavily modified version of Stanford's Center for Turbulence Research incompressible CFD code CDP v2.4 (§A.1)[1]. Finally, the complete framework is demonstrated using the case of high Reynolds number post drag-crisis cylinder in crossflow in comparison with experimental measurements and simulations using RANS alone.

6.1 Anisotropic SGS

To evaluate the efficacy of the proposed anisotropic SGS model, simulations of forced isotropic turbulence at $Re_T \approx 5000$ in a $(2\pi \times 2\pi \times 2\pi)$ periodic domain are performed. LES using the proposed SGS model and the standard Smagorinsky model are performed on an anisotropic grid $(128 \times 32 \times 32$ and $128 \times 128 \times 16)$ with comparison to equivalently filtered DNS on a $256 \times 256 \times 256$

---

[1] Basic verification results shown in §A.4

grid.

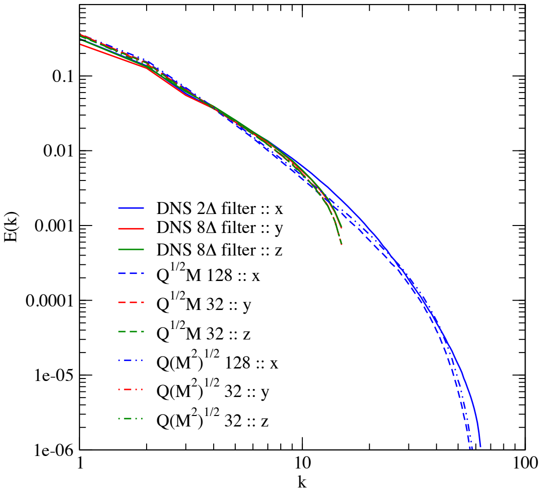

Figure 6.1: One dimensional energy spectrum of filtered DNS($N = 256^3$) *and both proposed SF-SGS model forms of anisotropy, "*$Q^{1/2}M$*" using (5.3) and "*$Q(M^2)^{1/2}$*" using (5.4) with* $N = 128x32x32$ *in a periodic* 2π *box. All spectra averaged of five eddy turnover times.*

As seen in Figure 6.1, the form of the anisotropy model makes only a slight difference for orthogonal grids. The $\tilde{Q}^{1/2}$ (5.3) based form slightly outperforms the $Q^{1/2}\mathcal{M}$ (5.4) form when considering the more resolved direction (blue lines) across the entire spectrum. However, both forms vastly outperform the standard Smagorinsky model (Figures 6.2 and 6.3, only $\tilde{Q}^{1/2}$ shown for clarity). In Figure 6.2 we examine the case of one refined direction with two coarse directions. While there is little difference in the coarse directions, the refined direction is increasingly corrupted with higher wavenumbers for the Smagorinsky model while the new model behaves quite well and only begins to resolve less turbulent content than filtered DNS just before the cutoff wavenumber. Similar grid anisotropy effects are observed in in Figure 6.3 for the case of two refined directions and one coarse direction. However, the new model yields slightly excessive energy in comparison with filtered DNS over wave numbers ranging from ≈ 10 to 50. Additionally, both models experience increased energy

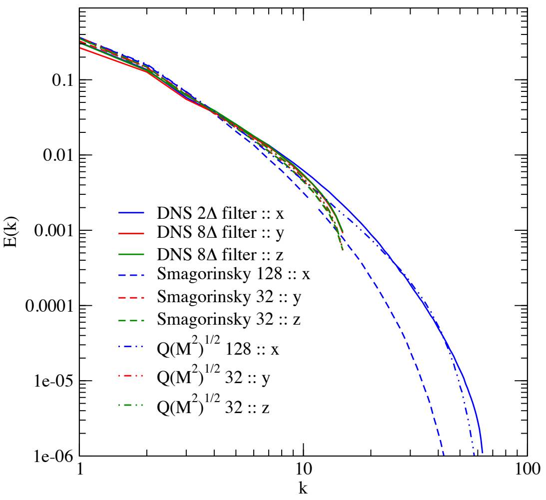

Figure 6.2: One dimensional energy spectrum of filtered DNS($N = 256^3$), proposed SF-SGS model (5.4), and standard Smagorinsky ($C = 0.18$) with $N = 128$x32x32 in a periodic 2π box. All spectra averaged of five eddy turnover times.

in the coarse direction with the Smagorinksy model being the more erroneous of the two.

It is the goal of an LES to simulate statistically accurate turbulence over all scales of resolved motion. In the presence of anisotropic grids, an isotropic SGS model cannot achieve this and effectively wastes the added computational costs associated with the more refined orientation. With the anisotropy presented in (5.4), statistically relevant turbulence is recovered in all orientations of the grid. While the filter/grid aspect ratios are mild (1:4:4 and 1:1:8) in comparison to grids seen in complex geometries they serve to demonstrate both the deficiencies in a scalar measure of grid spacing for anisotropic grids and the significant improvements in the model presented here. However, more validation tests are needed to fully characterize the performance of the anisotropic model.

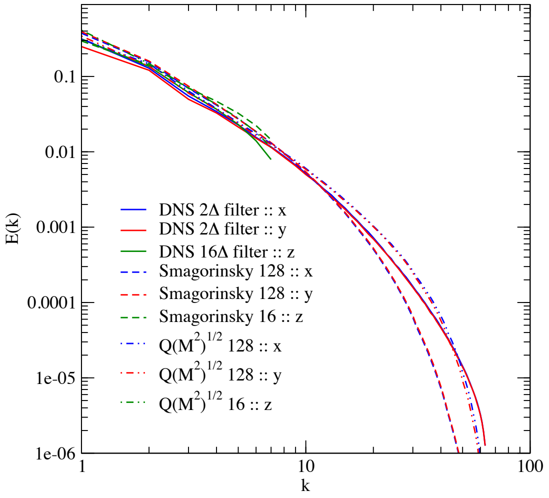

Figure 6.3: One dimensional energy spectrum of filtered DNS($N = 256^3$), proposed SF-SGS model (5.4), and standard Smagorinsky ($C = 0.18$) with $N = 128$x128x16 in a periodic 2π box. All spectra averaged of five eddy turnover times.

6.2 Hybrid RANS/LES Blending

To demonstrate the behavior of the hybridization, we examine the case of a post drag crisis cylinder in cross flow at $Re_D = 4$x10^5. The domain is a truncated version of the wind tunnel experiments of Schewe [1] with dimensions ($10D \times 11D \times 0.1D$) having the cylinder centered at 5D downstream of the inlet (Fig 6.4). A uniform velocity is used at the inlet, slip conditions imposed on the top and bottom wind tunnel "walls"[2], periodic conditions in the span, and convective outflow boundary conditions at the exit. Grid details are as follows: initial wall normal spacing: 5x10^{-5}D, initial aft wall tangent spacing: 1x10^{-3}D, initial for wall tangent spacing: 2.5x10^{-2}D, spanwise spacing: 0.01D, and farfield maximum spacing: 0.5D. Wall normal spacing is selected so that the first cell at the top and bottom of the cylinder is positioned at $y^+ \approx 1$ at the operating Reynolds number.

---

[2] This is justified by the boundary layer being very thin along with wind tunnel walls so that rather than resolving the boundary layer, slip conditions may be imposed at the approximate location of the momentum displacement thickness.

The mesh is constructed with an expansion region just aft of the cylinder for 0.5D followed by a "focus" region extending for 1.0D containing a uniform in-plane mesh of 3x10^{-3}D (Fig. 6.5). After this focus region, the mesh rapidly expands to the outlet.

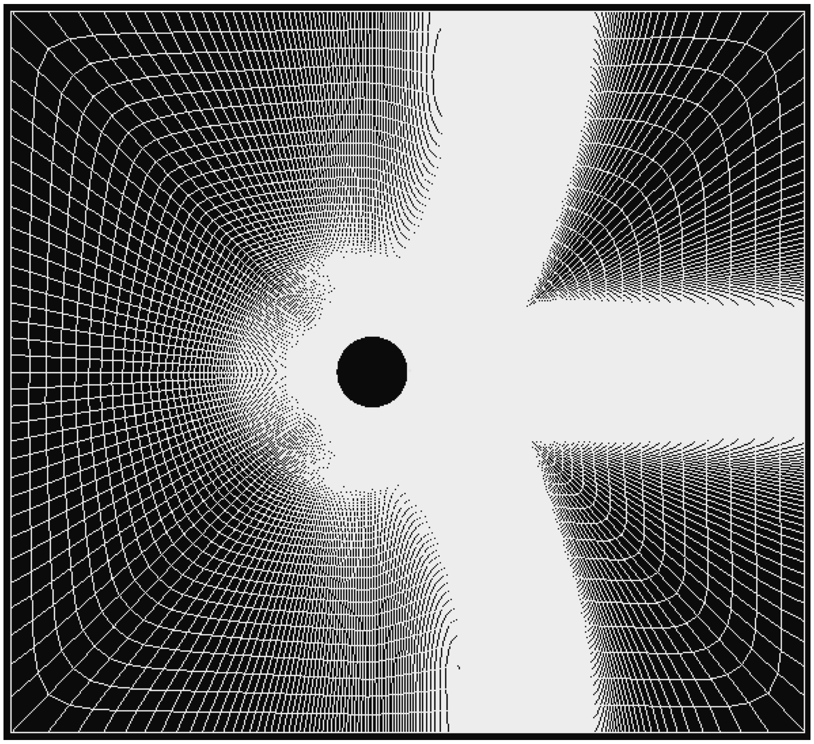

Figure 6.4: Domain and mesh of the cylinder in crossflow.

Simulation are run under conditions of full $\overline{v^2}f$ RANS and the hybrid model as presented in the previous chapter for over $100t_{conv}$. Snapshots comparing typical spanwise vorticity, resolution adequacy parameter, r_k (5.7)), and modeled turbulent kinetic energy are shown in Fig. 6.6.

Figure 6.6 demonstrates the overall concept of the proposed hybrid framework. Dictated by the the resolution adequacy indicator (Fig. 6.6c), modeled energy (Fig. 6.6e) is returned to the resolved

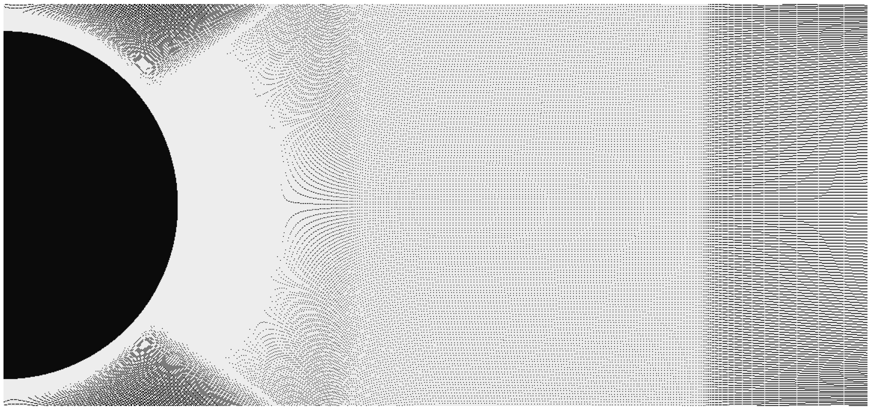

Figure 6.5: Focus region of domain in Fig. 6.4 showing the the expansion region just aft of the cylinder for 0.5D followed by the focus region of uniform resolution $3\text{x}10^{-3}D$ *followed by the beginning of the rapid expansion region.*

scales (Fig. 6.6a) resulting in increased simulated turbulence (Fig. 6.6b) and reduced modeled turbulence (Fig. 6.6f). Even in the weakly 3D domain used here (that is, unsteady wake structures such as ribs and rollers are prevented from forming), drastically different results are evident between RANS and hybrid simulations as seen by the amount of resolved versus modeled turbulence (Fig. (6.6) a/e compared to b/f). Everywhere the resolution adequacy parameter, r_k, is less than unity in the RANS simulation (Fig. 6.6c) is indicative of the grid being capable of resolving additional turbulence. With the hybridization activated, the blending parameter responds to $r_k < 1$ and guides the model and resolved field so that $r_k \to 1$ in the cylinder wake resulting in significantly more resolved turbulence in place of modeled turbulence. It is important to note that r_k does not necessary equal unity in the hybrid simulation. This is because $r_k = 1$ is merely the target value for the blending; as the dynamically evolving turbulence convects through the wake, blending adjusts accordingly and continually attempting to maximize the amount of resolved turbulence to be consistent with the theoretical estimate of unresolved turbulence kinetic energy.

Partial resolution of turbulence with reduced SGS is, of course, the entire point of an LES. How-

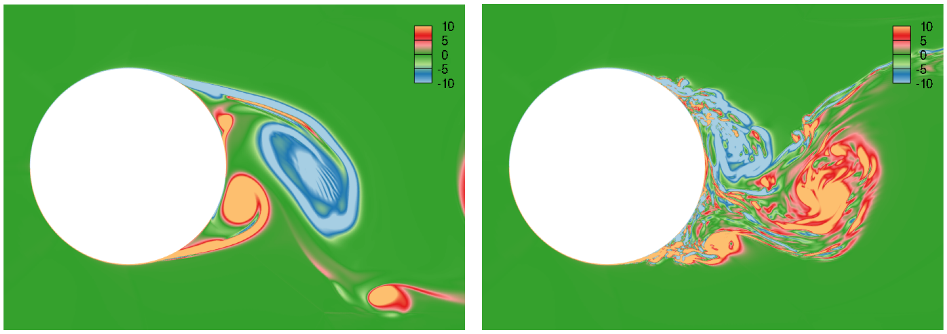

(a) Spanwise vorticity RANS (b) Spanwise vorticity HYBRID

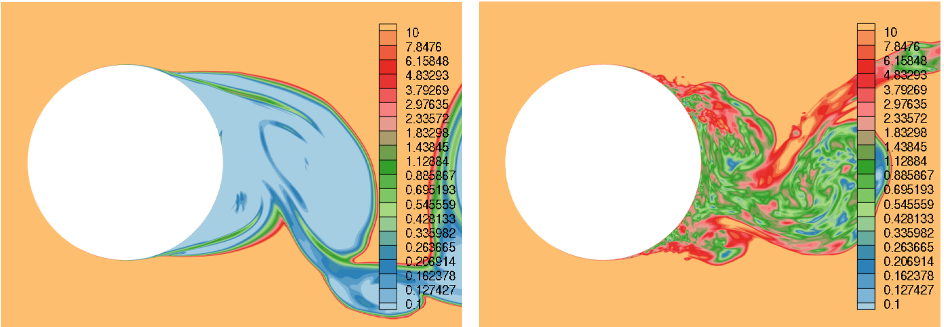

(c) r_k RANS (d) r_k HYBRID

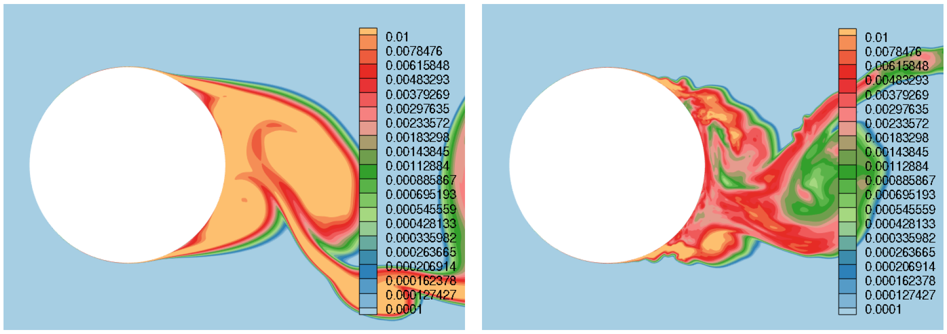

(e) k_m RANS (f) k_m HYBRID

Figure 6.6: Comparison of spanwise vorticity (a,b), resolution adequacy parameter r_k *(c,d), and modeled turbulent kinetic energy (e,f) of a cylinder in crossflow at* $Re_D = 4\text{x}10^5$ *using basic* $\overline{v^2}f$ *RANS (a,c,e) and the hybrid blending presented in §5.3 (b,d,f).*

ever, what is significant is that the hybridized model is able to transition between RANS and LES without user intervention or special considerations for the attached boundary layer and the separation location. Notice the separation point of the fully turbulent boundary layer is at approximately the same location in both simulations. The upstream boundary layer remains primarily RANS (except in the outer regions near the separation point) in the hybrid simulation. While only one case, this is a strong indication of the ability of the new approach to simulate smooth-wall separation.

6.3 Resolution Inhomogeneity

In an effort to clearly demonstrate the action of the diffusivity-based inhomogeneity correction term, a 2D unsteady RANS simulation is used with $\mathcal{C}_r = 1$ (5.21) and $\mathcal{C}_k = 1$ (5.20). This is not how the term will be used in the remainder of this work but serves to emphasize its effects. A post drag-crisis 2D cylinder in cross flow ($Re_D = 3.5 \times 10^5$) is selected for this purpose. The domain is a simple spanwise-periodic O-mesh of radius $10D$ with initial wall tangent spacing $1 \times 10^{-2}D$ and wall normal spacing of $5 \times 10^{-5}D$ grown at a rate of 5% to a maximum of 0.8D. The convective term in momentum is discretized using a central difference scheme (CDS). For this Reynolds number, a 2D simulation is absolutely incorrect; again, this case is purely for demonstrative purposes.

Figure 6.7 shows the mesh (6.7(a)), spanwise vorticity (6.7(b) and 6.7(d)), and model kinetic energy (**??**), both as computed from simulations with and without the inhomogeneity treatment. Clearly, without any correction, when using an energy conserving CDS, even this mild mesh resolution gradient leads to drastic dispersion errors which entirely destroy all coherent flow structures in the wake. The addition of (5.17) prevents the spurious oscillations, allowing the vorticies shed from the cylinder to retain their structure as they move through the coarsening grid while transferring the energy of the unsupported flow structures to the turbulent model. Of course, as we have set $\mathcal{C}_r = 1$ for this demonstration, much of the energy transferred to the model may be due to unsteadiness and not resolved turbulence.

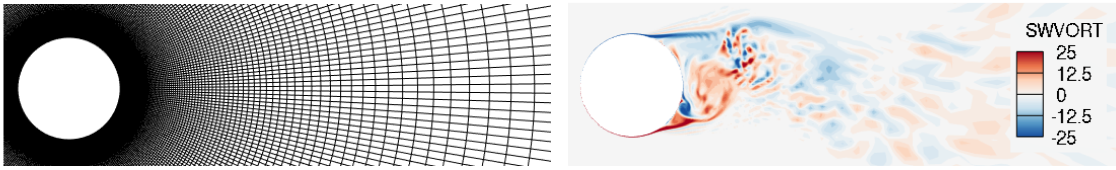

(a) Cylinder mesh with resolution inhomogeneity.

(b) Spanwise vorticity (without correction).

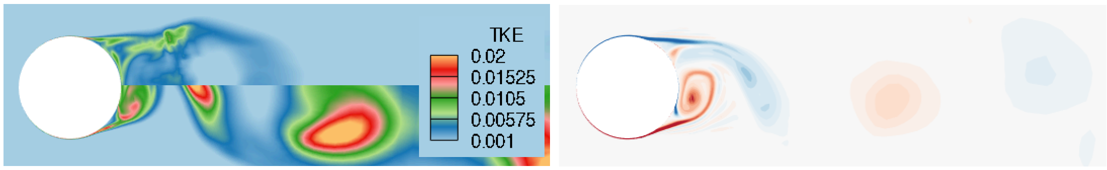

(c) Model kinetic energy (top: without correction, bottom: with correction).

(d) Spanwise vorticity (with correction).

Figure 6.7: Effects of correction for resolution inhomogeneities on an unsteady RANS of a 2D cylinder at $Re_D = 3.5 \times 10^6$.

6.4 Integrated Framework

We now quantitatively compare the results of the hybrid and RANS simulations discussed in §6.2 and the second portion of §6.3 to the experimental results of Schewe [1] for three post drag-crisis Reynolds numbers, $Re_D = (4, 6, 10) \times 10^5$. While a three cases are completely insufficient for validation purposes, it does begin to reveal the improvements attainable with the new hybrid method. Mean drag coefficient and Strouhal numbers are shown in Table 6.1.

Re_D	4×10^5		6×10^5		1×10^6	
	C_D	St	C_D	St	C_D	St
Experiment [1]	0.224	0.476	0.221	0.473	0.253	0.456
$\overline{v^2} f$ RANS	0.873	0.289	0.835	0.289	0.849	0.312
Hybrid	0.690	0.332	0.546	0.359	0.447	0.366

Table 6.1: Simulation statistics for a cylinder in cross flow at $Re_D = (4, 6, 10) \times 10^5$ *taken over* $50 t_{conv}$ *for a basic* $\overline{v^2} f$ *RANS simulation, hybrid simulation, and experiments of [1]*

Direct comparison of the mean drag coefficient and Strouhal number shows poor agreement for both

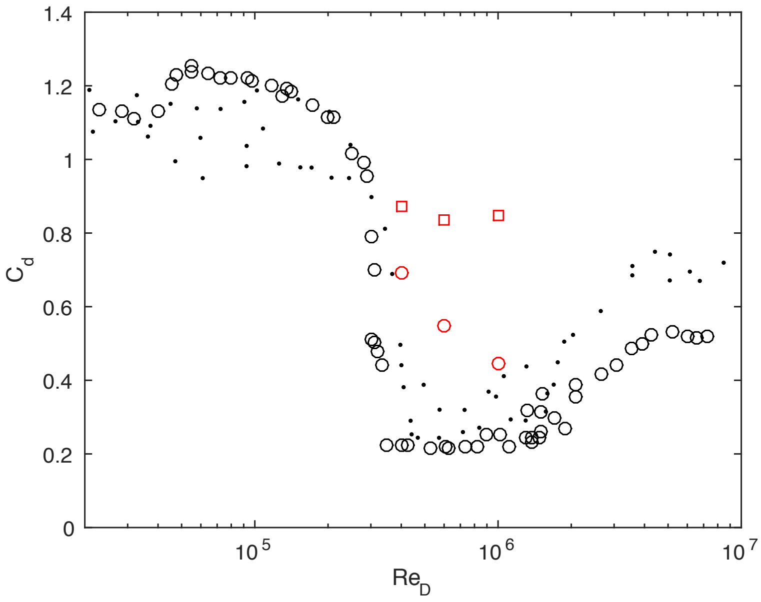

Figure 6.8: Comparison of drag coefficient simulation results for a cylinder in cross flow at $Re_D = 4 \times 10^5$ *using* $\overline{v^2}f$ *RANS (□) and the new hybrid framework (○) with experimental data (○) of Schewe [1] and (·) of [4–8] as accumulated by and reproduced from [9].*

the RANS and hybrid simulations. However, for both measures, the hybrid method yields results closer to experimental data than RANS alone. Further, plotting these results with data (Figs. 6.8 and 6.9) at other Reynolds numbers reveals the sharp drag-crisis transition to a fully turbulent boundary layer has become more gradual for the hybrid simulations (and possibly not at all for the RANS simulations). For both C_D and St, it appears the hybrid simulation is approaching the experimental value as Re_D moves further past the drag-crisis. This is likely either due to there being no inclusion of background turbulence in the simulations (the wind tunnel used in [1] is reported to contain up to 0.4% free stream turbulence intensity) or there being some flow feature critical to the rapid transition which is not resolvable by the mesh. Alternatively, the shallow simulation span of 0.1D may be inadequate to resolve larger-scale spanwise instabilities necessary for the rapid drop off in drag at $Re_D \approx 3 \times 10^5$. A resolution and spanwise domain convergence study is necessary

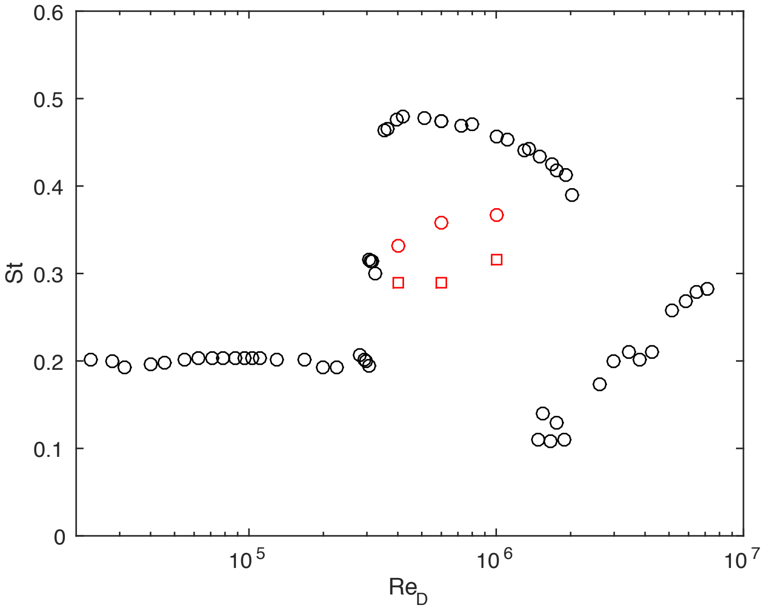

Figure 6.9: Comparison of Strouhal number simulation results for a cylinder in cross flow at $Re_D = 4 \times 10^5$ *using* $\overline{v^2}f$ *RANS (*□*) and the new hybrid framework (*○*) with experimental data (*○*) of Schewe [1].*

to determine if convergence to experimental values is possible with $\overline{v^2}f$ based hybrid simulations. Comparison of the hybrid C_D with the experimental data of [4–8] as accumulated by [9] (Fig. 6.8) show somewhat better agreement. However, additional Re_D cases should be performed to confirm the assertions of delayed and prolonged drag crisis and to evaluate claims of improvements of the new hybrid method over RANS alone.

Chapter 7

Stall Control Simulations

Simulations of a stalled NACA 4415 airfoil (20° AoA, $Re = 5.7 \times 10^5$) are performed with a heavily modified version of Stanford's CDP v2.4 finite volume incompressible Navier–Stokes solver [105] (§A1) with the aims of both demonstrating the proposed method's ability to accurately predict smooth wall separation while resolving turbulent content and to investigate the physical process responsible for pulse-actuated dynamic stall control. The simulation conditions are similar to experiments performed at Georgia Tech, allowing comparison to PIV data [10]. The simulation domain is $7 \times 2 \times 0.05$ (Fig. 7.1) (all lengths normalized by the chord) with uniform inflow, convective outflow, periodic boundary conditions in the spanwise direction, and slip boundary conditions at the top and bottom approximating the boundary layer momentum displacement thickness. The leading edge of the airfoil is 2 chord lengths downstream of the domain entrance. Located at 0.15c, the actuator is 4.2×10^{-2} [34].

Grid details are as follows; initial wall normal spacing: 2×10^{-5}, suction side wall tangent spacing: 2×10^{-3}, pressure side wall tangent spacing: 1×10^{-2}, stagnation point wall tangent spacing: 1×10^{-3}, trailing edge wall tangent spacing: 2×10^{-4}. The grid is grown from the airfoil surface at a rate of 10% per wall-normal cell step to a maximum of 2.0×10^{-3} in a region of $\approx 0.25c$ from the airfoil surface on the suction side. This has the effect of creating a focus region similar to that

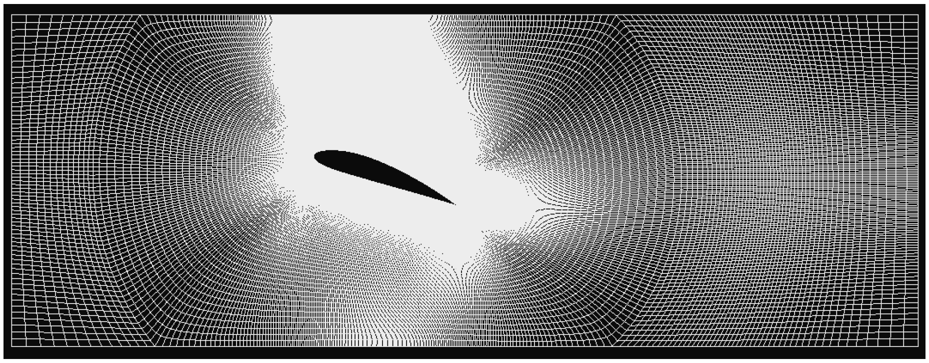

Figure 7.1: Approximated wind tunnel domain mesh for NACA 4415 airfoil at 20° *AoA.*

of §6.2 encompassing the attached boundary layer, separation point, shear layer, separation bubble, and near trailing-edge wake (Fig. 7.2). Outside of this region the mesh rapidly coarsens. The span is divided into only 10 cells. Thus, the mesh has extremely high aspect ratio cells near the actuator. Wall normal spacing is selected so that the first cell at the actuator is positioned at $y^+ \approx 1$ for the operating Reynolds number. The actuator is divided into 10 cells with edge-of-actuator spacing of 4×10^{-5}.

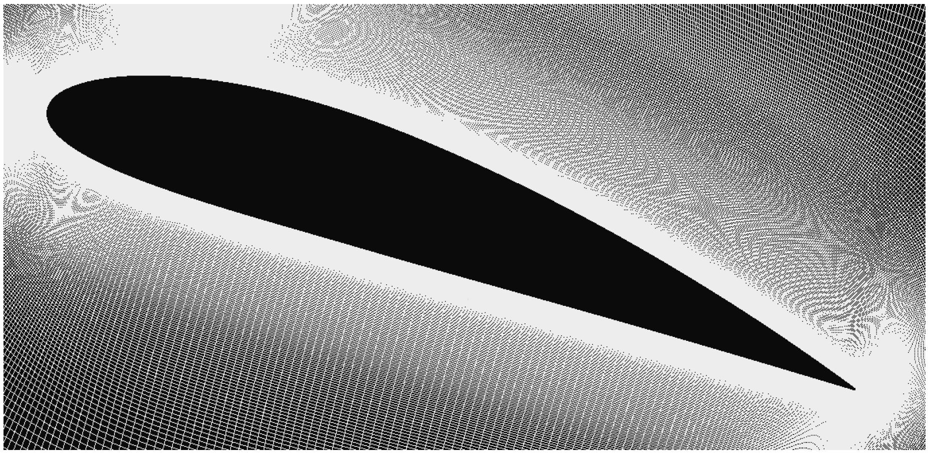

Figure 7.2: NACA 4415 airfoil mesh at 20° *AoA.*

Two hybrid cases are considered: the first with $\mathcal{M}$ everywhere determined directly from the grid and the second with a minimum spanwise-normal plane length scale of 2.5×10^{-3}c imposed on $\mathcal{M}$ to create a uniform resolution region.

7.1 Baseline Stall

Simulations are initialized from a uniform velocity field and allowed to come to a quasi steady state over approximately $20t_{conv}$ as a URANS simulation followed by activation of the hybrid method with superposition of random noise of maximum intensity of $0.01U_\infty$ to accelerate the development of turbulence. Hybrid simulations reach a quasi steady state after approximately $10t_{conv}$. Mean body forces of simulations are compared with experimental data in Table 7.1. While neither RANS nor the new hybrid method predicts C_L or C_D firmly within the range of experimental GaTech data, the hybrid C_L is very close to the upper-limit of the reported data as in [14]. The discrepancy is most likely attributable to the very shallow span used in the simulations which does not support significant spanwise modes of instability. Additionally, a reduction in mean lift may result from continued mesh refinement as there is a clear decrease in the transient local minima associated with the hybrid simulation in comparison with full RANS while the peak lift is largely unchanged (Fig. 7.3). In addition to the reduction in lift, the hybridization results in an elongation of the period of trailing edge vortex rollup and shedding as indicated by the reduced Strouhal number and oscillation period in C_L.

Case	C_L	C_D	St
GaTech [2, 10, 13, 14]	1.16-1.7	0.16-0.21	not provided
$\overline{v^2}f$ RANS	1.83	0.276	1.03
Hybrid	1.73	0.278	0.762

Table 7.1: Mean body forces and Strouhal number of a NACA 4415 at 20^o *and* $Re = 5.7 \times 10^5$ *using the developed new hybrid method,* $\overline{v^2}f$ *RANS, and GaTech experiments.*

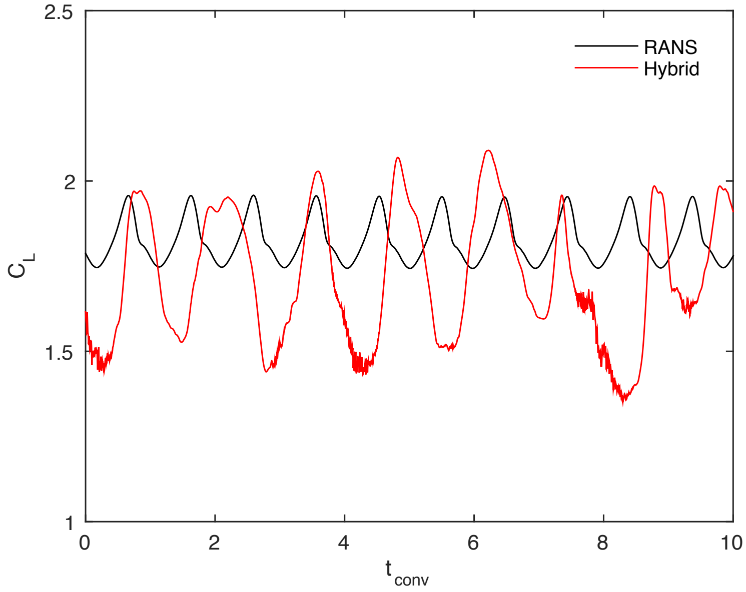

Figure 7.3: Transient lift coefficient of a simulated NACA 4415 at 20^o *and* $Re = 5.7 \times 10^5$ *using full* $\overline{v^2}f$ *RANS (-) and the developed new hybrid method (-).*

Figure 7.4 shows instantaneous images of the spanwise vorticity and corresponding modeled turbulent kinetic energy for the transient C_L curves shown in Fig. 7.3 and with an imposed resolution minimum at nearly the same point of their vortex shedding period. A prominent increase in resolved turbulence and unsteady flow structures, at the expense of modeled turbulence, is seen with each level of increased resolution. For the case of a resolution floor (7.4c & d), the imposed minimum length scale is on the order of the boundary layer thickness at the separation point causing the entire attached boundary layer upstream of separation to operate as a RANS. Significant modeled stress upstream of separation and stabilization of the detached shear layer results from modeling of the attached boundary layer. With the resolution dictated directly by the grid resolution (including the highly refined actuator resolution and transition), the turbulence in the outer boundary layer upstream of the separation point is actually partially resolved (7.4e & f). Though the first ∼10s of

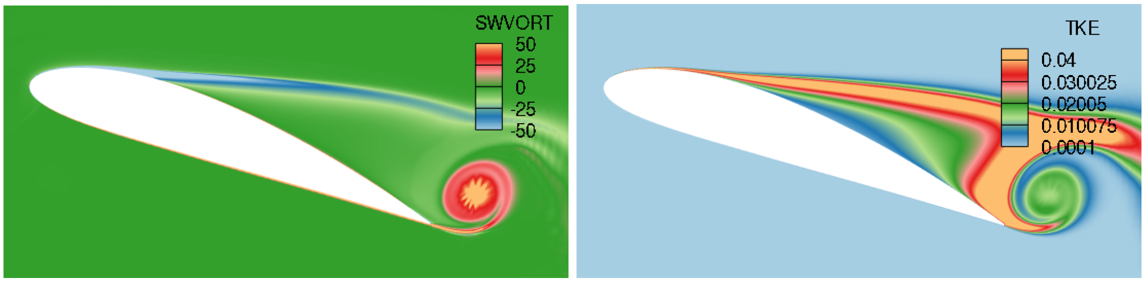

(a) Spanwise vorticity RANS (b) k_m RANS

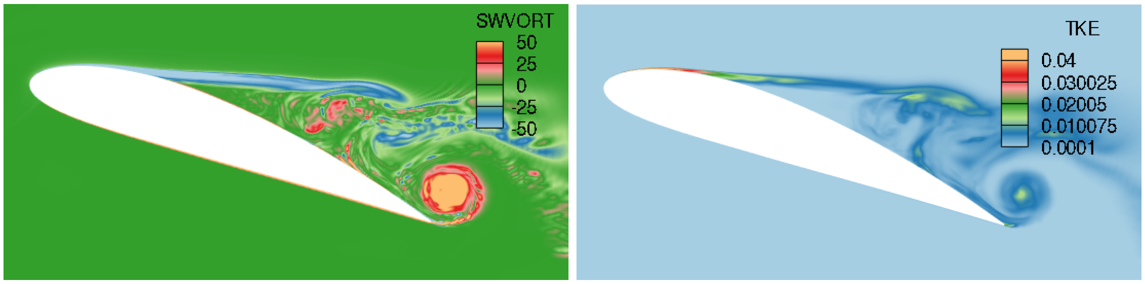

(c) Spanwise vorticity hybrid with $\mathcal{M}$ floor (d) k_m hybrid with $\mathcal{M}$ floor

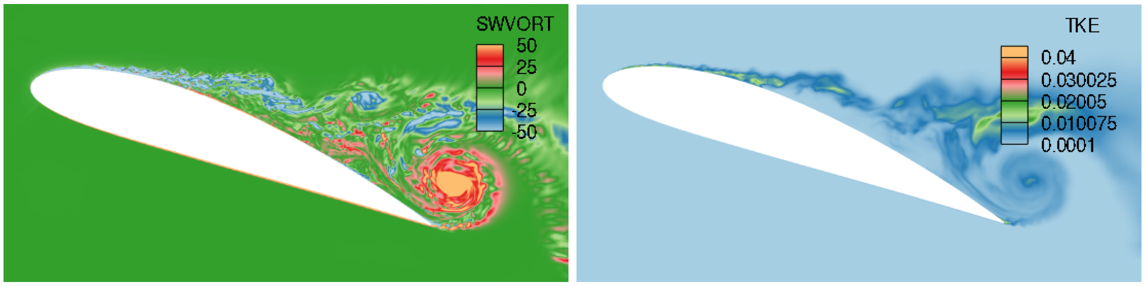

(e) Spanwise vorticity hybrid (f) k_m hybrid

Figure 7.4: Normalized spanwise vorticity (a,c,e) and corresponding modeled turbulent kinetic energy (b,d,f) of NACA 4415 at 20^o *and* $Re = 5.7 \times 10^5$ *for* $\overline{v^2}$*-*f *RANS (a,b), new hybrid method with a minimum resolution of* $2.5 \times 10^{-3}c$ *imposed on* $\mathcal{M}$ *(c,d), and new hybrid method with* $\mathcal{M}$ *determined directly form the grid (e,f).*

cells in the attached boundary layer remain entirely in a RANS regime, the turbulence is increasingly well resolved with distance from the wall. The result is turbulent undulations upstream of separation and a destabilized detached shear layer with resolved turbulent structures.

Perhaps the most significant point to be made from Fig. 7.4 is that the dynamic separation location remains virtually unchanged despite greatly different levels of turbulence resolution and modeling. The new hybrid modeling approach achieves this without *any* modifications to the model itself. That is, even though there is a difference of one to two orders-of-magnitude in the filter size leading to and in the vicinity of the separation region, the hybridization is still able to govern RANS to LES transition for both cases and yield the same general flow behavior. This is in stark contrast to the necessity for a length scale field floor in the presence of the actuator resolution to prevent GIS in previous DDES results (§4.2) and is an indication of the success of hybridization driven by a theoretical estimate of unresolved turbulence which considers both the state of the resolved field and the filter size.

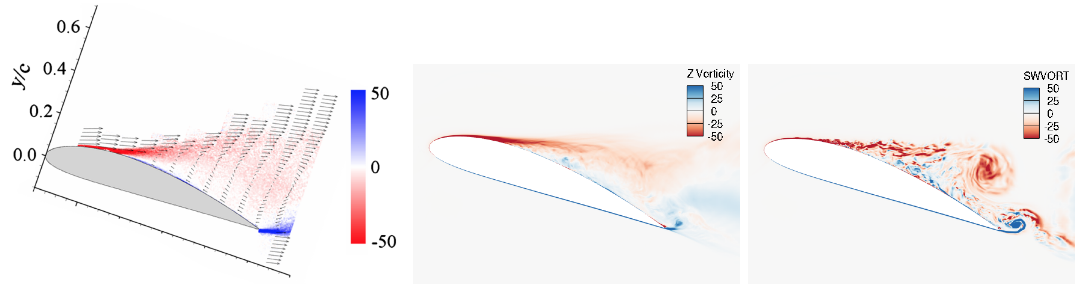

(a) Time averaged PIV (b) Time average hybrid (c) Instantaneous hybrid

Figure 7.5: Normalized spanwise vorticity of NACA 4415 at 20^o *and* $Re = 5.7 \times 10^5$ *of: (a) PIV [10], (b) time averaged new hybrid method, and (c) instantaneous new hybrid method. Average of (b) calculated as in §B.7 with* $t_{ave} = 0.5t_{conv}$.

The accuracy of the simulated dynamic smooth wall separation may be qualitatively evaluated by comparison of the separation point and the time-averaged separation region with experimental PIV images (Fig. 7.5). Simulations with the proposed hybrid model are in general agreement with experiments. Though fluctuating, the separation location is at approximately $0.3c$ in both the simulation and experiment. Further, the same general behavior, as seen by the average "spread" and intensity of spanwise vorticity, of the turbulent shear layer is observed. The spread of the shear layer is slightly more restricted in the simulation. This is again likely due to the shallow simulated span preventing spanwise instabilities and undulations from forming. However, the predicted mean is still an improvement over full RANS simulations (Fig. 7.4a). Thus, we may state that the simulations reveal detailed flow information in the separation region (Fig. 7.5c) not captured in PIV images (Fig. 7.5a) while still maintained accurate mean flow (Fig. 7.5b). It is quite remarkable that even with the coarse spanwise resolution ($5 \times 10^{-3}c$) in comparison to finest spanwise-normal plane resolution ($\mathcal{O}10^{-5}$) turbulent flow feature are capable of being resolved in spanwise-normal planes while maintaining overall accuracy. This is a strong indication of the validity of both the RANS/LES blending approach and the form of the eddy viscosity anisotropy.

7.2 Pulsed Actuation

The combustion pulse of [33] is simplified as incompressible and uniform plug flow of $U_{act} = 13.3U_\infty$ through the actuator over $0.05t_{conv}$ to match the total expulsion of the combustion chamber gas ($1cm^3$ or $1.05 \times 10^{-5}c^3$) over a duration from half-peak to half-peak of the combustion chamber pressure transient[1]. The boundary condition for the turbulent kinetic energy is heuristically selected to be $k_{act} = 80k_\infty$ (or $k_{act} \approx \frac{1}{4}U_{act}^2$) with $\overline{v^2}$ following as $\frac{2}{3}k_{act}$ and zero gradient for ϵ and f. As we are completely ignoring compressibility effects and have no real idea of the turbulent intensity in the combustion pulse, this value is set to create a coherent initial pulse vortex after actuation when using the resolution minimum of 2.5×10^{-3}c (Fig. 7.6b). This k_{act} does not result in a coherent initial actuation structure with $\mathcal{M}$ set directly from the grid (Fig. 7.6a); attempts at at raising k_{act} to achieve this resulted in simulation instability of ϵ. Additionally, k_{act} of 10 and 100 were also attempted but did not result in effective actuation highlighting how sensitive the reattachment process is to the structure of the initial pulse-induced vortex.

---

[1] It is likely that this pressure transient is affected by the measuring device risetime and may be much shorter in actuality.

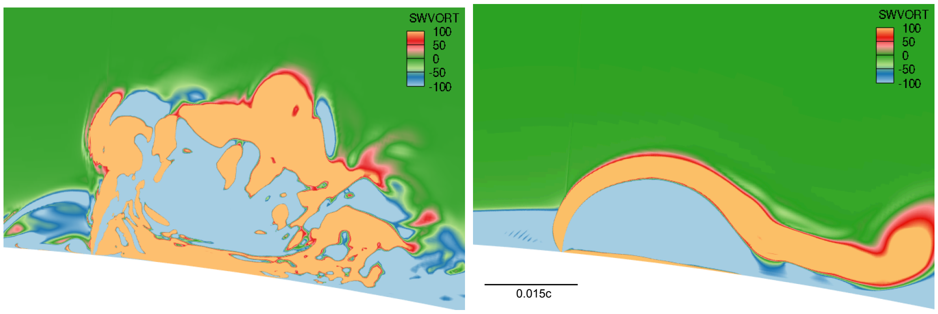

(a) Model resolution directly from grid (b) Minimum model resolution of 2.5×10^{-3}c

Figure 7.6: Normalized spanwise vorticity after application of a single pulse using the new hybrid method.

Without the imposed minimum resolution length scale, the initial pulse-induced structure shows a clear lack of coherency causing the actuation to be ineffective. The reason for this failure is likely due to a combination of: (i) the limitations placed on the inhomogeneity correction term (§5.4.2) being too severe and (ii) the fact that we are attempting to resolve turbulence much smaller than the initial actuation vortex structure. The former may be causing the amplification of errors as the high speed jet pulse convects through the coarsening near-actuator grid. The latter may result in the crude modeling simplifications of the complex combustion pulse becoming catastrophic to the fidelity of the pulse simulation. That is, the representation of the combustion pulse using a high k_{act} with a uniform flow boundary condition essentially breaks the proposed hybrid framework. The failure process can be summarized as follows.

The blending parameter is rapidly reduced due to the large local reduction in T_m as ϵ responds to the high k_{act} near the actuator orifice (5.8). The simulation attempts to return modeled k_{act} to the resolved scales but with only uniform flow at the actuator, there are no meaningful turbulent gradients to enhance and redistribute. Instead, the very sharp mean shear interface between the jet and the boundary layer are maintained causing the interface to break-up as the jet moves away from the actuator orifice. Negatively signed vorticity is not able to roll-up and form a distinct vortex resulting is the incoherent pulse structure seen in Fig. 7.6a.

No matter the cause, it is important to realize this is not the same mode of failure as seen by application of DDES to 3D pulsed stall control (§4.2). Using DDES, the initial pulse-induced structure was nearly identical to the 2D case. The pulse then broke-up rapidly indicating a failure of the hybrid method to sufficiently balance modeled and resolved turbulent stress. Using the new hybrid method, the initial pulse-induced structure never forms, indicating a failure in the representation of the combustion pulse itself as discussed above. Simulation of the reattachment process without the aid of a uniform resolution field remains an active goal. For the remainder of this section, we will focus on the results with the imposed minimum.

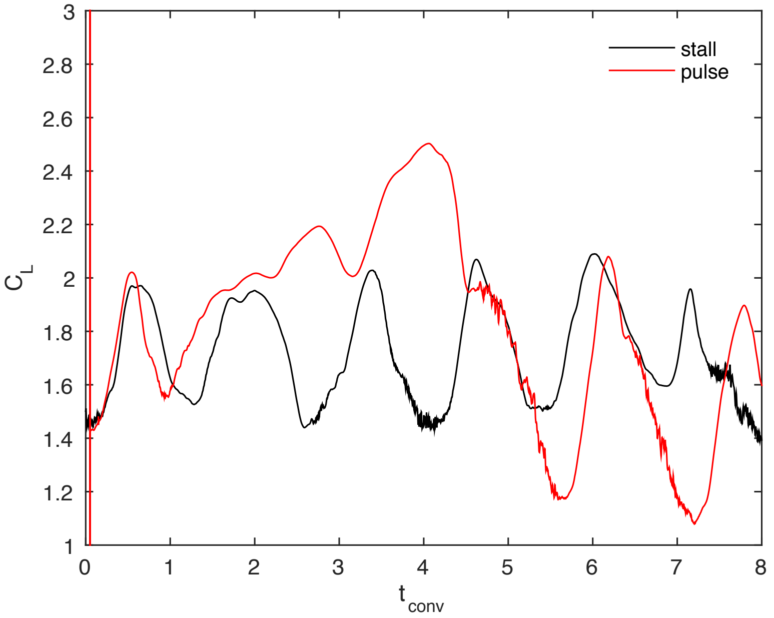

Figure 7.7: Transient lift coefficient of a simulated NACA 4415 at 20^o *and* $Re = 5.7 \times 10^5$ *of the baseline stall case using the new hybrid method (-) and with application of single pulse using a minimum resolution length scale of* $2.5 \times 10^{-3}c$ *(-).*

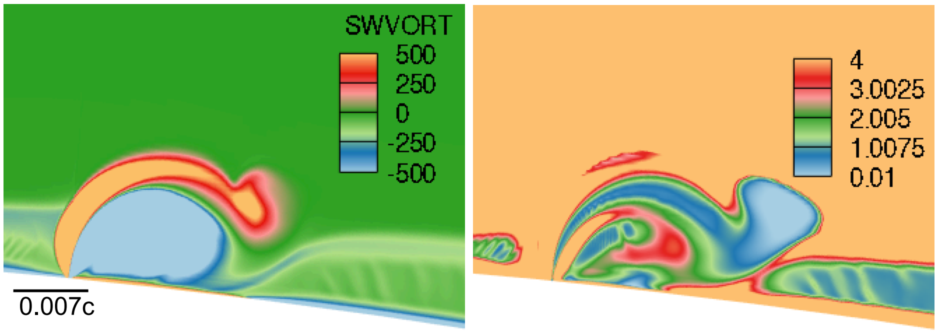

(a) Spanwise vorticity (b) r_k

Figure 7.8: Early pulse structure $0.01t_{conv}$ *into the pulse.*

Application of the pulse results in transient lift enhancements over approximately $4t_{conv}$ with maximum efficacy occurring $4t_{conv}$ after application of the pulse (Fig. 7.7). The enhanced lift coefficient peaks at $C_L \approx 2.5$ or nearly 50% higher than the mean lift. Experimental single pulse change in circulation transients found a return to stall after $7-10t_{conv}$ with a peak at $3t_{conv}$ after application of the pulse [2,3]. Thus, simulations reproduce the reattachment process of the experiment but not the return-to-stall. However, this is actually a misleading result. As we will discuss, an atypical event occurs which disrupts the reattachment and baseline flow. Nonetheless, as the reattachment process has been successfully reproduced, flow structures revealed in the simulations can be used to understand the physics driving the reattachment process.

The early formation of the initial pulse-induced vortex, $0.01t_{conv}$ after initiation of the pulse, is shown in Fig. 7.8 along with the resolution adequacy parameter. Directly in the pulse jet, $r_k \gg 1$ and the simulation functions as a RANS. Along the edge of actuation and at a distance of approximately 0.005c from the actuator orifice along the jet, r_k lowers to below unity and the simulation begins to resolve some of the turbulence. The vortex forms from the roll-up of large negative spanwise vorticity resulting from the downstream jet shear layer. The upstream jet shear layer results in regions of positive vorticity which convect over and around the vortex. This is similar to behavior described in [2] with a positive signed vortex convecting over the negative vortex and being shed. (Fig. 2.1). The actuation structure resulting from this roll-up of the downstream edge of actuation shear layer suggest angling the pulse downstream will enhance its formation.

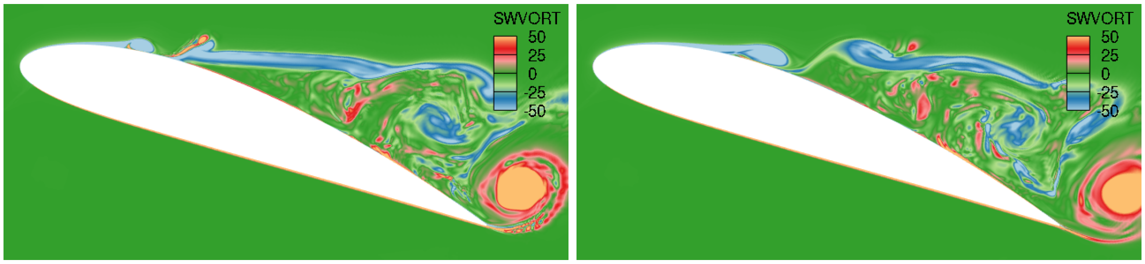

(a) $0.1t_{conv}$

(b) $0.3t_{conv}$

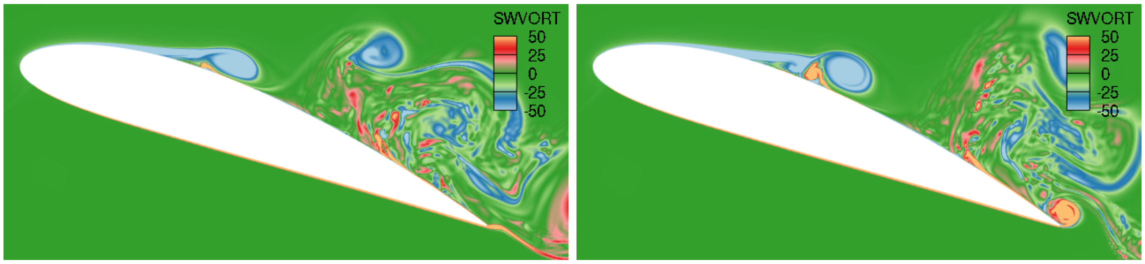

(c) $0.5t_{conv}$

(d) $0.7t_{conv}$

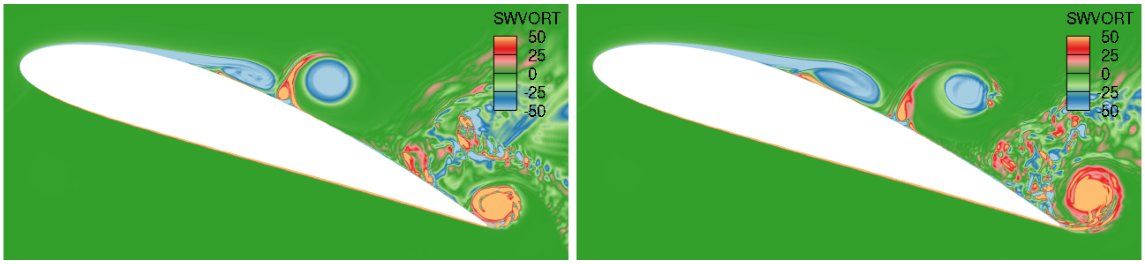

(e) $0.9t_{conv}$

(f) $1.1t_{conv}$

Figure 7.9: Reattachment process: normalized spanwise vorticity at intervals of $0.1t_{conv}$ *after completion of a single pulse using the hybridized* $\overline{v^2}$*-*f *model with a minimum resolution of* $2.5 \times 10^{-3}c$ *imposed on* $\mathcal{M}$*.*

The reattachment process is shown in Fig. 7.9 with physical mechanism described as follows. A leading negative-signed vortex moves along the airfoil surface. A positive-signed vorticity region is pulled up along the trailing edge of the leading vortex. This oppositely signed vorticity region causes the leading vortex to severe from the separated shear layer. The new leading edge of the separated shear layer rolls up behind the oppositely signed vorticity region forming a new negatively signed vortex which begins to repeat the process. The pulse-induced vortex serves as the “seed” vortex to initiate the process. The distance the boundary layer is able to move down the airfoil surface (directly corresponding to the lift enhancement) is proportional to the strength of the leading vortex.

The process is nearly identical to that observed for simulations using 2D DDES (§4.2) however, it has now been successfully reproduced in 3D and appears to be no longer overly stable with the reattachment structures gradually losing their strength due to resolved turbulence and three dimensional subgrid dissipation (Fig. 7.11). The weakening of each successive leading vortex is visible in the reduced vorticity strength and increasing size of the structure (compare the progression of the leading vortex from Fig. 7.9d to Fig. 7.11a and so on). Thus, the initial goal for constructing the new hybrid method has been achieved. However, the return-to-stall process was disrupted by the interaction between a shed reattachment vortex and a trailing edge (Fig. Fig.7.11d).

As the now large shed reattachment vortex passes over the trailing edge, its accompanying pressure depression creates a large negative pressure gradient towards the vortex core (Fig. **??**). The trailing edge shear layer is pulled towards the passing vortex causing it to roll-up on the suction-side surface of the airfoil. This interaction causes the reattachment structures to be “knocked” off from the airfoil surface resulting in a massive stall event. While this sort of event has not been reported in any of the GaTech experiments, it is plausible that it occurs and is just lost in the phase-locked averaging of 100s of individual pulses. These detrimental events may occur at random when the pulse is applied at just the wrong time in the dynamic stall period. Alternatively, and perhaps more likely, the periodic shallow span combined with incompressibility results in abnormally low vortex core pressures with increasing vortex size which are not physical. Additional simulations with the

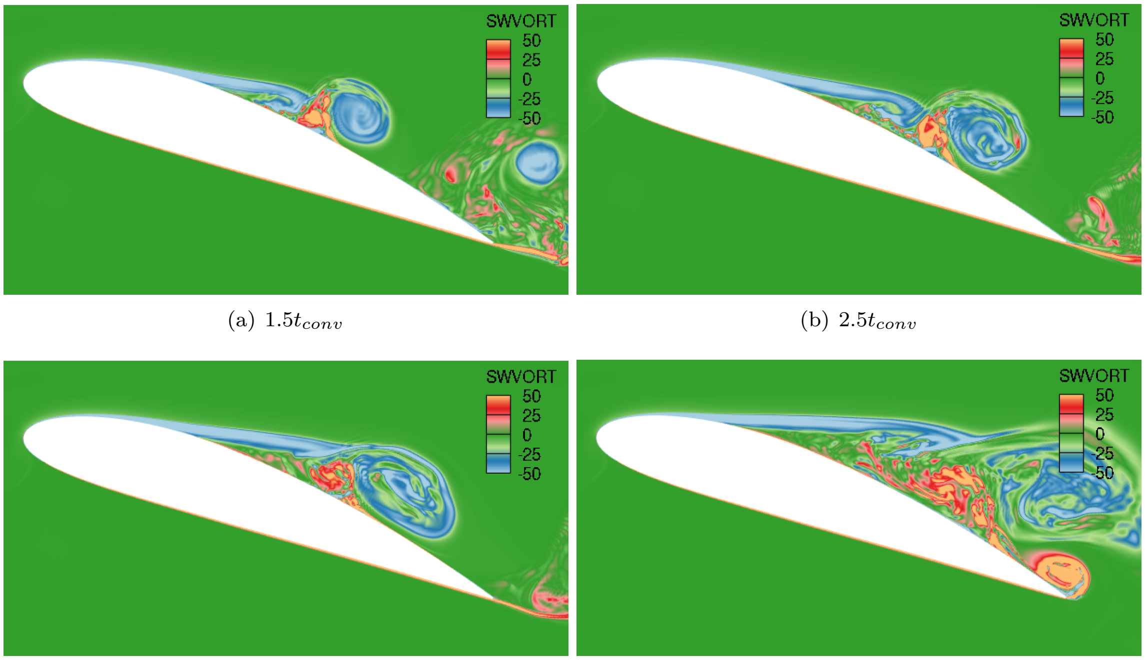

(a) $1.5t_{conv}$ (b) $2.5t_{conv}$

(c) $3.5t_{conv}$ (d) $4.5t_{conv}$

Figure 7.10: Return-to-stall process: normalized spanwise vorticity at intervals of $0.1t_{conv}$ *after application of a single pulse using the hybridized* $\overline{v^2}$-f *model with a minimum resolution of* $2.5 \times 10^{-3}c$ *imposed on* $\mathcal{M}$.

pulse applied at offset intervals are needed to evaluate this hypothesis.

Simulation of a finite span actuation zone has not yet been performed due to time constraints and remains an active goal. We anticipate these simulations will reveal the formation of streamwise vortices along the edge of actuation region which will entrain high momentum fluid from above the separation region and enhance the efficacy of the pulse as suggested by experimental observations.

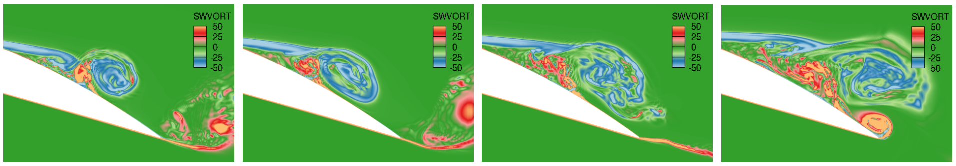

(a) ω_z $3.0t_{conv}$ (b) ω_z $4.0t_{conv}$ (c) ω_z $4.5t_{conv}$ (d) ω_z $5.0t_{conv}$

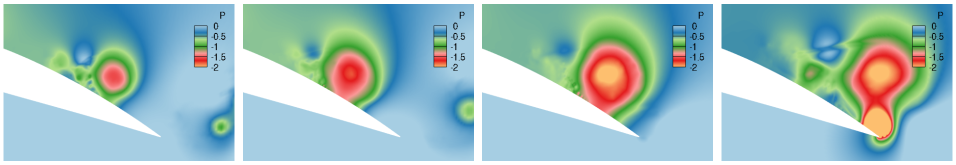

(e) p $3.0t_{conv}$ (f) p $4.0t_{conv}$ (g) p $4.5t_{conv}$ (h) p $5.0t_{conv}$

Figure 7.11: Normalized spanwise vorticity (a-d) and accompanying pressure field (f-h) leading to the massive stall event at $5t_{conv}$*. Vortex core pressure depressions increase with vortex size to the point where the shed reattachment vortex pulls in the trailing edge shear layer causing it to rollup on the airfoil surface.*

Chapter 8

Conclusion and Recommendations

Sometimes things become possible if we want them bad enough.

-T.S. Eliot

The simulation of pulse-actuated dynamic stall control is a particularly challenging problem for hybrid RANS/LES modeling techniques. Application of SA-based DDES to this problem yielded unsatisfactory results where the modeled combustion pulse experienced premature breakup resulting in ineffective actuation in direct contradiction to experimental evidence. Upon examining the failure of these attempts in detail, multiple issues related to the treatment of complex grids and inappropriate and often too rapid RANS/LES transition became evident.

Smooth-wall separation in the presence of adverse pressure-gradients is already known to be problematic for turbulence models. However, in this case, pulse-induced vortices travel through and interact with the attached boundary layer, the fluctuating separation point, and the downstream separation region. Resolution of these structures is critical for capturing the reattachment process yet given their movement along the airfoil surface, hybrid models will either attempt to model them as a RANS or be so biased towards LES that the attached boundary layer will all or partially be modeled as an under resolved LES resulting in premature separation. Furthermore, actuator resolution requirements in the attached boundary layer result in rapid transition to a local LES causing incorrect levels of total turbulent stress spoiling the fidelity of the solution far away from the actuator. These issues are all traceable to transition with either no regard for or ad-hoc consideration of the local flow coupled with insufficient crude scalar measures of the highly anisotropic cells in the boundary layer. To simulate pulse-actuated stall control, a new hybrid approach was necessary.

To address the challenges described above, a promising new hybrid modeling approach has been developed. The approach relies on four improvements:

1. A novel subgrid stress model using the filtered two-point, second-order structure function composed of a measure of the grid and resolved turbulence anisotropy to define an anisotropic eddy-viscosity model;
2. An anisotropic diffusivity-based model of the effects of resolution inhomogeneity in LES;
3. A new energy conserving RANS/LES transition approach accounting for anisotropy in both the resolution and the state of the resolved field, which transfers energy between the resolved and modeled scales at a physically realistic rate; and
4. Reliance on a RANS model, specifically Durbin's $\overline{v^2} - f$ model [36], that provides Reynolds stress anisotropy information and has no explicit dependence on distance to the wall.

The resulting new method fundamentally differs from existing hybrid techniques in three main ways: (i) transition is based on maintaining a balance between resolved and modeled scales, (ii) the evolution of the resolved scales due to changing resolution is governed by the turbulence itself and not explicitly defined by the available resolution, and (iii) the entire approach is structured to make hybrid simulations amenable to complex flows and geometries.

In the new method, model stress is guided by the balance between the resolved and modeled scales.

This is achieved by considering the current state of the resolved field for transition in addition to the grid size to form a theoretical estimate of the unresolved turbulence for comparison with the modeled quantity. Under the conditions of equivalence between the resolved scales and the available resolution, hybrid behavior will be similar to that of a DES. However, when this is not the case, the new approach has significant advantages. Rather than immediately assume the existence of resolved scales of turbulent motion at the grid size, the resolved field is allowed to adjust gradually towards the scales of motion supportable by the grid. The rate of this transition is limited based on the turbulent timescales at the filter in order to maintain statistical accuracy of the evolving resolved field. Under the conditions of modeled turbulence convecting into regions of higher resolution, the phenomenon of modeled stress depletion and its resulting deleterious effects such as grid-induced separation are circumvented by this transition strategy. Though overlooked in the literature, the opposite case of excess modeled stress is also corrected. As resolved turbulence is convected into more coarse regions, modeled stress will only increase with the removal of resolved turbulence as opposed to experiencing a jump resulting from the combination of a larger grid size and the remaining (and now unsupportable) large resolved gradients from the previous more refined region. While this “doubly” increased model stress would more rapidly remove resolved turbulence, the total turbulent (resolved plus modeled) seen by the mean flow would be erroneously high causing the entire simulation to lose fidelity.

Flows of engineering interest typically contain historically challenging phenomena for simulations such as regions of separation and reattachment while body geometries and domains require rapidly varying cell sizes of high aspect ratios. The presented hybrid framework is constructed to naturally handle precisely these scenarios. The use of the $\overline{v^2}f$ model as the base turbulence model allows for accurate prediction of near-wall model stress in both attached and separated regions which in turn dictates appropriate RANS/LES transition in both regions. Hybridization based on wall-distance suffers in such situations as wall distance makes no distinction between attached and separated flows necessitating secondary and often ad-hoc indications of flow behavior. As opposed to relying on a scalar measure of complex grid sizes, grid anisotropy is directly integrated into both the form of the subgrid stress model and in the hybridization. This has the distinct advantage of the SGS model dissipating the correct amount of resolved momentum in every orientation of the field while also preventing transition based on unresolvable orientations. Finally, grid heterogeneity is specifically accounted for by introduction of a commutation-error correction model which assists in the transfer of energy from resolved and modeled scales in the presence of convection through grid inhomogeneity.

Though much work (characterization, validation and refinements) are yet to be performed, the hybrid model developed in this work is expected to be applicable to a wide variety of complex turbulent flows, with minimal user intervention, thus providing robust predictive capability.

8.1 Stall Control

While the original scope of dynamic stall control simulations has been drastically reduced due to the difficulties experienced with initial simulation attempts using DDES and the development and implementation of the new hybrid method, new insight into the fundamental process responsible for reattachment has been attained. We now briefly summarize the findings from application of the new hybrid method to the difficult problem of pulse-actuated dynamic stall control.

8.1.1 Summary of Findings

Using the newly developed hybrid method, accurate smooth-wall separation behavior was attained with varying model resolution including the highly refined grid sizes in the vicinity of the actuator. The latter was not possible with DDES as the actuator resolutions resulted in local transition to LES tripping the attached boundary layer. However, using a very crude approximation of the combustion pulse, the model resolution minimum was still necessary to form an initial pulse-induced vortex favorable for the reattachment process. This necessity can be attributed to a combination of the severe limitations imposed on the resolution inhomogeneity correction term and the local resolution attempting to resolve turbulent content much smaller than the initial vortex coupled with the lack of any of this detail due to the incompressible and uniform pulse jet simplifications.

A repeating vortex-wall interaction process has been identified as the physical mechanism responsible for pulse-actuated dynamic stall control. In this process, a leading vortex travels along the stalled airfoil surface with the separated shear layer trailing. The strong negative vorticity of this leading vortex pulls up a region of positive vorticity in its wake as it travels along the wall. The positive vorticity region grows outward and severs the leading vortex form the separated shear layer causing the former to be shed and the latter to roll-up into another negative signed leading vortex. The process then repeats moving further down the airfoil surface. The combustion pulse provides the initial leading vortex. The process terminates as each successive leading vortex weakens due to turbulent dissipation.

With this knowledge, we can begin to optimize the vortex-wall reattachment process. Possible avenues include designing the actuator to maximizes the strength of the initial pulse-induced vortex or inclusion of secondary actuators further along the airfoil surface which serve to reinvigorate the leading vortices as they lose their strength with precisely timed pulses thus maintaining reattached flow continuously.

8.2 Recommendations for Future Work

The new modeling approach presented in Chapter 5 is very much preliminary in nature. Though the results of early use in Chapters 6 and 7 have been encouraging, each aspect of the modeling framework, as well as their integration, should be rigorously evaluated and refined individually. Here, we make specific suggestions to advance the proposed method and hybrid modeling in general.

8.2.1 Anisotropic SGS model

There are several open issues that remain regarding the anisotropic subgrid model formulation described in §5.2. In particular, the model forms described were developed through dimensional and tensor analysis by analogy to the structure function model [38]. However, other functional forms are possible, which may perform better, be more generally applicable, or be easier to compute. The development of the anisotropic SGS model only theoretically considered anisotropy in the filter (though it may be successful for mild turbulence anisotropy due to its construction through the anisotropic resolved field). The turbulence at the filter is assumed to be homogeneous and isotropic. It may be possible to add a model for Reynolds stress anisotropy to filter anisotropy component addressed here. As previously mentioned, addition of a traceless Clark model like term [103] would be a good starting point. Alternatively, uncontracted fourth-rank tensor forms of velocity differences across $\mathcal{M}$ could be explored.

The most appropriate anisotropic subgrid model should be determined through a series of statistical *a priori* tests in homogeneous anisotropic turbulence and high Reynolds number channel flow. These tests should include direct numerical simulations of several homogeneous flows including strained, rotating and sheared turbulence. Recent high Reynolds number channel DNS [106] is immediately available to begin this task. Anisotropic filters can be applied to the DNS data and the statistics of the resulting true subfilter stress compared to the statistics of the the anisotropic model. This will allow the anisotropic model to be refined and become broadly applicable. The same DNS flows can also be used for so-called *a posteriori* tests. LES of the sample flow will be performed using the anisotropic model on several anisotropic grids. The statistical results can then be compared to those of the filtered DNS.

The development and testing effort described here will result in a subgrid model that reliably characterizes the effects of anisotropic grids and anisotropic unresolved turbulence. This will be of great use in LES in general, but as described in §5.3 will be particularly useful in hybrid RANS/LES modeling.

8.2.2 Hybridization

While the hybridization approach described here has been found to perform well in the tests conducted so far, there is a need for further testing of the foundations of the technique. Jumping to the very complex problem of pulse-actuated dynamic stall control is very much "putting the cart before the horse". Testing and refinements of the hybrid RANS/LES method should begin with more fundamental and canonical problems. Perhaps the foremost problem should be evaluation of the hybrid method in attached turbulent boundary layers with refining resolution. This simple test will reveal if the primary design objective of the new hybrid method has been achieved– namely, that transition from RANS to LES and the exchange of energy between the resolved and modeled scales truly occurs in a manner which allows statistically meaningful turbulence to naturally develop. Further complexities, such channel flow with a hump, can be added to this case to rigorously quantify the hybridization behavior for challenging problems of smooth-wall separation and reattachment in the presence of pressure gradients.

Each element of the hybridization framework should be examined in detail. Using data from the DNS identified in §8.2.1, the estimate of the unresolved energy based on Q can be tested and if necessary refined. The resolution parameter, r_k, can be enhanced to account for non-local and non-equilibrated effects as well as account for resolutions approaching the Taylor microscale and Kolmogorov scale. Finally, the ability of the simple form of (5.8) to appropriately limit the energy exchange between resolved and unresolved turbulence should be rigorously tested by examining the energy spectrum of evolving LES in comparison with filtered DNS with refinements pursued as needed.

8.2.3 Resolution inhomogeneity treatment

The resolution inhomogeneity correction as presented in §5.4.1 requires the somewhat ad-hoc restrictions presented in §5.4.2 to maintain simulation stability and preserve consistency with the intent of the hybridization. This necessity is not only unsettling from the standpoint of basic implementation but also from the overall design approach. Ideally, we would like the term to adapt naturally by construction. It would be a worthwhile endeavor to attempt integration of the effects of the limitations into the model itself. Just how to do so remains unclear to the author at this time. Nonetheless, the correction term as-is should be tested in LES of isotropic homogeneous turbulence with convection through grids of varying size. The ability of the term to correctly govern the exchange of resolved and modeled energy as the filter width changes can be accessed by again comparison with filtered DNS data. These results would help characterize its behavior, guide further development, and illuminate under precisely what circumstances such a term is necessary to preserving the fidelity of an LES.

8.2.4 General improvements

As presented, there are no explicit limitations or assumptions which would prevent straightforward extension of the hybridization framework to compressible flows when using compressible RANS models (e.g., [56]) and the compressible LES formulation to be developed as part of this work. In particular, the resolution adequacy parameter (5.7) is contingent only on the two-point second-order structure function approximation and inertial range theory to estimate the unresolved turbulent kinetic energy which are not based on the incompressible assumption. Hybridization would then only indirectly affect the additional density and temperature equations associated with compressible flow simulations. However, these claims must be confirmed by evaluation of the performance of the hybrid model in compressible flows using cases such as the transonic axisymmetric bump [107] and the compressible mixing layer [108]. Demonstration of the method in compressible settings would aid its acceptance in the turbulence modeling community and subsequent potential development.

The inability of establishing an accurate estimate of the resolved turbulent kinetic energy for generally unsteady flows has been mentioned repeatedly throughout this work. The difficulty is rooted in having no computationally feasible method of determining the ensemble average of the flow. The lack of this vital piece of information is responsible for some of the more ad-hoc components of the presented material, in particular:

- the use of $r_k \gg 1$ to approximately establish regions of RANS operation (5.12 and 5.21),
- the use of model quantities in place of resolved turbulence quantities (T_m in (5.8) and k_m in (5.20)) , and
- and the necessity of imposing a maximum of 1 on α which restricts responsiveness of the hybridization.

The ability to discriminate between the unsteady flow and resolved turbulence would greatly enhance the overall hybrid framework presented here[1]. Of course, this is a pre-existing issue with unsteady RANS in general.

---

[1] See §B.8 for a reformulation of the hybrid method which would allow determination of k_{res} and solve multiple issues outlined above.

Finally, the hybrid framework as presented in compartmentalized. Ideally, the entire system would be integrated in a manner which obviates individual control and restrictions of each component. One possible avenue to achieve this is to turn to a single length scale transport equation, similar to Rotta's kL model used in Scale Adaptive Simulations (SAS) [109], which models the least resolved possible turbulent scale. Transition between RANS and LES (that is, L_m between L_{RANS} and $\mathcal{M}$) would be incorporated into the production term so that the exchange of resolved and modeled turbulent energy would again occur at a physical rate allowing for the development of statistically meaning turbulence. This advanced production term would take the place of both the blending parameter and inhomogeneous correction term used here. Subgrid stress anisotropy would be built in similar to the method used here. Such a treatment could potentially achieve the ultimate hybrid modeling objective of a truly independent and robust hybrid model which naturally optimizes the available resolution in a physically consistent manner.

8.3 Concluding Remarks

The initial goal of a comprehensive simulations-based study of pulse-actuated dynamic stall control illuminating the entire physical process responsible for reattachment and allowing for rapid optimization and implementation in experimental airframes has not been achieved. However, the root causes behind the deficiencies of existing hybrid methods responsible for this shortfall have been identified and individually addressed in a preliminary fashion. The resulting new hybrid method is very promising but requires further development and improvement. This represents a significant departure from previous methodology which serve as a basis for progress in applied turbulence modeling and simulation. The result could be a truly transformative reformulation of hybrid modeling.

Appendices

Appendix A

CDP Details and Modifications

A.1 Computational Improvements

A branch of the existing finite volume incompressible Navier Stokes solver CDP v2.4 [105] developed at the Center for Turbulence Research (CTR) Stanford is used as the code base. To accommodate large computational domains needed for staggered actuator arrays with spanwise domains, external and more efficient PETSC[1] solvers have been integrated into CDP. The previous built-in solvers suffered from significant communication overhead and used only Jacobi preconditioning. PETSC solvers are optimized for massively parallel execution and have more efficient preconditioners, such as ILU, available. Integration of PETSC required significant re-writing of the existing code but resulted in over six times total speed up. Additionally, the construction of PETSC operators has been implemented to accept tensor valued viscosities.

---

[1] available: www.mcs.anl.gov/petsc

A.2 Treatment of Convection

As has been demonstrated by multiple studies [110], the use of upwind differencing schemes (UDS) in an LES is not desirable due to numerical dissipation at high wavenumbers being on the order of the SGS dissipation while central difference schemes (CDS) have effectively no artificial numerical dissipation. However, dispersion error and resulting spurious oscillations can occur for any advection problem where local cell Reynolds numbers based on total viscosity (model plus molecular) are much larger than unity using a purely CDS. Conventional wisdom dictates a UDS should be implemented only where the LES model is not active. Travin *et.al.* have proposed and demonstrated a system to detect where applying upwinding is appropriate [111]. However, given that we already know where the model is active, such an additional treatment may be superfluous.

In this work, an extremely mild dynamic UDS, based on local cell Reynolds number using the total viscosity, has been implemented for computation of each convective face flux. Consider the cell face Reynolds number

$$Re_f = \frac{|u_i n_i|(s_j s_j)^{\frac{1}{2}}}{\nu + \nu_t}, \tag{A.1}$$

where n_i the cell face normal, s_i the face-sharing cell center-to-center vector. It is wholly undesirable for this value to be of order one in an LES. Were this true, the inertial and viscous forces would be balanced at the filter cutoff resulting in a large roll-off of the resolved turbulent energy similar to between the Taylor microscale and Kolmogorov scale for fully resolved flows. Such behavior would defeat the purpose of an LES. Instead, we desire the local cell Reynolds number to be equal to the Reynolds number of the unresolved turbulence, $Re_T = \frac{k_{mod}^2}{\nu\epsilon}$. In doing so, the resolved behavior is consistent with the unresolved field at the cutoff.

Enforcing this conditions is performed be taking an approximate artificial face-based UDS numerical diffusivity [112] as $\nu_{UDS}^f \approx w_{UDS}^f |u_i n_i|(s_j s_j)^{1/2}$ where w_{UDS}^f is the face UDS weight. We then require the face Reynolds number including ν_{UDS}^{f} to equal Re_T. Upon rearranging, one obtains

$$w_{UDS}^{f} = \frac{Re_f - Re_T}{Re_f Re_T}, \tag{A.2}$$

with the additional restrictions of

$$Re_T = \max(Re_T, 1), \tag{A.3}$$

$$w_{UDS}^{f} = \max(w_{UDS}, 0), \text{ and} \tag{A.4}$$

$$w_{UDS}^{f} = \min(w_{UDS}, 1). \tag{A.5}$$

Matching cell and subgrid Reynolds numbers is a consistent (with respect to the spectral distribution of turbulent energy) method to determine the degree of upwinding for momentum in an LES. As the balance between inertial to viscous forces for scalar variables at the filter size has no physical meaning, upwinding of model transport terms may be set such that solution stability is maintained. The most conservative selection would be to use (A.2) with unity in place of Re_T.

A.3 Skewness Correction with Tensor Viscosity

The standard finite volume gradient is calculated using divergence theorem

$$\partial_j \phi = \frac{1}{\delta V} \sum_{f} \phi n_j^f A^f \tag{A.6}$$

where f indicates the face quantity and δV is the cell volume. To correct for cell face skewness when calculating second derivatives, Zwart proposed including a portion of the average cell values from adjacent cells, such that face normal gradients $\partial_n \phi$ used in determining second derivatives are expanded as

$$\partial_n \phi = \partial_i \phi^f n_i^f \approx \partial_i \phi^f \alpha s_i + \partial_i \phi^f (n_i^f - \alpha s_i) \tag{A.7}$$

which is then approximated as

$$\partial_n \phi \approx (\phi^{nbr} - \phi^p)\frac{\alpha}{|s|} + \frac{1}{2}(\partial_i \phi^{nbr} + \partial_i \phi^p)(n_i^f - \alpha s_i) \tag{A.8}$$

where $\alpha = s_i n_i$ and s_i has been normalized by the magnitude of the distance $|s|$. Let us apply this to our tensor viscosity. The first portion of the modeled stress (5.2) would be

$$\partial_j\left(\nu^t_{jk}\partial_k u_i\right) = \frac{1}{\delta V}\sum_f F^f_{ij} n^f_j A^f \tag{A.9}$$

where

$$F^f_{ij} n^f_j = (\nu^t_{jk}\partial_k u_i)|_f \approx (u_i^{nbr} - u_i^p)\frac{s_j \nu^f_{jk} n^f_k}{|s|} + \frac{1}{2}[\partial_k u_i^{nbr} + \partial_k u_i^p]\nu^f_{jk}(s_j - n^f_j), \tag{A.10}$$

where the face averaged viscosity is ν^f_{ij} is the average of the face-sharing cells. The gradients appearing in (A.10) may be explicitly defined using the previous time step. However, for solution of the f scalar equation (3.14), which has no time history effects, an implicit treatment is necessary. While the standard finite volume treatment could be used, this would result in significantly more complicated stencils and associated solution times. Instead, the approximation

$$\partial_k u_i^f \approx (u_i^{nbr} - u_i^p)\left[\frac{2A^f}{\delta V^{nbr} + \delta V^p}\right] \tag{A.11}$$

is used.

The second term of (5.2) does not require special treatment as incompressibility may be used to reduce the term to only the contraction over two first derivatives ($\partial_j(\nu_{ik}\partial_k u_j) = \partial_j \nu_{ik}\partial_k u_j$).

A.4 Basic Code Verification

It was discovered that the code contained major errors in previous versions which were thought to be reliable. To ensure these bugs have been corrected, some basic verification has been performed. The verification cases include 2D and 3D simulations of a smooth cylinder in crossflow at Re_D from 0.1 to 10K. The domain is a simple O-mesh of 40D diameter with initial wall normal spacing of 1x10^{-4}D, wall tangent spacing of 1x10^{-2}D, and a final radial spacing of 1D. The result is 200 cells in the wall normal directions with a growth of approximately 5% at each level. For the 3D cases (Re_D of 1K and 10K), the span of the cylinder is 2πD discretized with cell spacing of approximately 0.196D.

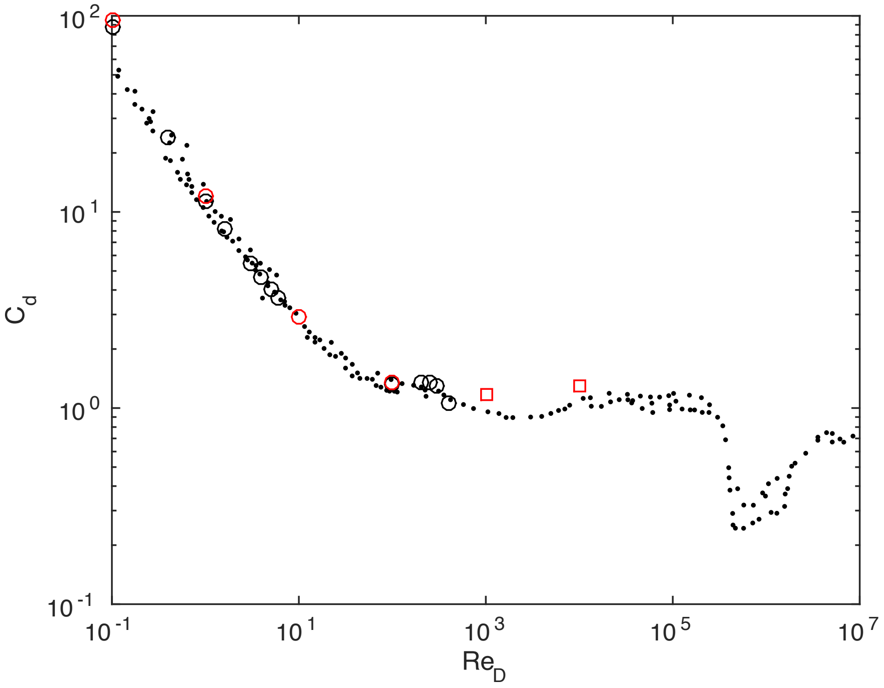

Figure A.1: Comparison of simulations results for a cylinder in crossflow using current modified CDP code (2D: ○ and 3D: □) with experimental data (·) of [4–8] as accumulated by and reproduced from [9] and the simulations (○) of [11]. The k-ϵ model is active for only Re_D of 1K and 10K simulations.

Results are shown in Fig. A.1 with comparison to the experiments of [4–8] and the simulations of [11] using the same domain size. Averages are taken over 50 convective times. The lowest Re_D simulations at 0.1 produce a drag coefficient which is significantly higher than experiments. This is due to the 40D domain being too small with viscous effects extending far away from the cylinder. The two 3D cases are slightly above the experimental value. This can be attributed to the rather coarse spanwise resolution. Otherwise, the simulation results are very close to experimental measurements and other simulations.

While these tests do include activation of the k-ϵ model in the turbulent wake at Re_D of 1K and 10K, they are not rigorous tests of their implementation. Moreover, they do not activate the $\overline{v^2}f$ model. The fidelity of the turbulence models relies on use of the implementation verified in [81]. However, additional verification should be performed.

Appendix B

Additional Model Details

B.1 On the relation between eddy viscosity models and τ_{ij}

Let us further examine the implications of the relation between velocity differences in the structure function and the unresolved turbulent kinetic energy. If the turbulence at the filter size is isotropic, then at every point $(u'_i)^2 \approx \frac{2}{3}k_{sgs}$. With (3.25), we know $(u'_i)^2 \approx C\overline{F_2}$ or equivalently, $(u'_i)^2 \approx C\overline{\delta U_i}\overline{\delta U_i}$. Therefore, eddy viscosities of the Smagorinsky and SF form are also $\nu_{SGS} = C\Delta_c(u'^2)^{1/2}$ (*i.e.* the same form as basic RANS eddy viscosities). Expand the exact τ_{ij} definition (3.18) with the total decomposed velocity field as

$$\tau_{ij} = \overline{\overline{U}_i\overline{U}_j} - \overline{U}_i\overline{U}_j + \overline{\overline{U}_i u'_j} + \overline{u'_i\overline{U}_j} + \overline{u'_i u'_j} \tag{B.1}$$

and the eddy viscosity model τ_{ij} definition (3.20) with the eddy viscosity of the form

$$\tau_{ij} = C\Delta_c\big((u'^2)^{1/2}\overline{U}_{i,j} + (u'^2)^{1/2}\overline{U}_{j,i}\big). \tag{B.2}$$

Recognize that the cutoff size and the gradient operator form a filtered change in velocity across Δ_c, $\Delta_c\partial_j u_i \approx \overline{\delta u_{ij}}$, such that

$$\tau_{ij} \approx C\big((u'^2)^{1/2}\overline{\delta U_{i,j}} + (u'^2)^{1/2}\overline{\delta U_{j,i}}\big), \tag{B.3}$$

and once again invoke the implication that $(u')^2 \approx (C\overline{\delta U})^2$ yielding the approximate relationship

$$\tau_{ij} \sim (u'^2)\left(\frac{\overline{U}_{i,j}}{\overline{U}_{k,k}} + \frac{\overline{U}_{j,i}}{\overline{U}_{k,k}}\right) = (u'^2)\frac{S_{ij}}{S_{kk}}. \tag{B.4}$$

Compare the exact (B.1) with the approximate model form of (B.4) and we see eddy viscosity models carry the magnitude of fluctuating-fluctuating term $\overline{u_i'u_j'}$ but with anisotropy set by the large scale strain rate tensor.

Advancing SGS models which are generally applicable and do not require specific flow tuning requires acknowledging basic eddy-viscosity models are subject to the limitation that, at their best, they can only possibly model a portion of the exact SGS term. However, with the above analysis in mind, we can clearly construct more complete models which account for the entire τ_{ij} term. Doing so will require carefully consideration for how discrete gradient operators imply additional grid filtering and the approximations for anisotropy in τ_{ij} given the available information in the resolved field and resolution.

B.2 Approximate $\mathcal{M}$ for finite volume based simulations

In §5.2, we dissuces $\mathcal{M}$ in terms of a transformation from a unit cell to the global cell. This is straightforward to implement in a finite element code as the the Jacobian of this transformation is already calculated. For finite volume methods however, a more direct and geometric interpretation is easier to implement. We may alternatively think of $\mathcal{M}$ as a desired resolution where we are free to dictate the scale of features we are interested in resolving provided this scale is supported by the underlying grid. To this end, we define the separation tensor as the desired resolution. For hexahedral cells, consider the vector connecting the centers of opposing faces, l_i^p, where p indicates each of the three face pairs. We may construct $\mathcal{M}$ as

$$\mathcal{M}_{ij} = e_{mi} L_{mn} e_{nj} \tag{B.5}$$

with $\mathbf{e}$ composed of the normalized opposing face-to-face directions in rows ($l_i^p/|l_i^p|$, approximate cell eigenvectors) and $\mathbf{L}$ a diagonal matrix composed of the magnitude of the maximum of the components of l_i^p and the desired resolution scale, l_i^{res}, in each direction (approximate cell/resolution eigenvalues). Thus, in regions where the grid is more refined than our desired resolved scale, a uniform resolution field is imposed preventing changes in grid resolution from adversely affecting resolved flow structures. In more coarse regions, (perhaps we do not need to resolve small features everywhere in a computational domain) the resolution tensor defaults to a grid description.

B.3 Constant C_F for approximation of unresolved turbulent kinetic energy

Here, the constant relating the structure function to the unresolved turbulent kinetic energy is derived. This is essentially performed in [38] but their end goal was a viscosity constant such that C_F as presented here was not directly given. Begin by assuming homogeneous isotropic turbulence with a Kolmogorov inertial range

$$E(\kappa) = C_k \epsilon^{\frac{2}{3}} \kappa^{-\frac{5}{3}}, \tag{B.6}$$

where the wavenumber is related to a physical length scale, Δ, as $\kappa = \frac{\pi}{\Delta}$. The two-point second order structure function at separation distance r is related to the turbulent energy spectrum. For isotropic homogeneous turbulence [70]

$$F_2(r,t) = 4\int_0^\infty E(\kappa,t)\left(1 - \frac{sin(\kappa r)}{\kappa r}\right) d\kappa, \tag{B.7}$$

and upon assuming a Kolmogorov spectrum (B.6) and integrating from 0 to ∞

$$F_2(r,t) = 4.82 C_k (\epsilon r)^{\frac{2}{3}}. \tag{B.8}$$

The total subgrid (as defined by r) turbulent kinetic energy may be approximated by integration of (B.6) from $\kappa_c = \frac{\pi}{r}$ to ∞ such that

$$k_{sgs} = \frac{3}{2} C_k \epsilon^{\frac{2}{3}} \left(\frac{r}{\pi}\right)^{\frac{2}{3}}. \tag{B.9}$$

Rearranging (B.9) with (B.8) yields

$$k_{sgs} = \frac{3}{2}\frac{1}{4.82\pi^{2/3}}F_2(r,t). \tag{B.10}$$

Now, F_2 is the total structure function. When calculating F_2 from the resolved field, we are actually approximating the filtered structure function $\overline{F_2}$ with r approximately equation to the cutoff length scale, Δ_c. The contribution of the unresolved scales (F_2') to the total structure function,

$$F_2 = \overline{F_2} + F_2', \tag{B.11}$$

can be approximated by again assuming (B.6) and integrating (B.7) from κ_c to ∞ yielding

$$F_2'(r,\Delta_c) = F_2(r)\left(\frac{r}{\Delta_c}\right)^{-\frac{2}{3}} H\left(\frac{r}{\Delta_c}\right), \tag{B.12}$$

where

$$H(\gamma) = \frac{4}{4.82}\int_{\pi}^{\infty} \delta'\left(1 - \frac{sin(\delta'\gamma)}{\delta'\gamma}\right)d\delta'. \tag{B.13}$$

Combining (B.11) and (B.12) yields

$$F_2(r) = \left[1 - \left(\frac{r}{\Delta_c}\right)^{-\frac{2}{3}} H\left(\frac{r}{\Delta_c}\right)\right]^{-1}\overline{F_2}(r). \tag{B.14}$$

If the separation distance and filter are taken to be equal ($r = \Delta_c$), $F_2 = 2.53\overline{F_2}$. Thus, the final constant relating the filtered structure function to the unresolved turbulent kinetic energy at scales smaller than r ($k_{sgs} = C_F\overline{F_2}(r)$) is

$$C_F = \frac{3}{2}\frac{2.53}{4.82\pi^{2/3}}, \tag{B.15}$$

or $C_F \approx 0.367$. Let us now discuss come caveats associated with the applicability of this simple relation.

Throughout this derivation, the Reynolds number has been assumed to be infinite with the inertial range defined by (B.6) extended to ∞. This does not account for rolling off about the Kolmogorov length scale, η. As a result, as r approaches η, k_{sgs} will be over predicted. However, where r is larger than the Taylor microscale ($L_\lambda^2 \approx 10\frac{\nu k}{\epsilon}$), the approximation is reasonable. Finally, as Q in (5.1) is calculated using $\mathcal{M}$ which we have allowed to be larger than local grid size, the implication that $r = \Delta_c$ becomes questionable. That is, implicit grid filtering at the grid size is performed when calculating velocity gradients. Composing the filtered structure function approximation, *i.e.* Q, using these gradients and a larger separation distance via $\mathcal{M}$ implicitly assumes the model is removing all scales of motion between $\mathcal{M}$ and the actual grid. This is not true, in general. In fact, when using a diffusivity based eddy viscosity model, where $\mathcal{M}$ is larger than the grid, not only will there be energy at scales smaller than $\mathcal{M}$, but there will also be erroneously reduced energy at scales larger than $\mathcal{M}$. The resolved field will be "smeared" across all available scales of resolution up to the grid length scale even though the model is attempting to remove all energy at scales smaller than $\mathcal{M}$.

B.4 Aside on improving basic DES

Though the goal of this work is not to improve DES, introducing $\mathcal{M}$ provides a clear avenue to remove ambiguity in defining the scalar grid length scale. Rather than rely on inconsistent definitions (cell volume, quadratic mean, cell diagonal, edge max/min), a simple gradient weighted length scale is superior. That is,

$$\Delta_{grid} = \left(\frac{u_{i,p}\mathcal{M}_{p,j}u_{i,q}\mathcal{M}_{q,j}}{u_{m,n}u_{m,n}} \right)^{1/2} \tag{B.16}$$

provides a measure of the least resolved orientation in the cell which, as stressed previously, is the relevant length scale to consider for RANS to LES transition. Alternatively, Q_{ij} may be employed as

$$\Delta_{grid} = \left(\frac{Q_{ij}Q_{ij}}{Q^I_{mn}Q^I_{mn}} \right)^{1/4} \tag{B.17}$$

where

$$Q^I_{ij} = u_{k,m}\delta_{mi}u_{k,n}\delta_{nj}. \tag{B.18}$$

Neither of these suggestions has been tested here, but widespread adoption in the DES community would do a great deal in establishing consistent practices.

B.5 Non-presumptive length scale based switching

As discussed in §3.4, the main reason for the grey-area problem is that switching from RANS to LES behavior based solely on a comparison between the grid and the model length scales implicitly assumes the presence of turbulence at the grid length scale. A simple modification to the standard eddy viscosity definition which accounts for the state of the resolved follows from the estimate of the unresolved turbulent kinetic energy in (5.10) as

$$\nu_t = C_\mu L_{est} (\overline{v'^2})^{\frac{1}{2}} \tag{B.19}$$

where

$$L_{est} = \frac{k_{est}^{\frac{3}{2}}}{\epsilon}. \tag{B.20}$$

Anisotropy and hybridization may be built directly into this definition by using Q_{ij} such that

$$\nu^t_{ij} = C_\mu \min(k_{tot}\delta_{ij}, C_F Q_{ij})^{\frac{3}{2}} \frac{(\overline{v'^2})^{\frac{1}{2}}}{\epsilon}, \tag{B.21}$$

where the minimum is understood to consider the eigenvalues of Q_{ij}. Though not tested here, this procedure might be a way to alleviate the grey-area problem without requiring the blending parameter. The difficulty would be finding an accurate k_{res} to form k_{tot} for unsteady flows. Alternatively, (B.20) may be used in a DES instead of the ambiguous scalar measure of the grid size.

B.6 On the relation between the resolution inhomogeneity term and upwinding

It has long been known that upwinding can be expressed as standard central differencing plus a numerical diffusivity due to upwinding [112]. For simplicity, let us examine the one-dimensional case with grid spacing h. In this case,

$$\nu_{uds} = \frac{uh}{2} w_{uds}, \tag{B.22}$$

where w_{uds} would equal one for full upwinding and zero for full central differencing. The presented grid inhomogeneity correction term (5.18) would take the simplified 1-D form

$$\nu_c = uh\frac{dh}{dx} \tag{B.23}$$

Thus, we see the artificial diffusivity proposed to correct for grid inhomogeneities is simply the standard upwinding diffusivity weighted by the gradient of the resolution, *i.e.* $\nu_c = 2\nu_{uds}\nabla h$. Put in another way, the correction term is upwinding applied only to the change in resolution, δh, *i.e.* $\nu_c = u\delta h$. This is, of course, no surprise as (5.18) is derived from applying the convective operator to varying filter widths [57], but is worth stating as it provides insight into the nature of the term.

B.7 Time averaging

Time averaging is performed by take a local running average of the velocity field over some time window, t_{ave}, as

$$U_i^n|_{ave} = \frac{1}{w_t}\big((w_t - 1)U_i^{n-1}|_{ave} + \overline{U}_i^n\big), \tag{B.24}$$

where the averaging weight is

$$w_t = \max\left(\frac{t_{ave}}{\delta t}, 1\right), \tag{B.25}$$

and δt is the computational timestep. If this averaging is set to the the local subgrid turbulent timescale and provided $T_m \ll T_{RANS}$, then $U_i|_{ave} \approx \langle U_i\rangle + u_i - u_i'$. If we were able to distinguish between the unsteady mean field and the fluctuating component, we would have a very good estimate of the resolved turbulent field, $u_i^{res} = \overline{U}_i - \langle U_i\rangle = u_i - u_i'$, and therefore, the resolved turbulent kinetic energy, k_{res}. As discussed in §8.2.4, this information would greatly simplify and enhance the new hybrid method presented in Chapter 5. It is, unfortunately, not possible to separate the unsteady flow from the total resolved flow using any sort of time averaging. For arguments sake, let us assume the resolved turbulence is $k_{res} \approx \frac{1}{2}(\overline{U}_i - \langle U_i \rangle)(\overline{U}_i - \langle U_i \rangle)$ and the local total turbulent timescale is $T_{tot} = \frac{k_m + k_{res}}{\epsilon}$ to use as t_{ave}. For any unsteady flow where the local unsteady timescale is not significantly larger than the local largest turbulent timescale, the approximate k_{res} will be dominated by the unsteady kinetic energy and thus be completely incorrect. Determination of an accurate k_{res} is perhaps the most pressing need for the new hybrid model.

B.8 A modified approach

As discussed throughout this work, the main limitation of the new hybrid method is the lack of knowledge of k_{res} stemming from not being able to divide $\overline{U_i}$ into the mean, $\langle U_i \rangle$, and the resolved turbulence, u_i^{res}. An alternative approach would be to directly solve for these two components. That is, the unsteady RANS equations would be solved for the ensemble mean $\langle U_i \rangle$ with the full modeled Reynolds stress, τ_{ij}^{RANS}, along with u_i^{res}. The equations for the u_i^{res} are found readily from subtracting the RANS equations (3.1) from the LES equations (3.16) with $u_i^{res} = \overline{U_i} - \langle U_i \rangle$ as

$$\partial_t u_i^{res} + \partial_j (\langle U_i \rangle u_j^{res} + \langle U_j \rangle u_i^{res} + u_i^{res} u_j^{res}) = -\frac{1}{\rho} \partial_i p^{res} + \nu \partial_j \partial_j u_i^{res} - S_i^{res} \tag{B.26}$$

where the resolved source term results from the imbalance between the subgrid and Reynolds stress tensors as

$$S_i^{res} = \partial_j (\tau_{ij}^{SGS} - \tau_{ij}^{RANS}). \tag{B.27}$$

The subgrid stress would then be found either using the algebraic SF-SGS model presented in §5.2 using velocity differences found from the total resolved field, $\langle U_i \rangle + u_i^{res}$, or a hybridized version of the k_{SGS} transport model [61]. Limitations on S_i^{res} would be imposed to ensure it vanished when $\partial_j \tau_{ij}^{SGS} > \partial_j \tau_{ij}^{RANS}$. Finally, the production in the full RANS k equation would include u_i^{res} when nonzero (*i.e.* when not full RANS) as

$$\mathcal{P}_k = -\partial_j \langle U_i \rangle (u_i^{res} u_j^{res} + \tau_{ij}^{SGS}), \tag{B.28}$$

with the Reynolds stress appearing in the mean equations modified similarly. Of course, the issue with this method is the computational overhead associated with the additional 3-4 transport equations and the additional Poisson equation for p^{res}. The expense could be lessened by solving the the two sets of equations on separate grids, that is, only using a coarsened version for the mean field. As an additional advantage, the heterogeneity correction term could be applied only to the u_i^{res} to obviate the limitations in $\mathcal{C}_r$ intended to prevent activation in RANS regions.

Bibliography

[1] G. Schewe, “On the force fluctuations acting on a circular cylinder in crossflow from subcritical up to transcritical Reynolds numbers,” *Journal of Fluid Mechanics*, vol. 133, 1983.

[2] G. Woo, T. Crittenden, and A. Glezer, “Transitory separation control over a stalled airfoil,” *AIAA 39th Fluid Dynamics Conference*, 2009.

[3] D. Brzozowski and A. Glezer, “Transient separation control using pulse-combustion actuation,” *AIAA 3rd Flow Control Conference*, 2006.

[4] C. Wieselberger, “Neuere feststellungen uber die gestze des fluüssigkeits und luftwiderstands,” *Zeitschrift für Physik*, vol. 22, pp. 321–328, 1921.

[5] N. K. Delany and N. E. Sorensen, “Low-speed drag of cylinder of various shape,” *NACA Technical Note 3038*, no. 19930083675, 1953.

[6] R. K. Finn, “Determination of the drag on a cylinder at low Reynolds numbers,” *Journal of Applied Physics*, vol. 24, p. 774, 1953.

[7] D. J. Tritton, “Experiments on the flow past a circular cylinder at low Reynolds numbers,” *Cavendish Laboratory, Cambridge*, pp. 547–567, 1959.

[8] A. Roshko, “Experiments on the flow past a circular cylinder at very high Reynolds number,” *Journal of Fluid Mechanics*, vol. 10, no. 3, pp. 345–356, 1961.

[9] R. Panton, *Incompressible Flow.* John Wiley & Sons, 2013.

[10] D. Brzozowski, G. Woo, J. Culp, and A. Glezer, "Transient separation control using pulse-combustion actuation," *AIAA Journal*, vol. 48, no. 11, pp. 2482–2490, 2010.

[11] B. N. Rajani, A. Kandasamy, and S. Majumdar, "Numerical simulation of laminar flow past a circular cylinder," *Applied Mathematical Modelling*, vol. 33, pp. 1228–1247, 2009.

[12] J. Slotnick, A. Khodadoust, J. Alonso, D. Darmofal, W. Gropp, E. Lurie, and D. Mavriplis, "CFD vision 2030 study: A path to revolutionary computational aerosciences," *NASA/CR?2014-218178*, 2014.

[13] G. Woo, T. Crittenden, and A. Glezer, "Transitory control of a pitching airfoil using pulse combustion actuation," *AIAA 4th Flow Control Conference*, 2008.

[14] G. Woo and A. Glezer, "Transitory control of separating flow over a dynamically-pitching airfoil," *AIAA 48th Aerospace Science Meeting*, 2010.

[15] C. Mockett, *A comprehensive study of detached-eddy simulation.* University of TU Berlin, 2009.

[16] J. Anderson, "Ludwig Prandtl's boundary layer," *Physics Today*, pp. 42–48, 2005.

[17] M. G. el Hak, *Flow control: passive, active, and reactive flow management.* Cambridge University Press, 2000.

[18] K. Kaepernick, L. Koop, and K. Ehrenfried, "Investigation of the unsteady flow field inside a leading edge slat cove," *AIAA 11th Aeroacousticd Conference*, 2005.

[19] J. Eaton and J. Johnston, "A review of research on subsonic turbulent flow reattachment," *AIAA Journal*, vol. 19, no. 9, 1981.

[20] A. Jacobi and R. Shah, "Heat transfer surface enhancement through the use of tlongitudinal vortices: A review of recent progress," *Experimental Thermal and Fluid Science*, vol. 11, pp. 295–309, 1995.

[21] J. C. Lin, "Review of research on low-profile vortex generators to control boundary-layer separation," *Progress in Aerospace Sciences*, vol. 28, pp. 389–420, 2002.

[22] T. R. Bewley, "Flow control: new challenges for a new renaissance," *Progress in Aerospace Sciences*, vol. 37, pp. 21–58, 2001.

[23] A. Glezer and M. Amitay, "Synthetic jets," *Annual Review of Fluid Mechanics*, vol. 34, pp. 503–529, 2002.

[24] A. Glezer, "Some aspects of aerodynamic flow control using synthetic-jet actuation," *Philosophical Transactions of the Royal Society A*, vol. 369, pp. 1476–1494, 2011.

[25] E. Mednikov and B. Novitski, "Experimental study of intense acoustic streaming," *Soviet Physics and Acoustics*, vol. 21, pp. 152–154, 1975.

[26] I. Lebedeva, "Experimental study of acoustic streaming in the vicinity of orifices," *Soviet Physics and Acoustics*, vol. 26, pp. 331–333, 1980.

[27] K. McManus and J. McGill, "Airfoil performance enhancement using pulsed jet separation control," *AIAA Journal*, 1997.

[28] D. Greenblatt and I. Wygnanski, "The control of flow separation by periodic excitation," *Progress in Aerospace Science*, vol. 36, no. 7, pp. 487–545, 2000.

[29] S. Collis, R. Joslin, A. Seifert, and V. Theofilis, "Issues in active flow control: theory, control, simulation, and experiment," *Progress in Aerospace Sciences*, vol. 40, pp. 237–289, 2004.

[30] M. DeSalvo and A. Glezer, "Aerodynamic performance modification at low angles of attack by trailing edge vortices," *AIAA 2nd Flow Control Conference*, 2004.

[31] M. DeSalvo and A. Glezer, “Control of airfoil aerodynamic performance using distributed trapped vorticity,” *AIAA 45th Aerospace Science Meeting and Exhibit*, 2007.

[32] A. Glezer, “Fluid mechanics research laboratory,” *Available: http://www.fmrl.gatech.edu/drupal/*, 2013.

[33] T. Crittenden and A. Glezer, “Combustion-driven jet actuators for flow control,” *AIAA 31st Fluid Dynamics Conference*, 2001.

[34] T. Crittenden, B. Warta, and A. Glezer, “Combustion-driven jet actuators for flow control,” *AIAA 3rd Flow Control Conference*, 2006.

[35] M. Dreka, “Xfoil: An analysis and design system for low Reynolds number airfoils,” *Conference on Low Reynolds Number Airfoil Aerodynamics*, 1989.

[36] P. Durbin, “Separated flow computations with the $k - \epsilon - \nu^2$ model,” *AIAA Journal*, vol. 33, no. 4, pp. 659–664, 1995.

[37] F. Lien, G. Kalitzin, and P. Durbin, “RANS modeling for compressible and transitional flows,” *Center for Turbulence Research Proceedings of the Summer Program 1998*, vol. 22, pp. 267–286, 1998.

[38] O. Metais and M. Lesieur, “Spectral large-eddy simulation of isotropic and stably stratified turbulence,” *Journal of Fluid Mechanics*, vol. 239, 1992.

[39] S. B. Pope, *Turbulent Flows.* Cambridge University Press, 2000.

[40] P. A. Durbin and B. A. P. Reif, *Statistical Theory and Modeling for Turbulent Flows.* John Wiley & Sons, 2010.

[41] P. Spalart, W. Jou, M. Strelets, and A. Allmaras, “Comments on the feasibility of LES for wings and on a hybrid RANS/LES approach,” *Proceeding of the 1st AFOSR Internation Conference on DNS/LES*, 1997.

[42] P. Spalart, “Detached-eddy simulation,” *Annual Review of Fluid Mechanics*, vol. 41, pp. 181–202, 2009.

[43] J. B. Perot and J. Gadebusch, “A self-adapting turbulence model for flow simulation at any mesh resolution,” *Physics of Fluids*, vol. 19, 2007.

[44] U. Piomelli and E. Balaras, “Wall-layer models for large-eddy simulations,” *Annual Review of Fluid Mechanics*, vol. 34, pp. 349–374, 2002.

[45] F. G. Schmitt, “About boussinesq?s turbulent viscosity hypothesis: historical remarks and a direct evaluation of its validity,” *C. R. Mecanique*, vol. 335, pp. 617–627, 2007.

[46] S. Pope, “A more general effective-viscosity hypothesis,” *Journal of Fluid Mechanics*, vol. 72, no. 2, pp. 331–340, 1975.

[47] A. Celic and E. Hirschel, “Comparison of eddy-viscosity models in flows with adverse pressure gradient,” *AIAA Journal*, vol. 44, no. 10, pp. 2156–2169, 2006.

[48] W. P. Jones and B. E. Launder, “The prediction of laminarization with a two-equation model of turbulence,” *International Journal of Heat and Mass Transfer*, vol. 15, pp. 301–314, 1972.

[49] P. A. Durbin, “On the k-3 stagnation point anomaly,” *International Journal of Heat and Mass Transfer*, vol. 17, pp. 89–90, 1996.

[50] V. C. Patel, W. Rodi, and G. Scheuerer, “Turbulence models for near-wall and low reynolds number flows: A review,” *AIAA Journal*, vol. 23, no. 9, pp. 1308–1319, 1985.

[51] T. H. Shih and N. N. Mansour, “Modeling of near-wall turbulence,” *NASA Technical Memorandum*, vol. 10322, 1990.

[52] P. A. Durbin, “Near-wall turbulence closure modeling without “damping functions”,” *Theoretical Computional Fluid Dynamics*, vol. 3, pp. 1–13, 1991.

[53] B. E. Launder, G. J. Reece, and W.Rodi, "Progress in the development of a reynolds-stress turbulence closure," *Journal of Fluid Mechanics*, vol. 68, no. 3, pp. 537–566, 1975.

[54] B. Launder and N. Sandham, *Closure strategies for turbulent and transitional flows.* Cambridge University Press, 2002.

[55] S. Parneix, P. Durbin, and M. Behnia, "Computation of 3-d turbulent boundary layers using the $\overline{v^2}f$ model," *Flow, Turbulence, and Combustion*, vol. 60, pp. 19–46, 1998.

[56] F. Lien and G. Kalitzin, "Computations of transonic flow with the $\nu^2 - f$ turbulence model," *Heat and Fluid Flow*, vol. 22, pp. 53–61, 2001.

[57] S. Ghosal and P. Moin, "The basic equations for the large eddy simulation of turbulent flows in complex geometry," *Journal of Computational Physics*, vol. 118, pp. 24–37, 1995.

[58] F. Hamba, "Analysis of filtered Navier-Stokes equation for hybrid RANS/LES simulation," *Physics of Fluids*, vol. 23, 2011.

[59] C. Meneveau and J. Katz, "Scale-invariance and turbulence models for large-eddy simulation," *Annual Review of Fluid Mechanics*, vol. 32, pp. 1–32, 2000.

[60] U. Piomelii, W. H. Cabot, P. Moin, and S. Lee, "Subgrid-scale backscatter in turbulent and transitional flows," *Physics of Fluids A: Fluid Dynamics*, vol. 3, no. 7, pp. 1989–1993, 1991.

[61] J. W. Deardorff, "The use of subgrid transport equations in a three-dimensional model of atmospheric turbulence," *ASME Journal of Fluids Engineering*, vol. 95, pp. 429–438, 1973.

[62] L. Gicquel, P. Givi, F. Jaberi, and S. Pope, "Velocity filtered density function for large eddy simulation of turbulent flows," *Physics of Fluids*, vol. 14, pp. 1196–1213, 2002.

[63] A. Misra and D. Pullin, "A vortex-based subgrid stress model for large-eddy simulation," *Physics of Fluids*, vol. 9, pp. 2443–2454, 1997.

[64] F. Grinstein, L. Margolin, and W. Rider, *Implicit large eddy simulation: computing turbulent fluid dynamics*. Cambridge University Press, 2007.

[65] D. K. Lilly, "The representation of small scale turbulence in numerical simulation experiments," *IBM Scientific Computing Symposium on environmental sciences*, pp. 195–210, 1967.

[66] M. Lesieur, *Turbulence in Fluids*. Springer, 2008.

[67] M. Germano, U. Piomelli, P. Moin, and W. H. Cabot, "A dynamic subgrid-scale eddy viscosity model," *Physics of Fluids A: Fluid Dynamics*, vol. 3, p. 1760, 1991.

[68] D. K. Lilly, "A proposed modification of the germano subgrid?scale closure method," *Physics of Fluids A: Fluid Dynamics*, vol. 4, p. 633, 1992.

[69] M. Lesieur and O. Metais, "New trends in large-eddy simulations of turbulence," *Annual Review of Fluid Mechanics*, vol. 28, pp. 245–82, 1996.

[70] G. K. Batchelor, *The theory of homogeneous turbulence*. Cambridge University Press, 1953.

[71] A. A. Wray and J. C. R. Hunt, "Algorithms for classification of turbulent structures," *Proceedings of the IUTAM Symposium Topological Fluid Mechanics*, pp. 95–104, 1989.

[72] P. Spalart, "Strategies for turbulence modeling and simulations," *International Journal of Heat and Fluid Flow*, vol. 21, no. 3, pp. 252–263, 2000.

[73] M. Leschziner and D. Drikakis, "Turbulence modeling and turbulent-flow computation in aeronautics," *Aeronautical Journal*, vol. 106, no. 1061, pp. 349–383, 2001.

[74] M. Shur, P. Spalart, K. Squires, M. Strelets, and A. Travin, "Three-dimensionality in unsteady Reynolds averaged Navier-Stokes simulations of two-dimensional geometries," *AIAA Journal*, vol. 43, pp. 1230–1242, 2005.

[75] J. Frohlich and D. vonTerzi, "Hybrid LES/RANS methods for the simulation of turbulent flows," *Progress in Aerospace Sciences*, vol. 44, pp. 349–377, 2008.

[76] P. Batten, U. C. Goldberg, , and S. R. Chakravarthy, "Subgrid turbulence modeling for unsteady flow with acoustic resonance," *AIAA*, vol. 0473, 2000.

[77] P. Batten, U. C. Goldberg, and S. R. Chakravarthy, "Interfacing statistical turbulence closures with large-eddy simulation," *AIAA*, vol. 42, no. 3, pp. 485–492, 2004.

[78] R. A. Baurle, C. J. Tam, J. R. Edwards, and H. A. Hassan, "Hybrid simulation approach for cavity flows: Blending, algorithm, and boundary treatment issues," *AIAA Journal*, vol. 41, no. 8, pp. 1463–1480, 2003.

[79] J. Riou, E. Garnier, S. Deck, and C. Basdevant, "An extension of DDES applied to the computation of a generic missle fine in transonic regime," *Proceedings of the 7th International Symposium on Engineering Turbulence Modeling in Measurements*, pp. 732–737, 2008.

[80] M. Gritskevich, A. Garbaruk, J. Schutze, and F. Menter, "Development of DDES and IDDES formulations for the $k-\omega$ shear stress transport model," *Flow Turbulence Combustion*, vol. 88, pp. 431–449, 2012.

[81] S. Jee and K. Shariff, "Detached-eddy simulation based on the $\nu^2 - f$ model," *Seventh International Conference on Computational Fluid Dynamics*, 2012.

[82] C. Speziale, "Computing non-equilibrium turbulent flows with time- dependent rans and vles," *15th international conference on numerical methods in fluid dynamics*, 1996.

[83] C. Speziale, "Turbulence modeling for time-dependent rans and vles: a review," *AIAA*, vol. 36, no. 2, pp. 173–184, 2004.

[84] W. Cabot and P. Moin, "Approximate wall boundary conditions in the large-eddy simulation of high reynolds number flow," *Flow, Turbulence and Combustion*, vol. 63, pp. 269–291, 1999.

[85] P. Quemere and P. Sagaut, "Zonal multi-domain RANS/LES simulations of turbulent flows," *International Journal for Numerical Methods in Fluids*, vol. 40, no. 7, pp. 903–925, 2002.

[86] S. Deck, “Zonal-detached-eddy simulation of the flow around a high-lift configuration,” *AIAA*, vol. 43, no. 11, pp. 2372–2384, 2005.

[87] P. Spalart, S. Deck, M. Shur, K. Squires, M. Strelets, and A. Travin, “A new version of detached-eddy simulation, resistant to ambiguous grid densities,” *Theoretical Computational Fluid Dynamics*, vol. 20, pp. 181–195, 2006.

[88] M. Shur, P. Spalart, M. Strelets, and A. Travin, “A hybrid RANS-LES approach with delayed-DES and wall-modelled LES capabilities,” *International Journal of Heat and Fluid Flow*, vol. 29, pp. 1638–1649, 2008.

[89] P. Spalart and A. Allmaras, “A one-equation turbulence model for aerodynamic flows,” *La Recherche Aerospatiale*, vol. 1, pp. 5–21, 1994.

[90] J. Riou, E. Garnier, S. Deck, and C. Basdevant, “Improvement of delayed-detached eddy simulation applied to separated flow over missle fine,” *AIAA Journal*, vol. 47, no. 2, pp. 345–360, 2009.

[91] M. Breuer, N. Jovicic, and K. Mazaev, “Comparison of DES, RANS, and LES for separated flow around a flat plate at high incidence,” *International Journal for Numerical Methods in Fluids*, vol. 41, pp. 357–388, 2003.

[92] P. Spalart, “Young-person’s guide to detached-eddy simulation grids,” *NASA/CR-2001-211032*, 2001.

[93] J. B. Perot and S. M. DeBruynKops, “Modeling turbulent dissipation at low and moderate reynolds numbers,” *Journal of Turbulence*, vol. 7, no. 69, 2006.

[94] M. Leschziner and S. Lardeau, “Simulation of slot and round synthetic jets in the context of boundary-layer separation control,” *Philosophical Transactions of the Royal Society A*, vol. 369, pp. 1495–1512, 2011.

[95] S. Jee, *Flow Control Simulation with Synthetic and Pulsed Jet Actuator.* The University of Texas at Austin, 2010.

[96] T. Hőll, A. K. vel Job, P. Giacopinelli, and F. Thiele, "Numerical study of active flow control on a high-lift configuration," *Journal of Aircraft*, vol. 49, no. 5, 2012.

[97] D. Wilcox, "Formulation of the $k - \omega$ turbulence model revisited," *AIAA 45th Aerospace Sciences Meeting and Exhibit*, 2007.

[98] D. You and P. Moin, "A dynamic global-coefficient subgrid-scale eddy-viscosity model for large-eddy simulation in complex geometries," *Center for Turbulence Research Annual Research Briefs*, 2006.

[99] J. Gilaranz, L. Traub, and O. Rediniotis, "A new class of synthetic jet actuators, part ii application to flow separation control," *Journal of Fluids Engineering*, vol. 127, p. 377, 2005.

[100] A. Vreman, "An eddy-viscosity subgrid-scale model for turbulent shear flow," *Physics of Fluids*, vol. 16, no. 10, pp. 3670–3681, 2004.

[101] N. Park, S. Lee, J. Lee, and H. Choi, "A dynamic subgrid-scale eddy-viscosity model with a global model coefficient," *Physics of Fluids*, vol. 18, 2006.

[102] A. Scotti, C. Meneveau, and D. K. Lilly, "Generalized smagorinsky model for anisotropic grids," *Physics of Fluids A*, vol. 5, p. 2306, 1993.

[103] R. A. Clark, J. H. Ferziger, and W. C. Reynolds, "Evaluation of subgrid-scale models using an accurately simulated turbulent flow," *Journal of Fluid Mechanics*, vol. 91, pp. 1–16, 1979.

[104] U. Frisch, *Turbulence: The Legacy of A. N. Kolmogorov.* Cambridge University Press, 1995.

[105] F. Ham and G. Iaccarino, "Energy conservation in collocated discretization schemes on unstructured meshes," *Center for Turbulence Research Annual Research Briefs*, 2004.

[106] M. Lee and R. D. Moser, “Direct numerical simulation of turbulent channel flow up to Re=5200,” *Journal of Fluid Mechanics*, vol. 774, pp. 395–415, 7 2015.

[107] W. D. Bachalo and D. A. Johnson, “Transonic, turbulent boundary-layer separation generated on an axisymmetric flow mode,” *AIAA Journal*, vol. 24, no. 3, pp. 437–443, 1986.

[108] S. G. Goebel and J. C. Dutton, “Experimental study of compressible turbulent mixing layers,” *AIAA Journal*, vol. 29, no. 4, pp. 538–546, 1991.

[109] F. Menter and Y. Egorov, “The scale-adaptive simulation method for unsteady turbulent flow predictions. part 1: Theory and model description,” *Flow Turbulence Combustion*, vol. 83, pp. 113–138, 2010.

[110] R. Mittal and P. Moin, “Suitability of upwind-biased finite difference schemes for large-eddy simulation of turbulent flows,” *AIAA Journal*, vol. 35, no. 8, pp. 1415–1417, 1997.

[111] A. Travin, M. Shur, and M. Strelets, “Physical and numerical upgrades in the detached-eddy simulation of complex turbulent flows,” *Advances in LES of Complex Flows*, pp. 239–254, 2000.

[112] A. N. Brooks and T. J. R. Hughes, “Streamline upwind/Petrov-Galerkin formulations for convection dominated flows with particular emphasis on the incompressible navier-stokes equations,” *Computer Methods in Applied Mechanics and Engineering*, vol. 32, pp. 199–259, 1982.

Vita

Sigfried William Haering was born in Guayaquil, Ecuador on 27 August 1981. He received a Bachelor of Science degree in Engineering from the University of New Mexico and was commissioned an Officer in the United States Air Force in 2003. He entered active duty in February 2004, and was stationed at Wright-Patterson Air Force Base, Dayton, Ohio, where he worked at the Air Force Research Laboratory in the field of behavior and life predictions of gas turbine engine components. He separated from the USAF in 2007 to attend graduate school at the University of Texas at Austin in Mechanical Engineering where he received a Masters of Science degree in 2010 for his experimental and numerical work in predicting nanoparticle mediated photodistruption with application towards skin cancer treatment.

Permanent address: 2205 Canterbury St
Austin, Texas 78702

This dissertation was typeset with LaTeX[†] by the author.

[†] LaTeX is a document preparation system developed by Leslie Lamport as a special version of Donald Knuth's TeX Program.